emission rate either with fixed or time variable airborne fraction. As long as this emission is not zero, the atmospheric concentration further increases, independent of its actual level; and also at constant emissions the system never reaches steady state.

However, when such unusual correlation between emission and absorption rates would really exist, this cannot only be restricted to anthropogenic emissions and switched off for native emissions. Due to the equivalence principle it should be valid for both. *Also for times before 1750 the absorption process cannot have been completely different to that over the Industrial Era or was suddenly changing with the first anthropogenic emissions.*

The dramatic consequences when applying the Bern Model to the total emissions are illustrated in Figure 11. This would result in an exploding atmospheric CO_2 concentration (Green Line) up to levels found 500 Mio. yr ago, and it would never allow steady state conditions as supposed before 1750. In average such an increase over the last 270 yr is equivalent to an $AF = 35\%$.

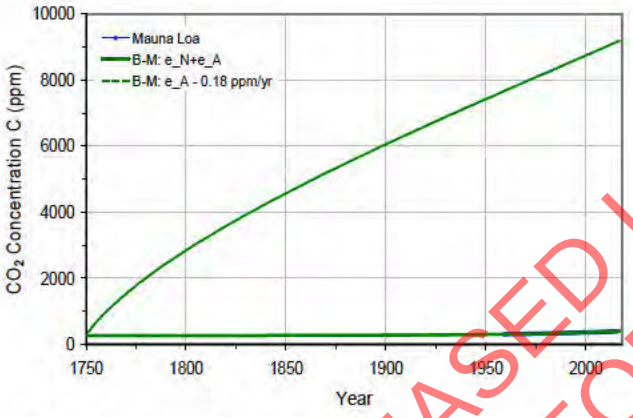

Figure 11. *Simulation of the CO_2 concentration based on the Bern Model assuming the total emissions (Green). Also shown is a calculation for only anthropogenic emissions (Green Crosses). Compared against the observed record of CO_2 from Mauna Loa (Blue Diamonds).*

An uptake process only scaling with the emission rate and not the concentration looks completely unrealistic (see also subsection 3.4). It must be dismissed, even when the simulation for the anthropogenic emissions alone (Green Crosses) pretends good agreement with the Mauna Loa observations (Blue Diamonds).

A balance which only adds up net emissions, and denies an increasing absorption rate with inclining atmospheric concentration, is in contradiction to real observations and hurts fundamental physical laws. CO_2 is not a noble gas, which indifferently accumulates in an open compartment after an emission, but it is dissolved in oceans and converted via photosynthesis to organic molecules. This uptake obeys a first order absorption process and scales with the actual concentration or the difference to an external reservoir[1]. It prevails as long as its concentration C or the difference remains nonzero, i.e., indefinitely.

Different to subsections 3.1 and 3.2 approach 3.3 already emanates from a first order absorption process, but it is also restricted only to anthropogenic concentration changes. Basically an 'ansatz' in (22), third case, and considering changes relative to some reference concentration is correct, when this also includes natural variations over the considered time period. But the fundamental flaw in 3.3 is to introduce a new, independent absorption constant, the adjustment time, for the uptake of the additional emissions instead of using the same absorption process, which already controls more than 95% of the carbon cycle, and this - due to physical causalities - at pre- industrial times in the same manner as over the Industrial Era.

5.3. Environment as a Net Sink

From the observations of the atmospheric concentration and estimates of anthropogenic emissions it is widely inferred that not natural but anthropogenic origin is responsible for the increasing atmospheric CO_2. Writing the global atmospheric carbon budget in the form (see e.g., Cawley [22])

$$\frac{dC}{dt} - e_A(t) = e_N - a_T < 0\,, \tag{25}$$

it is obvious that the net environmental flux, e_N - a_T can quite well be assessed without needing to know the absolute magnitudes of e_N or a_T, quantities which on their parts are highly uncertain. Since the concentration changes dC/dt are smaller than the anthropogenic emission rate, the left side of (25) is negative and thus, the environmental uptake a_T must be larger than the natural emissions e_N. From this correct statement that the environment has acted as a net sink throughout the Industrial Era, however, often wrong conclusions are derived that nature cannot be the reason for any observed CO_2 increase.

For a moment let us assume e_N may be the emission rate at which the system was in balance, and e_A may represent an additional rate of human or native emissions or of both. In reality and in all discussed models with airborne fraction or with first order uptake the concentration growth rate develops slower than these additional emissions and thus, a_T gets larger than e_N. So, with both sides of (25) getting negative this only means that with additional emissions, native or humans, nature also acts as a further increasing sink (compared to a previous equilibrium). As long as any arbitrary fraction of human emission is involved, the environment is always a net sink. This is true per definition, since up to now no artificial uptake exists. But this does not say anything about any additional native emissions over the Industrial Era, since emission and uptake are largely independent processes and the absorption does not impede nature from increasing its own emissions.

A similar strange logic is used by Richardson [29], who

[1] Diffusion processes which act proportional to the concentration difference between two reservoirs, can be assumed to consist of an outflux proportional to the atmospheric concentration C_a and an influx proportional to the concentration of the reservoir C_r.

considers mean values of the net atmospheric accumulation $\langle dC/dt\rangle = 1.7$ *ppm/yr* and of the human emissions $\langle dC_A/dt\rangle = e_A(t) = 3$ *ppm/yr* in a balance

$$\langle dC/dt\rangle - \langle dC_A/dt\rangle = \langle dC_N/dt\rangle < 0\,, \tag{26}$$

in which with $\langle dC_A/dt\rangle = e_A(t)$ a priori any anthropogenic absorptions are embezzled. From this relation it is also inferred that the average natural contribution $\langle dC_N/dt\rangle$ has been to remove CO_2 from the atmosphere, this with the same wrong conclusion as Cawley that the long term trend of rising CO_2 could not be explained by natural causes. This argument is disproved with Figures 8 and 10. The fact that the environment has acted as a net sink throughout the Industrial Era is a consequence of a dynamic absorption rate, which is only controlled by the total CO_2 concentration $C = C_N + C_A$. So, also with additional native emissions and/or temperature changes in the absorptivity the total uptake always tries - with some time delay - to compensate for the total emissions which, of course, also include the anthropogenic fraction. In other words: *Since nature cannot distinguish between native and human emissions, nature is always a net sink as long as human emissions are not zero.* Thus, except for shorter temporary events like volcanic activities the environment will generally act as a net sink even in the presence of increasing natural emissions.

To equate $\langle dC_A/dt\rangle$ in (26) exclusively with human emissions violates conservation of mass. Only when replacing $\langle dC_A/dt\rangle$ by $\langle e_A(t) - C_A/\tau_R\rangle$, eq.(26) satisfies the Conservation Law, and when additionally replacing $\langle dC_N/dt\rangle$ by $\langle e_N(t) - C_N/\tau_R\rangle$ eq.(26) converts to (23).

Again we emphasize that a separate treatment of the native and human cycle with their respective concentrations C_A and C_N is possible if and only if no contributions are missing and the two balances are linked together in one rate equation with only one unitary residence time.

5.4. Too Simple Model

Often climate scientists argue that changes of CO_2 in the atmosphere cannot be understood without considering changes in extraneous systems (see e.g., AR5 [1], Chap.6; Köhler et al. [8]), and they characterize the Conservation Law as a flawed 1-box description because, a single balance equation would not account for details in other reservoirs. In particular, they refer to carbonate chemistry in the ocean, where CO_2 is mostly converted to bicarbonate ions. As only about 1% remains in the form of dissolved CO_2, they argue that only this small fraction could be exchanged with the atmosphere. Due to this so-called Revelle effect, carbonate chemistry would sharply limit oceanic uptake of anthropogenic CO_2.

In regard to understanding changes of CO_2 in the atmosphere, changes in extraneous systems are only qualifiedly of interest. The governing law of CO_2 in the atmosphere (4) and in more elaborate form (23) is self contained. With the inclusion of the surface fluxes $e_T(t)$ and $a_T(t) = C/\tau_R(t)$, which account for influences of the adjacent reservoirs on atmospheric CO_2, details of other extraneous reservoirs of carbon are entirely irrelevant. This feature of the governing physics is not only powerful, but fortunate.

Concerning carbonate chemistry, it is noteworthy that, in the Earth's distant past, CO_2 is thought to have been almost 2000% as great as its present concentration (e.g., Royer et. al. [30]). Most of that was absorbed by the oceans, in which carbon today vastly exceeds that in the atmosphere. According to the IPCC, even in modern times the oceans account for 40% of overall absorption of CO_2 (AR5 [1], Fig.6.1). In relation to other sinks, their absorption of CO_2 is clearly not limited (see Appendix A). Of that 40%, over the Industrial Era anthropogenic CO_2 represents less than 1%. Contrasting with that minor perturbation in absorption is oceanic emission of CO_2. Through upwelling of carbon-enriched water, the oceans significantly enhance natural emission of CO_2 (Zhang [31]).

Different to our approach, which takes into account human and also naturally varying emissions and absorptions, the models in Section 3 emanate from such a simple and apparently flawed description that over thousands of years CO_2 was circulating like an inert gas in a closed system, and only with the industrial revolution this closed cycle came out of control due to the small injections by human emission.

5.5. Different Time Constants

The different time scales introduced with the models in Section 3 represent different absorption processes for the uptake of atmospheric CO_2 molecules by the extraneous reservoirs. From physical principles it is impossible that an absorption process would differentiate between naturally and anthropogenically emitted molecules. The temporal absorption or sequestration - except for smallest corrections due to isotopic effects - is for all molecules identical.

The absorption also cannot decline unexpectedly by more than one order of magnitude with the begin of the Industrial Era or because of an additional emission rate of a few %. Observations show that no noticeable saturation over recent years could be found (Appendix A).

Oceans and continents consist of an endless number of sources and sinks for CO_2 which act parallel, emitting CO_2 into the atmosphere and also absorbing it again. In the same way as the different emission rates add up to a total emission, the absorption rates with individual absorptivities α_i - and each of them scaling proportional to the actual CO_2 concentration - add up to a total uptake as a collective effect

$$\begin{aligned} a_T &= \alpha_1 C + \alpha_2 C + \ldots + \alpha_N C \\ &= (\alpha_1 + \alpha_2 + \ldots + \alpha_N)\cdot C = \alpha_R \cdot C \end{aligned}\,. \tag{27}$$

Collective absorption thus leads to exponential decay of perturbation CO_2 at a *single* rate

$$\alpha_R = 1/\tau_R = \alpha_1 + \alpha_2 + \ldots + \alpha_N\,. \tag{28}$$

This decay rate is faster than the rate of any individual sink

and it prevails as long as its concentration C or its difference to external reservoirs remains nonzero (see: Harde [6]; Salby [11]).

The above behavior is a consequence of the Conservation Law and in contrast to the Bern Model, where decay proceeds at *multiple* rates. A treatment of CO_2 with a multiple exponential decay obeys the following:

$$\begin{aligned} C &= C_{10}e^{-\alpha_1 t} + C_{20}e^{-\alpha_2 t} + ... + C_{N0}e^{-\alpha_N t} \\ &= C_1 + C_2 + ... + C_N \end{aligned} \quad . \tag{29}$$

Then differentiation gives:

$$\begin{aligned} \frac{dC}{dt} &= -\alpha_1 C_{10}e^{-\alpha_1 t} - \alpha_2 C_{20}e^{-\alpha_2 t} ... - \alpha_N C_{N0}e^{-\alpha_N t} \\ &= -\alpha_1 C_1 - \alpha_2 C_2 ... - \alpha_N C_N \\ &\neq -(\alpha_1 + \alpha_2 + ... + \alpha_N) \cdot C \end{aligned} \tag{30}$$

At multiple decay rates the corresponding sinks operate, not collectively, but independently. After a couple of their decay times, the fastest sinks become dormant. Overall decay then continues only via the slowest sinks, which remove CO_2 gradually. It is for this reason that such a treatment leaves atmospheric CO_2 perturbed for longer than a thousand years (Figure 5). In contrast, the behavior required by the Conservation Law decays as fast or faster than that of the fastest sink (see (28)).

The observed decay of ^{14}C shows that the corresponding absorption is determined by a single decay time and operates on a time scale of only about one decade (see Figure 5). This scale is the same for the natural carbon cycle as for the anthropogenic cycle. Therefore, it is unrealistic to differentiate between a residence time and different adjustment times.

In this context it should be noticed that due to re-emissions of $^{14}CO_2$ from extraneous reservoirs the real residence time of $^{14}CO_2$ in the atmosphere as well as that of the other isotopologues of CO_2 can only be shorter, even shorter than a decade (for details see subsection 5.7.3 and Appendix B).

5.6. Temperature Dependence

According to (9) or (10) we see that with increasing atmospheric concentration over the Industrial Era from 280 to 400 ppm either the residence time must be increased with temperature from 3 to about 4 yr, or τ_R is considered to be constant and the total emissions were rising from 93 to about 130 ppm/yr, synchronously increasing the concentration. Both these limiting cases are in agreement with a temperature anomaly of about 1.2 °C over this period (see GISS [9]), when we assume the maximum temperature coefficients $\beta_\tau = 0.74$ *yr/°C* or $\beta_e = 24$ *ppm/yr/°C*. However, generally both temperature induced natural emissions as well as temperature dependent absorptions together will dictate the inclining concentration in the atmosphere.

In any way, as we see from Figure 8, is the CO_2 concentration dominantly empowered by the temperature increase; with only one unique decay process not human activities but almost only natural impacts have to be identified as the main drivers for the observed CO_2 increase in the atmosphere and also for the continuous climate changes over the past and present times.

The various mechanisms, along with their dependence on temperature and other environmental properties, could not have remained constant during the pre-industrial era. This inconsistency invalidates the fundamental assumption, that natural emission and absorption during the pre-industrial period did remain constant. Even less this is valid over the Industrial Era, a period which is characterized by the IPCC as the fastest rise in temperature over the Holocene or even the last interglacial.

So, the CO_2 partial pressure in sea water approximately changes with temperature as $(pCO_2)_{sw}(T) = (pCO_2)_w(T_0)$* *exp*$[0.0433*(T-T_0)]$ (see: Takahashi et al. [32]) and thus, an increase of *1°C* causes a pressure change of about *18 µatm*, which amplifies the influx and attenuates the outflux. From observations over the North Atlantic Ocean (see, Benson et al. [33]) it can be estimated that a pressure difference ΔpCO_2 between the atmosphere and ocean of *1 µatm* contributes to a flux change of $\delta f_{in} \approx 0.075$ *mol/m²/yr = 3.3 g/m²/yr*. Therefore, with an Earth s surface of *320 Mio. km²* covered by oceans and a pressure change of $\Delta pCO_2 = 18$ *µatm,* under conventional conditions the native influx from oceans to the atmosphere already increases by $\Delta f_{in} \approx 19$ *Pg/yr* or *2.4 ppm/yr* for an ave age temperature incline of *1°C*. An even stronger variation can be expected for the land vegetation with an increased decomposition and reduced uptake of CO_2 at rising temperature (Lee [34]; Salby [11]).

Together this causes an incline of the atmospheric CO_2 level which is larger than all apparent human activities, but its contribution is completely neglected in the official accounting schemes.

Also melting permafrost and emissions of volcanoes on land and under water as well as any emissions at earthquakes are not considered. In addition, actual estimates of dark respiration suggest that under global warming conditions whole-plant respiration could be around 30% higher than existing estimates (Huntingford et al. [35]). This longer list of different native events and effects is completely embezzled in the favored IPCC models.

Equally inconsistent is the presumption that additional uptake of anthropogenic CO_2, which represents less than 1% of the total over the Industrial Era, has, somehow, exceeded the storage capacity of oceans and other surface and sub-surface reservoirs, capacity which is orders of magnitude greater. *A reduced absorption is rather the consequence of global warming than of saturation*. Due to Henry's law and its temperature dependence not only the partial pressure in sea water increases, but also the solubility of CO_2 in water declines exponentially with temperature and, thus, reduces the CO_2 uptake. Often is this effect incorrectly misinterpreted as saturation caused by a limited buffer capacity and dependent on the concentration level. But here we consider an uptake changing with temperature, as this is known for chemical reactions, where the balance is controlled by temperature. How strongly the biological pump (see Appendix A) and

photosynthesis on land is also controlled by temperature, is only incompletely known, but obviously they are also varying slightly exponentially with temperature (Lee [34]).

Figure 12 displays a scatter plot supporting the close correlation of the atmospheric CO_2 concentration with the land-ocean temperature anomaly (GISS [9]). The latter is controlled by more than 60% by the solar influence and less than 40% by CO_2 as greenhouse gas feedback (Harde [36, 37]).

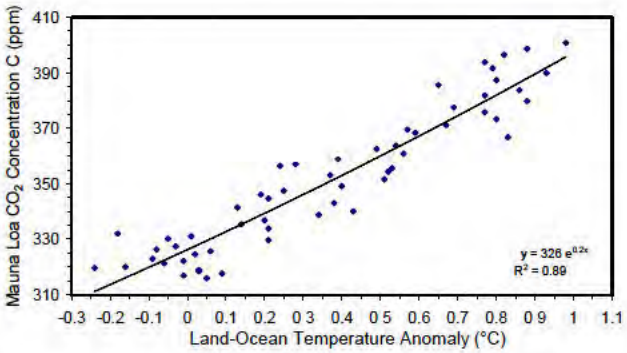

Figure 12. *Scatter plot of Mauna Loa CO_2 concentration (Blue Diamonds) and trend curve (Black Graph) versus land-ocean temperature anomaly.*

5.7. IPCC Arguments for a Human-Made CO_2 Increase

The preceding discussion has made clear that a consistent description of the carbon-cycle, which is in full agreement with all observations and physical relations, can only emanate from unitary treatment of all CO_2 molecules - native and human-caused ones. This means: the anthropogenic carbon cycle cannot be separated from the natural cycle; it exists only one single residence time of CO_2 molecules in the atmosphere; and the uptake of all these molecules obeys a first order principle.

But we still have to scrutinize how far this description is really in contradiction to the key arguments (lines of evidence) as adduced by the IPCC for a human caused CO_2 incline, or how far these arguments also hold for our alternative approach.

In AR5 [1], Subchap.6.3.2.3 we read:

"*With a very high confidence, the increase in CO_2 emissions from fossil fuel burning and those arising from land use change are the dominant cause of the observed increase in atmospheric CO_2 concentration.*"

IPCC then lists five arguments to support this conclusion (references in the following IPCC-citations are not listed as additional references in this article).

5.7.1. Decrease in Atmospheric O_2

The observed decrease in atmospheric O_2 content over past two decades and the lower O_2 content in the northern compared to the SH are consistent with the burning of fossil fuels (see Figure 6.3 and Section 6.1.3.2; Keeling et al., 1996; Manning and Keeling, 2006)."

This is barely a supporting argument for a dominantly man-made CO_2 increase, since this 'line of evidence' is in the same way valid for our approach, which evidently includes the same amount of anthropogenic emissions. Burning of fossil fuels removes oxygen from the atmosphere in a tightly defined stoichiometric ratio dependent on the fuel carbon content. This content is the same in our balance as in the IPCC models, therefore, the respective O_2 decay rate and on the other hand the CO_2 growth rate due to combustion is also the same, independent of any additional emissions of natural origin. The fundamental difference to the IPCC's assumption is that the anthropogenic emissions do not cumulate in the atmosphere for longer times or for ever. They have the same residence time as native CO_2, in average 4 yr or shorter, and therefore they only contribute 15% or even less to the observed increase since 1750.

In this context it should also be clear that CO_2 and O_2 behave just anti-cyclic in the photosynthesis and respiration cycle. Also the biochemical reactions in the atmosphere are completely different. CO_2 is a non-reacting gas in the atmosphere, while O_2 preferentially oxidizes other materials and is tied in chemical compounds. All these reactions are directly controlled by the temperature. Compared to the atmospheric oxygen content of about 21% a decrease of 80 ppm over 20 yr is relatively small, it is not more than 0.4‰. As long as this O_2 cycle is not better known, an observed decline in atmospheric oxygen gives only little evidence for a dominantly human caused CO_2 increase. At best it can confirm the CDIAC-data, which are the same in our approach as in the IPCC models.

5.7.2. Lower $^{13}C/^{12}C$ Isotope Ratio in Fossil Fuels

CO_2 from fossil fuels and from the land biosphere has a lower $^{13}C/^{12}C$ stable isotope ratio than the CO_2 in the atmosphere. This induces a decreasing temporal trend in the atmospheric $^{13}C/^{12}C$ ratio of atmospheric CO_2 concentration as well as, on annual average, slightly lower $^{13}C/^{12}C$ values in the NH (Figure 6.3). These signals are measured in the atmosphere."

Also this is no supporting argument for a dominantly man-made CO_2 increase, as with our approach we are also expecting such declining $^{13}CO_2$ concentration. The $^{13}C/^{12}C$ ratio in the atmosphere or its normalized ‰-difference $(\delta^{13}C)_{atm}$ is measured at Mauna Loa and at the South Pole atmospheric station (see AR5 [1], Figure 6.3). At Mauna Loa, e.g., it shows an average decrease of 0.7‰ from -7.6‰ in 1980 to -8.3‰ in 2010. Over these 30 years was the anthropogenic emission rate increasing by *1.8 ppm/yr* from *2.5 ppm/yr* in 1980 to *4.3 ppm/yr* in 2010 (CDIAC [4]). With respect to the total emission rate this corresponds to an increase of 1.8 %.

Owing to the equivalence principle fossil fuel emissions cannot cumulate in the atmosphere but will be absorbed with the same probability like naturally emitted CO_2 molecules. Thus, in first order the $^{13}C/^{12}C$ ratio in the atmosphere can only be diluted proportional to the leaner ^{13}C concentration and proportional to the fraction of the man-made flux to the total flux. Smaller corrections will result from the fractionation for lighter molecules and a slightly higher emission probability for molecules, which were just taken up (re-emission, see next

item).

Since the fossil fuel emissions have a leaner difference $(\delta^{13}C)_{fuel\text{-}atm}$ = -18 ‰ compared to the atmosphere, or $(\delta^{13}C)_{fuel\text{-}VPDB}$ = -25 ‰ with respect to the international VPDB carbonate standard (Coplen [38]), the rising human emissions over the 30 yr interval can only have contributed to a decline of $\Delta = (\delta^{13}C)_{fuel\text{-}atm} \times 1.8\% = -18‰ \times 1.8\% = -0.32$ ‰ or a $(\delta^{13}C)_{atm}$ = -7.92‰ in 2010. Thus, the difference to -8.3‰, which is more than 50%, in any case must be explained by other effects.

One possible explanation for a faster decline of $(\delta^{13}C)_{atm}$ to -8.3‰ can be - even with oceans as source and an $^{13}C/^{12}C$ ratio in sea water greater than in air (particularly in the surface layer) - that the lighter $^{12}CO_2$ molecules are easier emitted at the ocean's surface than $^{13}CO_2$, this with the result of a leaner ^{13}C concentration in air and higher concentration in the upper water layer (see also: Siegenthaler & Münnich [39]). From water we also know that its isotopologues are evaporated with slightly different rates.

Such behavior is in agreement with the observation that with higher temperatures the total CO_2 concentration in the atmosphere increases, but the relative $^{13}CO_2$ concentration decreases. This can be observed, e.g., at El Niño events (see: M. L. Salby [40], Figure 1.14; Etheridge et al. [41]; Friedli et al. [42]).

We also remind at the Mauna Loa curve, which shows for the total emissions a seasonal variation with an increasing CO_2 concentration from about October till May and a decline from June to September. The increase is driven by respiration and decomposition mainly on the Northern Hemisphere (NH) as well as the temperature on the Southern Hemisphere (SH) and also local temperature effects. The $(\delta^{13}C)_{atm}$ value is just anti-cyclic to the total CO_2 concentration (AR5 [1], Figure 6.3) with a minimum at maximum CO_2 concentration and with seasonal variations of 0.3 - 0.4‰, the same order of magnitude as the fossil fuel effect.

An increase of ^{13}C in the upper strata of oceans also results from an increased efficiency of photosynthesis for lighter CO_2. Plankton accumulates this form and sinks to lower layers, where it decomposes and after longer times is emitted in higher concentrations with stronger upwelling waters particularly in the Eastern Tropic Pacific. It is also known that the ^{13}C concentrations are by far not equally distributed over the Earth's surface. Thus, it can be expected that with volcanic and tectonic activities different ratios will be released.

So, without any doubts fossil fuel emissions will slightly dilute the $^{13}CO_2$ concentration in air. But presupposing regular conditions for the uptake process (equivalence principle) they contribute less than 50% to the observed decrease. The difference has to be explained by additional biogeochemical processes. Particularly the seasonal cycles and events like El Niños are clear indications for a stronger temperature controlled modulation of the $(\delta^{13}C)_{atm}$ value. Therefore is an observed decline of the $^{13}C/^{12}C$ ratio over recent years by far not a confirmation of an anthropogenic global warming (AGW) theory.

Also the widely spread but wrong declaration that "*about half of the emissions remained in the atmosphere since 1750*" and "*the removal of all the human-emitted CO_2 from the atmosphere by natural processes will take a few hundred thousand years (high confidence)*" (see AR5 [1], Chap. 6-Summary and Box 6.1) can be simply refuted by the isotope measurements at Mauna Loa. If the *113 ppm* CO_2 increase since 1750 (28.8% of the present concentration of *393 ppm* - average between 2007 and 2016) would only result from human impacts and would have cumulated in the atmosphere, the actual $(\delta^{13}C)_{atm}$ value should have dropped by $\Delta = (\delta^{13}C)_{fuel\text{-}atm} \times 28.8\% = -18‰ \times 28.8\% = -5.2‰$ to $(\delta^{13}C)_{atm} \approx$ -7‰ -5.2‰ = -12.2‰, which by far is not observed. $(\delta^{13}C)_{atm}$ in 1750 was assumed to have been -7‰.

5.7.3. Fossil Fuels are Devoid of Radiocarbon

"Because fossil fuel CO_2 is devoid of radiocarbon (^{14}C), reconstructions of the $^{14}C/C$ isotopic ratio of atmospheric CO_2 from tree rings show a declining trend, as expected from the addition of fossil CO_2 (Stuiver and Quary, 1981; Levin et al., 2010). Yet nuclear weapon tests in the 1950s and 1960s have been offsetting that declining trend signal by adding ^{14}C to the atmosphere. Since this nuclear weapon induced ^{14}C pulse in the atmosphere has been fading, the $^{14}C/C$ isotopic ratio of atmospheric CO_2 is observed to resume its declining trend (Naegler and Levin, 2009; Graven et al., 2012)."

For ^{14}C we can adduce almost the same comments as listed for ^{13}C. Fossil CO_2 devoid of ^{14}C will reduce the $^{14}C/C$ ratio of the atmosphere, this is valid for our approach in the same manner as for the IPCC schemes. But, as no specific accumulation of anthropogenic molecules is possible (equivalence principle), this decline can only be expected proportional to the fraction of fossil fuel emission to total emission. Before 1960 this was not more than 1% and actually it is about 4.3%.

^{14}C is continuously formed in the upper atmosphere from ^{14}N through bombardment with cosmic neutrons, and then rapidly oxidizes to $^{14}CO_2$. In this form it is found in the atmosphere and enters plants and animals through photosynthesis and the food chain. The isotopic $^{14}C/C$ ratio in air is about $1.2 \cdot 10^{-12}$, and can be derived either from the radioactivity of ^{14}C, which with an average half-lifetime of 5730 yr decays back to ^{14}N by simultaneously emitting a beta particle, or by directly measuring the amount of ^{14}C in a sample by means of an accelerator mass spectrometer.

Fossil fuels older than several half-lives of radiocarbon are, thus, devoid of the ^{14}C isotope. This influence on radiocarbon measurements is known since the investigations of H. Suess [43] who observed a larger ^{14}C decrease (about 3.5%) for trees from industrial areas and a smaller decline for trees from unaffected areas. This so-called Suess or Industrial effect is important for reliable age assignments by the radiocarbon method and is necessary for respective corrections. But for global climate considerations it gives no new information, it only confirms the calculations based on the human to total emission rate (see above), and it clearly shows that an assumed accumulation of anthropogenic CO_2 in the

atmosphere contradicts observations.

More important for climate investigations is that after the stop of the nuclear bomb tests 1963 ^{14}C could be used as a sensitive tracer in the biosphere and atmosphere to study temporal carbon mixing and exchange processes in the carbon cycle. As the bomb tests produced a huge amount of thermal neutrons and almost doubled the ^{14}C activity in the atmosphere, with the end of these tests the temporal decline of the excess radiocarbon activity in the atmosphere can well be studied. This decline is almost completely independent of the radioactive lifetime, but practically only determined by the uptake through extraneous reservoirs.

Such decline has already been displayed in Figure 5 as fractionation-corrected ‰-deviations $\Delta^{14}CO_2$ from the Oxalic Acid activity corrected for decay, this for a combination of measurements at Vermunt and Schauinsland (Magenta Dots and Green Triangles; data from Levin et al. [17]). The decay is well represented by a single exponential with a decay constant of about 15 yr (Dashed Blue). For similar observations see also Hua et al. [18] and Turnbull et al. [19]. Thus, the decay satisfies the relation

$$\frac{dC'_{14}}{dt} = -\frac{1}{\tau_{14}} \cdot C'_{14}, \tag{31}$$

where C'_{14} represents the excess concentration of radiocarbon above a background concentration in the atmosphere. It corresponds to absorption that is proportional to instantaneous concentration with an apparent absorption time τ_{14} slightly more than a decade.

Because CO_2 is conserved in the atmosphere it can change only through an imbalance of the surface fluxes e_T and a_T. This holds for all isotopologues of CO_2 in the same way. For this reason, its adjustment to equilibrium must proceed through those influences. They are the same influences that determine the removal time of CO_2 in the atmosphere. If CO_2 is perturbed impulsively (e.g., through a transient spike in emission), its subsequent decay must track the removal of perturbation CO_2, C', which in turn is proportional to its instantaneous concentration. Determined by the resulting imbalance between e_T and a_T, that decay is governed by the perturbation form of the balance equation:

$$\frac{dC'}{dt} = -\frac{1}{\tau_R} \cdot C', \tag{32}$$

which is the same form as the observed decay of ^{14}C following elimination of the perturbing nuclear source. But there is still one important difference between these equations.

Eq.(32) is the perturbation form of (23) with a decay time τ_R, the residence time, because $1/\tau_R$ describes the rate at which CO_2 is removed from the atmosphere, this as the result of the balance between all absorption and emission processes.

In contrast to this describes (31) a decay process, which implicitly also considers some back-pumping of radiocarbon to the atmosphere (see Appendix B, (37)). So, from all ^{14}C that is removed from the atmosphere with the time constant τ_R - in the same way as all isotopes -, only some smaller fraction is completely sequestered beneath the Earth's surface by a single absorption process. A substantial fraction is therefore returned to the atmosphere through re-emission (e.g., through decomposition of vegetation which has absorbed that ^{14}C), and in average it takes several absorption cycles to completely remove that ^{14}C from the atmosphere. This simply modifies the effective absorption for radiocarbon, but with a resulting decay which remains exponential (see Figure 5). Unlike any dilution effect by fossil fuel emission, which is minor (see Appendix B), this re-emission slows decay over what it would be in the presence of pure absorption alone. Therefore is the apparent absorption time - as derived from the ^{14}C decay curve - longer than the actual absorption time.

In this context we emphasize that apart from some minor influence due to fractionation all CO_2 isotopologues are involved in the same multiple re-emission cycles. But in (23) or (32) this is already considered in the total balance via the emission rates, for which it makes no difference, if the same or meanwhile exchanged molecules are recycled to the atmosphere. In contrast to this are $^{14}CO_2$ isotopologues identified through their radioactivity, and in the worst case without any dilution or exchange processes in an external reservoir τ_{14} would approach the radioactive lifetime. On the other hand, at strong diffusion, dilution or sequestration of ^{14}C in such reservoirs τ_{14} would converge to τ_R. Consequently it follows from the observed ^{14}C decay shown in Figure 5 that this provides an upper bound on the actual absorption time τ_R, which can be only shorter. Both are tremendously shorter than the adjustment time requested by the IPCC.

The exponential decay of ^{14}C with only one single decay time proves models with multiple relaxation times to be wrong. At the same time it gives strong evidence for a first order absorption process as considered in Section 4.[2]

5.7.4. Higher Fossil Fuel Emissions in the Northern Hemisphere

"Most of the fossil fuel CO_2 emissions take place in the industrialised countries north of the equator. Consistent with this, on annual average, atmospheric CO_2 measurement stations in the NH record increasingly higher CO_2 concentrations than stations in the SH, as witnessed by the observations from Mauna Loa, Hawaii, and the South Pole (see Figure 6.3). The annually averaged concentration difference between the two stations has increased in proportion of the estimated increasing difference in fossil fuel combustion emissions between the hemispheres (Figure 6.13; Keeling et al., 1989; Tans et al., 1989; Fan et al., 1999)".

The strongest terrestrial emissions result from tropical forests, not industrial areas. The strongest oceanic emissions can be seen from the map of Takahashi et al. [32]. They are

[2] A calculation similar to Figure 8 but with a residence time of 15 yr as an upper bound would require to reduce the natural emissions at pre-industrial times from *93 ppm/yr* to *19 ppm/yr*. Then the anthropogenic contribution would supply *59 ppm*, which is 15% of the total atmospheric concentration or 52% of the increase since 1850.

between 10°N and 10°S in the Eastern Tropic Pacific. Nevertheless, there is no doubt that industrial emissions endow their fingerprints in the atmosphere and biosphere (Suess effect). The influence and size of these emissions has already been discussed above, and their different impact on the two hemispheres can be estimated from Figure 6.3c of AR5 [1] indicating a slightly faster decline of $(\delta^{13}C)_{atm}$ for the NH in agreement with predominantly located industrial emissions in this hemisphere. Even more distinctly this is illustrated by Figure 6.13 of AR5 [1] for the difference in the emission rates between the northern and SH with 8 PgC/yr, which can be observed as a concentration difference between the hemispheres of 3.8 ppm. But this is absolutely in no dissent to our result in Section 4 that from globally *4.7 ppm/yr* FFE and LUC (average emission over 10 yr) 17 ppm or 4.3 % contribute to the actual CO_2 concentration of *393 ppm* (average). This impact is of the same size as seasonal variations observed at Mauna Loa before flattening and averaging the measurements.

5.7.5. Human Caused Emissions Grew Exponentially

> *"The rate of CO_2 emissions from fossil fuel burning and land use change was almost exponential, and the rate of CO_2 increase in the atmosphere was also almost exponential and about half that of the emissions, consistent with a large body of evidence about changes of carbon inventory in each reservoir of the carbon cycle presented in this chapter".*

The size and influence of FFE and LUC on the atmospheric CO_2 concentration has extensively been discussed in the preceding sections. Only when violating fundamental physical principles like the equivalence principle or denying basic causalities like a first order absorption process with only a single absorption time, the CO_2 increase can be reproduced with anthropogenic emissions alone.

In contrast to that we could demonstrate that conform with the rising temperature over the Industrial Era and in conformity with all physical legalities the overwhelming fraction of the observed CO_2 increase has to be explained by native impacts. Such simulations reproduce almost every detail of the observed atmospheric CO_2 increase (see Figures 8 and 10). And from observations of natural emissions it can be seen that they are increasing slightly exponential with temperature (Takahashi et al. [32]; Lee [34]).

Thus, no one of the preceding lines of evidence can really support the above statement that "*fossil fuel burning and land use change are the dominant cause of the observed increase in atmospheric CO_2 concentration*." In fact, they apply in the same way for our concept, and thus they are useless to disfavour our approach. The isotopic studies rather confirm our ansatz of a first order absorption process with a single absorption time, which is significantly shorter than one decade, and they refute the idea of cumulating anthropogenic emissions in the atmosphere.

6. Conclusion

The increase of CO_2 over recent years can well be explained by a single balance equation, the Conservation Law (23), which considers the total atmospheric CO_2 cycle, consisting of temperature and thus time dependent natural emissions, the human activities and a temperature dependent uptake process, which scales proportional with the actual concentration. This uptake is characterized by a single time scale, the residence time of about 3 yr, which over the Industrial Era slightly increases with temperature. Only this concept is in complete conformity with all observations and natural causalities. It confirms previous investigations (Salby [7, 10]; Harde [6]) and shows the key deficits of some widespread but largely ad hoc carbon cycle models used to describe atmospheric CO_2, failures which are responsible for the fatal conclusion that the increase in atmospheric CO_2 over the past 270 years is principally anthropogenic.

For a conservative assessment we find from Figure 8 that the anthropogenic contribution to the observed CO_2 increase over the Industrial Era is significantly less than the natural influence. At equilibrium this contribution is given by the fraction of human to native impacts. As an average over the period 2007-2016 the anthropogenic emissions (FFE&LUC together) dominated not more than 4.3% to the total concentration of 393 ppm, and their fraction to the atmospheric increase since 1750 of 113 ppm is not more than 17 ppm or 15%. With other evaluations of absorption, the contribution from anthropogenic emission is even smaller. Thus, not really anthropogenic emissions but mainly natural processes, in particular the temperature, have to be considered as the dominating impacts for the observed CO_2 increase over the last 270 yr and also over paleoclimate periods.

Acknowledgements

The author thanks Prof. Murry Salby, formerly Macquarie University Sydney, for many stimulating discussions when preparing the paper, and Jordi López Fernández, Institute of Environmental Assessment and Water Studies Barcelona, for his support when searching for temperature data.

This research did not receive any specific grant from funding agencies in the public, commercial, or not-for-profit sectors.

Appendix

Appendix A

The absorption efficiency of extraneous reservoirs has been claimed to have decreased, based on changes in the arbitrarily-defined airborne fraction (e.g., Le Quéré et al. [12]; Canadell et al. [44]). Such claims are dubious because they rely on the presumption that changes of CO_2 are exclusively of anthropogenic origin. Nor are the claims supported by recent atmospheric CO_2 data. Gloor et al. [45] found that decadal changes of AF followed from changes in the growth of anthropogenic emissions - not from changes in absorption efficiency, which were comparatively small. Further, uncertainties in emission and absorption exceeded any

changes in AF. Ballantyne et al. [46] arrived at a similar conclusion. They used global atmospheric CO_2 measurements and CO_2 emission inventories to evaluate changes in global CO_2 sources and sinks during the past 50 years. Their mass balance analysis indicates that net CO_2 uptake significantly increased, by about 0.18 Pg/yr (0.05 GtC/yr) and, between 1960 and 2010, that global uptake actually doubled, from 8.8 to 18.4 Pg/yr. It follows that, without quantitative knowledge of changes in natural emission, interpretations based on AF are little more than speculative.

The uptake and outgassing of atmospheric CO_2 by oceans is simulated with complex marine models. How much CO_2 enters or leaves the ocean surface is calculated from the difference between atmospheric and surface concentrations of CO_2, modified by the Revelle factor. However, most of these models involve assumptions which are not in agreement with observed behavior (see, e.g., Steele [47]). They assume that the surface layer absorbs CO_2 through equilibrium with atmospheric concentration. On this premise, they calculate how much Dissolved Inorganic Carbon (DIC) will be added to the ocean based on increased atmospheric CO_2 since pre-industrial times. In reality, the surface layer is not at equilibrium with the atmosphere. A difference in concentration results from conversion of CO_2 into organic carbon by photosynthesis. Organic carbon produced then sinks into the deep ocean, where it is sequestered. This downward transport to the deep ocean is known as the biological pump. In the Northeastern Atlantic basin, e.g., Benson et al. [33] report on seasonal pressure differences between the ocean and atmosphere of $\Delta pCO_2 = -70\ \mu atm$ and an air-sea CO_2 flux *of* $220\ g/m^2/yr$. Only in those regions where strong upwelling of DIC from the deep ocean exceeds sequestration of carbon via photosynthesis can CO_2 be outgassed to the atmosphere. The latter is found primarily in the tropical oceans (Takahashi et al. [32]; Zhang et al. [31]). Several models es imate that, without the biological pump, atmospheric CO_2 would be 200 to 300 ppm higher than current levels (see also Evans [48]).

With increasing primary production, carbon export to depth also grows. Arrigo et al. [49] reported that since 1998, annual primary production in he Arctic has increased by 30%. Steinberg et al. [50] observed a 61% increase in meso-plankton between 1994 and 2006 in the Sargasso Sea. The North Atlantic coccolithophores h ve increased by 37% between 1990 and 2012 (Krumhardt et al. [51]). And Chavez et al. [52] found a dramatic increase in primary production in the Peru Current since the end of the Little Ice Age (LIA). Together, the increase in primary production and downward transport of organic carbon is sufficient to account for anthropogenic CO_2 that was absorbed from the atmosphere (Steele [47]).

Further, seasonal changes in surface CO_2 illustrate that absorption of CO_2 by the oceans and accumulation of DIC near the surface are determined, not by the Revelle factor, but by the biological pump. Evans et al. [48] found from buoy data off the coast of Newport, Oregon that each spring photosynthesis lowers ocean surface CO_2 to 200 ppm - far below current atmospheric concentrations and much lower than what would be expected from equilibrium with a pre-industrial atmosphere. Anthropogenic CO_2 in surface water is then quickly removed. It is also well known that higher concentrations of CO_2 magnify photosynthesis. At increased atmospheric CO_2, the plankton community consumed 39% more DIC (Riebesell et al. [53]). During summer and autumn, surface CO_2 can rapidly increase to 1000 ppm - more than twice the concentration of CO_2 in the atmosphere. Surface water then significantly enhances natural emission to the atmosphere. Conversely, during winter, surface CO_2 remains at about 340 ppm. Despite reduced photosynthesis, CO_2 in surface water then remains below equilibrium with the atmosphere, reflecting efficient removal through downward transport by the biological pump. It is noteworthy that these strong seasonal variations of CO_2 in surface water are manifest in the record of atmospheric CO_2 (see Figures 9 and 10).

Under steady state conditions, diffusion of CO_2 into the ocean is believed to require about 1 year to equilibrate with an atmospheric perturbation. But, when increased sunlight enhances photosynthesis, such equilibration is no longer achieved. Perturbation CO_2 is then simply transported to depth, where it is sequestered from surface waters (McDonnell et al. [54]). Under such conditions uptake of CO_2 is not restricted by the Revelle factor but by the biological pump.

The foregoing processes are controlled essentially by sunlight and temperature. There is no reason to believe that net primary production, the biological pump, and sequestration of CO_2 below surface waters would be the same today as 270 years ago, when temperature and atmospheric CO_2 were likely lower.

In simulating transport of carbon in the ocean, complex models assume behavior that is found in tracers like chlorofluorocarbons (CFCs). Because those species accumulate near the ocean surface, models assume DIC does as well. But unlike CFCs, which are inert, CO_2 entering sunlit waters is quickly converted to organic matter by photosynthesis (Steele [47]). Although dissolved CFCs and dissolved carbon are passively transported in the same manner, particulate organic carbon (alive or dead) behaves very differently. It rapidly sinks, removing carbon from surface water through mechanisms which do not operate on CFCs.

The removal of carbon from surface water depends on the sinking velocity and also on how rapidly organic matter is decomposed. After descending below the pycnocline (depths of 500-1000 meters), carbon is effectively sequestered - because water at those depths does not return to the surface for centuries (Weber et al. [55]). For the atmosphere, this long-term sequestration translates into removal that is effectively permanent. Before such carbon can return to the atmosphere, fossil fuel reserves will have long since been exhausted.

The combination of sinking velocities and sequestration depth suggests that a significant fraction of primary production is sequestered in a matter of days to weeks (Steele [47]). Therefore, increasing primary production leads to a proportionate increase and rapid export of carbon to depth. If marine productivity has increased since pre-industrial times, it will

have also sequestered the respective anthropogenic carbon into the deeper ocean. Observations from ocean basins suggest that, since the Little Ice Age, marine productivity and carbon export have indeed increased as the oceans warmed (Chavez et al. [52]; Abrantes et al. [56]).

Appendix B

The bomb radiocarbon signal in the atmosphere is a sensitive tracer to study the fluxes in the carbon cycle, in particular to determine an upper bound for the residence time of CO_2 in the atmosphere and its uptake through extraneous reservoirs. Carbon 14 obeys the balance equation

$$\frac{dC_{14}}{dt} = e_{14} - \frac{C_{14}}{\tau_{14}} \tag{33}$$

with e_{14} as the emission rate, which follows from background emission of ^{14}C as well as anthropogenic emission. The decay after the stop of the bomb tests in 1963 then satisfies the relation (see Subsection 5.7.3, (31))

$$\frac{dC'_{14}}{dt} = -\frac{1}{\tau_{14}} \cdot C'_{14}, \tag{34}$$

where C'_{14} represents the excess concentration of radiocarbon above background concentration in the atmosphere, and τ_{14} is the apparent absorption time of about 15 yr. Regularly not the absolute number of ^{14}C but its ratio to ^{13}C or ^{12}C is measured, either as radioactivity or by accelerator mass spectrometry.

As the total CO_2 concentration is not constant over the observed decay period and this directly affects the relative ^{14}C decay as well as the background level, the measured ^{14}C activity has to be corrected for these variations to obtain the true C'_{14} concentration. Such corrections are important for age dating of materials and also for atmospheric ^{14}C measurements. Without compensating for the varying total concentration, e.g., the ^{14}C-decay and the background would be modified by several ten %.

Mostly the corrected data are specified as fractionation-corrected ‰-deviations from the Oxalic Acid standard activity corrected for decay (see Stuiver&Polach [57]):

$$\Delta^{14}C = \left[\frac{A_{SN}}{A_{ABS}} - 1\right] \cdot 1000 \tag{35}$$

with A_{SN} as sampling activity normalized for isotope fractionation to ^{13}C, and A_{ABS} as the absolute international standard activity (Oxalic Acid standard). A_{SN} relates to the measured sample activity A_S as

$$A_{SN} = A_S\left[1 - \frac{2(25+\delta^{13}C}{1000}\right], \tag{36}$$

where $\delta^{13}C$ is specified in ‰ with respect to the ^{13}C VPDB standard.

This normalization procedure also accounts for fossil fuel emissions, which are devoid of ^{14}C and also have a leaner ^{13}C abundance. So, human emissions dilute the $^{14}C/^{12}C$ and $^{13}C/^{12}C$ ratio in the atmosphere. Such corrections are important for correct age assignments, but how much does this industrial effect and the observed dilution also affect the atmospheric ^{14}C decay?

To answer this question we compare the original $\Delta^{14}CO_2$ data of Vermunt and Schauinsland shown in Figure 5, with a hypothetical $\Delta^{14}CO_2$-distribution, which is found for a fixed $\delta^{13}C$-value over the full observation period, thus, assuming no further dilution. This requires first to recalculate the sampling activity A_S from (35) and (36) with the known $\delta^{13}C$-record, e.g., from Mauna Loa (AR5 [1], Chap6, Figure 6.3c, missing data from 1964-1976 can be extrapolated from this record), and then to simulate the decay curve with new A_S activities, which are derived for a constant $\delta^{13}C(1964) = -7.4‰$.

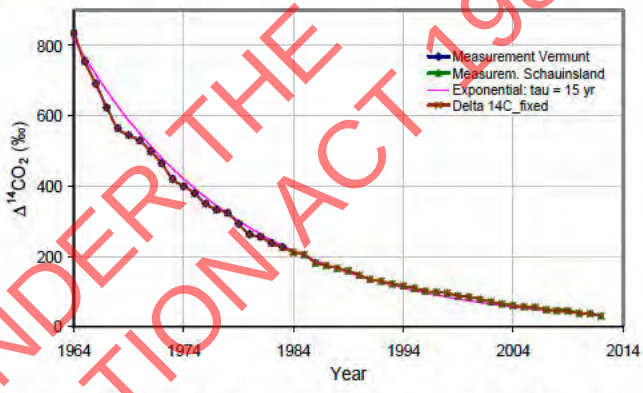

Figure 13. $\Delta^{14}CO_2$-evolution for Vermunt and Schauinsland (Magenta Dots and Green Triangles), compared with a recalculated decay neglecting dilution effects (Brown Crosses). Additionally shown is an exponential fit with an e-folding time of 15 yr (Magenta).

Figure 13 displays the normalized $\Delta^{14}CO_2$-values of Vermunt and Schauinsland (Blue Diamonds and Green Triangles; data from Levin et al. [17]) as reproduction of Figure 5 on a magnified scale.

It directly compares this with the hypothetical $\Delta^{14}CO_2$ decay curve (Brown Crosses). Deviations over the observed time period of 48 yr are smaller than 2‰ and the respective graphs completely coincide on this scale. They can well be approximated by a single exponential with a decay time of 15 yr (Magenta Line). Thus, any dilution effect of fossil fuel and natural emissions can well be neglected for the ^{14}C-decay.

Far more influential is re-emission of ^{14}C that was absorbed from the atmosphere. On the time scale of observed absorption, not all ^{14}C is directly sequestered beneath the Earth's surface, but needs several cycles before being removed from the atmosphere. This can be described by a perturbation balance, which different to (33) now considers the regular absorption (characterized by the residence time τ_R) and takes account of an emission rate e'_{14}, now for re-emitted ^{14}C from the upper Earth layer (e.g., through decomposition of vegetation which has absorbed that ^{14}C), before it is sequestered or distributed:

$$\frac{dC'_{14}}{dt} = e'_{14} - \frac{C'_{14}}{\tau_R} \approx \left(\frac{C'_{14}}{\tau_R} - \frac{C'_{E,14}}{\tau_{14}}\right) - \frac{C'_{14}}{\tau_R} \approx -\frac{C'_{14}}{\tau_{14}}. \tag{37}$$

Primed quantities are now referenced against unperturbed values before introduction of the nuclear source. From a balance for the Earth layer it follows that in good approximation e'_{14} opposes the atmospheric absorption rate C'_{14}/τ_R minus the sequestration rate $C'_{E,14}/\tau_{14}$, for which it is assumed that the concentration in the upper layer $C'_{E,14}$ is almost the same as the concentration C'_{14} in the atmosphere. Thus, re-emission simply modifies the effective absorption, which for ^{14}C is controlled by the apparent absorption time τ_{14} and not the residence time τ_R in agreement with (34).

Unlike the dilution effect, which is minor, this slows decay over what it would be in the presence of absorption alone. The apparent absorption time is therefore *longer* than the actual absorption time, which must even be shorter than a decade. Integration of (37) or (34) exactly reproduces a pure exponential decay in Figure 13 with an e-folding time $\tau_{14} = 15$ *yr*.

References

[1] AR5, In: Stocker, T. F., Qin, D., Plattner, G.-K., Tignor, M., Allen, S. K., Boschung, J., Nauels, A., Xia, Y., Bex, V., Midgley, P. M. (Eds.), "Climate Change 2013: The Physical Science Basis. Contribution of Working Group I to the Fifth Assessment Report of the Intergovernmental Panel on Climate Change", Cambridge University Press, Cambridge, United Kingdom and New York, NY, USA, 2013.

[2] C. Le Quéré et al., "Global Carbon Budget 2017", Earth Syst. Sci. Data Discuss., https://doi.org/10.5194/essd-2017-123 Open Access Earth System Science Data Discussions, Manuscript under review for journal Earth Syst. Sci. Data, 2017

[3] CICERO, Center for International Climate Research, Oslo, R Andrew: http://folk.uio no/roberan/GCP2017.shtml 2017.

[4] CDIAC, 2017: Carbon Dioxide Information Analysis Center http://cdiac.ornl.gov/trends/emis/glo_2014.html.

[5] C. D. Keeling, S. C. Piper, R. B. Bacastow, M. W hlen, T. P. Whorf, M. Heimann, H. A. Meijer, "Atmospheric CO_2 and $^{13}CO_2$ exchange with the terrestrial biosphere and oceans from 1978 to 2000: Observation and carbon cycle implications", In: Ehleringer, J. R., Cerling, T. E., Dearing, M. D. (Eds.), A History of Atmospheric CO2 and Its Effects on Plants, Animals, and Ecosystems. Springer Science+Business Media, New York, NY, USA, and Heidelberg, Germany, pp. 83–113 (actualized by Scripps-Institutes, USA), 2005.

[6] H. Harde, "Scrutinizing the carbon cycle and CO_2 residence time in the atmosphere", Global and Planetary Change 152, pp. 19–26, 2017. http://dx.doi.org/10.1016/j.gloplacha.2017.02.009.

[7] M. L. Salby, "Atmospheric Carbon", Video Presentation, July 18, 2016. University College London. https://youtu.be/3q-M_uYkpT0.

[8] P. Köhler, J. Hauck, C. Völker, D. A. Wolf-Gladrow, M. Butzin, J. B. Halpern, K. Rice, R. E. Zeebe, Comment on "*Scrutinizing the carbon cycle and CO2 residence time in the atmosphere*" by H. Harde, Global and Planetary Change 164, pp. 67-71, 2017. https://doi.org/10.1016/j.gloplacha.2017.09.015

[9] GISS, 2017: Goddard Institute for Space Studies: https://data.giss nasa.gov/gistemp/.

[10] M. L. Salby, "Relationship Between Greenhouse Gases and Global Temperature", Video Presentation, April 18, 2013. Helmut-Schmidt-University Hamburg https://www.youtube.com/watch?v=2ROw_cDKwc0.

[11] M. L. Salby, "What is Really Behind the Increase of Atmospheric CO_2"? Helmut-Schmidt-University Hamburg, 10. October 2018, https://youtu.be/rohF6K2avtY

[12] C. Le Quéré, M. R. Raupach, J. G. Canadell, G. Marland et al., "Trends in the sources and sinks of carbon dioxide", Nature Geosci., 2, pp. 831–836, 2009. doi:10.1038/ngeo689.

[13] P. Tans, NOAA/ESRL and R. Keeling, Scripps Institution of Oceanography (scrippsco2.ucsd.edu/), 2017. https://www.esrl noaa.gov/gmd/ccgg/trends/data html.

[14] F. Joos, M. Bruno, R. Fink, U. Siegenthaler, T. F. Stocker, C. Le Quéré, J. L. Sarmiento, "An efficient and accurate representation of complex oceanic and biospheric models of anthropogenic carbon uptake", Tellus B 48, pp. 397–417, 1996. doi:10.1034/j.1600-0889.1996.t01-2-00006.x.

[15] J. Hansen, M. Sato, P. Kharecha, G. Russell, D. W. Lea, M. Siddall, "Climate change and trace gases", Phil. Trans. R. Soc. A 365, pp. 1925–1954, 2007. doi:10.1098/rsta.2007.2052.

[16] J. Hansen, M. Sato, G. Russell, K. Pushker, "Climate sensitivity, sea level, nd atmospheric CO_2", Philos. Trans. R. Soc. A, 371, 20120294, 2013. doi:10.1098/rsta.2012.0294. https://www.nasa.gov/

[17] I. Levin, B. Kromer, and S. Hammer, "Atmospheric $\Delta^{14}CO_2$ trend in Western European background air from 2000 to 2012", Tellus B 65, pp. 1-7, 2013.

[18] Q. Hua, M. Barbetti, A. Z. Rakowski, "Atmospheric radiocarbon for the period 1950–2010". RADIOCARBON 55, pp. 2059–2072, (2013). Supplementary Material Table S2c, https://doi.org/10.2458/azu_js_rc.v55i2.16177

[19] J. C. Turnbull, S. E. Mikaloff Fletcher, I. Ansell, G. W. Brailsford, R. C. Moss, M. W. Norris, K. Steinkamp, "Sixty years of radiocarbon dioxide measurements at Wellington, New Zealand: 1954–2014", Atmos. Chem. Phys. 17, pp. 14771–14784, 2017. https://doi.org/10.5194/acp-17-14771-2017.

[20] U. Siegenthaler, J. L. Sarmiento, "Atmospheric carbon dioxide and the ocean", Nature 365, pp. 119-125, 1993.

[21] P. Dietze, IPCC's Most Essential Model Errors, 2001. http://www.john-daly.com/forcing/moderr.htm; (Carbon Model Calculations, http://www.john-daly.com/dietze/cmodcalc htm).

[22] G. C. Cawley, "On the Atmospheric Residence Time of Anthropogenically Sourced Carbon Dioxide", Energy Fuels 25, pp. 5503–5513, 2011. dx.doi.org/10.1021/ef200914u

[23] H.-J. Lüdecke, C. O. Weiss, "Simple Model for the Anthropogenically Forced CO_2 Cycle Tested on Measured Quantities", JGEESI, 8(4), pp. 1-12, 2016. DOI: 10.9734/JGEESI/2016/30532.

[24] R. E. Essenhigh, "Potential dependence of global warming on the residence time (RT) in the atmosphere of anthropogenically sourced carbon dioxide", Energy Fuel 23, pp. 2773–2784, 2009. http://pubs.acs.org/doi/abs/10.1021/ef800581r.

[25] E. Berry, "Human CO_2 has little effect on atmospheric CO_2", 2019. https://edberry.com/blog/climate-physics/agw-hypothesis/contradictions-to-ipccs-climate-change-theory/

[26] NOAA, 2017: https://www.esrl noaa.gov/psd/data/gridded/data ncep reanalysis html http://iridl.ldeo.columbia.edu/SOURCES/.NOAA/.NCDC/.GHCN/.v2/?bbox=bb%3A-161.488%3A16.360%3A-150.062%3A23.051%3Abb

[27] NOAA, 2018: http://iridl.ldeo.columbia.edu/SOURCES/.NOAA/.NCDC/.ERSST/.version2/.SST/index html http://iridl.ldeo.columbia.edu/SOURCES/.NOAA/.NCDC/.ERSST/.version2/.SST/X/%28164W%29VALUES/T/%28Jan%201938%29%28Dec%202009%29RANGEEDGES/Y/%2819N%29VALUES/datafiles.html

[28] O. Humlum, K. Stordahl, J. E. Solheim, "The phase relation between atmospheric carbon dioxide and global temperature", Global and Planetary Change 100, pp. 51-69, 2013.

[29] M. Richardson, Comment on "The phase relation between atmospheric carbon dioxide and global temperature" by Humlum, Stordahl and Solheim, Global and Planetary Change 107, pp. 226-228, 2013.

[30] D. L. Royer, R. A. Berner, I. P. Montañez, N. J. Tabor, D. J. Beerling, "CO_2 as a primary driver of Phanerozoic climate", GSA Today 14, no. 3, 2004. doi: 10.1130/1052-5173(2004)014<4:CAAPDO>2.0.CO;2.

[31] Y. G. Zhang, M. Pagani, J. Henderiks, H. Ren, "A long history of equatorial deep-water upwelling in the Pacific Ocean", Earth and Planetary Science Letters 467, pp. 1–9, 2017. http://dx.doi.org/10.1016/j.epsl.2017.03.016.

[32] T. Takahashi, S. C. Sutherland, R. Wanninkhof, C. Sweeney, R A. Feely et al., "Climatological mean and decadal change in surface ocean pCO_2 and net sea-air CO_2 flux over the global oceans", Deep-Sea Res. II, 56, pp. 554–577, 2009. doi:10.1016/j.dsr2.2008.12.009.

[33] N. U. Benson, O. O. Osibanjo, F. E. Asuquo, W. U. Anake "Observed trends of pCO_2 and air-sea CO_2 fluxes in the North Atlantic Ocean, Intern. J. Marine Science 4, pp. 1-7, 2014.

[34] J.-S. Lee, "Monitoring soil respiration using an automatic operating chamber in a Gwangneung temperate deciduous forest", J. Ecology & Field Biology 34(4), pp. 411-423, 2011.

[35] C. Huntingford, O. K. Atkin, A. Martinez de la Torre, L. M. Mercado, M. A. Heskel, A. B. Harper, K. J. Bloomfield, O. S. O'Sullivan, P. B. Reich, K. R. Wythers, E. E. Butler, M. Chen, K. L. Griffin, P. Meir, M. G. Tjoelker, M. H. Turnbull, S. Sitch, A. Wiltshire, Y. Malhi, "Implications of improved representations of plant respiration in a changing climate", NATURE COMMUNICATIONS 8, 1602, 2017. DOI: 10.1038/s41467-017-01774-z.

[36] H. Harde, "Radiation Transfer Calculations and Assessment of Global Warming by CO_2", International Journal of Atmospheric Sciences, Volume 2017, Article ID 9251034, pp. 1-30, 2017. https://doi.org/10.1155/2017/9251034.

[37] H. Harde, "Was tragen CO_2 und die Sonne zur globalen Erwärmung bei"? 12. Internationale EIKE Klima- und Energiekonferenz und 13th International Conference on Climate Change (ICCC-13), München, 23. u. 24. November, 2018, https://youtu.be/ldrG4mn_KCs.

[38] T. B. Coplen, "Reporting of stable hydrogen, carbon and oxygen isotopic abundances", Pure and Applied Chemistry 66, pp. 273-276, 1994.

[39] U. Siegenthaler, K. O. Münnich, "$^{13}C/^{12}C$ fractionation during CO_2 transfer from air to sea", *In:* Bolin, B. (Ed.): *Carbon cycle modelling (SCOPE 16),* John Wiley & Sons, pp. 249-257, 1981.

[40] M. L. Salby, "Physics of the Atmosphere and Climate", Cambridge University Press, Cambridge 2012. (ISBN: 978-0-521- 76718-7).

[41] D. M. Etheridge, L. P. Steele, R. L. Langenfelds, R. J. Francey, J.-M. Barnola, V. I. Morgan, "Natural and anthropogenic changes in atmospheric CO2 over the last 1000 years from air in Antarctic ice and firn", J. Geophys. Res. 101, pp. 4115-4128, 1996.

[42] Friedli H., H. Lötscher, H. Oeschger, U. Siegenthaler, B. Stauffer, 1986. Ice core record of the 13C/12C ratio of atmospheric CO2 in the past two centuries, Nature 324, pp. 237-238.

[43] H. Suess, "Radiocarbon Concentration in Modern Wood", Science 122, Issue 3166, pp. 415-417, 1955. DOI: 10.1126/science.122.3166.415-a

[44] J. G. Canadell, Le Quéré, C., Raupach, M. R., Field, C. B., Buitenhuis, E. T., Ciais, P., Conway, T. J., Gillett, N. P., Houghton, R. A., and Marland G., "Contributions to accelerating atmospheric CO_2 growth from economic activity, carbon intensity, and efficiency of natural sinks", P. Natl. Acad. USA. 104(47), 18866–18870, 2007, doi 10 1073/pnas 0702737104.

[45] M. Gloor, J. L. Sarmiento, and N. Gruber, "What can be learned about carbon cycle climate feedbacks from the CO_2 airborne fraction"? Atmos. Chem. Phys., 10, pp. 7739–7751, 2010. https://www.atmos-chem-phys net/10/7739/2010/, doi:10.5194/acp-10-7739-2010.

[46] A. P. Ballantyne, C. B. Alden, J. B. Miller, P. P. Tans, J. W. C. White, "Increase in observed net carbon dioxide uptake by land and oceans during the past 50 years", Nature 488, pp. 70-73, 2012. doi:10.1038/nature11299

[47] J. Steele, "How NOAA and Bad Modeling Invented an Ocean Acidification Icon", Part 2 – Bad Models, 2017. https://wattsupwiththat.com/2017/03/02/how-noaa-and-bad-modeling-invented-an-ocean-acidification-icon-part-2-bad-models/

[48] W. Evans, B. Hales, P. G. Strut, "Seasonal cycle of surface ocean pCO2 on the Oregon shelf", J. Geophys. Research 116, 2011, DOI: 10.1029/2010JC006625.

[49] K. R. Arrigo, G. L. van Dijken, "Continued increases in Arctic Ocean primary production", Progress in Oceanography 136, pp. 60-70, 2015, https://doi.org/10.1016/j.pocean.2015.05.002.

[50] D. K. Steinberg, M. W. Lomas, J. S. Cope, "Long-term increase in mesozooplankton biomass in the Sargasso Sea: Linkage to climate and implications for food web dynamics and biogeochemical cycling", Global Biogeochemical Cycle 26, 2012, DOI: 10.1029/2010GB004026.

[51] K. M. Krumhardt, N. S. Lovenduski, N. M. Freeman, N. R. Bates, "Apparent increase in coccolithophore abundance in the subtropical North Atlantic from 1990 to 2014", Biogeosciences 13, pp. 1163-1177, 2016. doi:10.5194/bg-13-1163-2016, http://www.biogeosciences net/13/1163/2016/.

[52] F. P. Chavez, M. Messié, J. T. Pennington, "Marine Primary Production in Relation to Climate Variability and Change", Annu. Rev. Mar. Sci. 3, pp. 227–260, 2011, doi:10.1146/annurev.marine.010908.163917.

[53] U. Riebesell, K. G. Schulz, R. G. J. Bellerby, M. Botros, P. Fritsche, M. Meyerhöfer, C. Neill, G. Nondal, A. Oschlies, J. Wohlers, E. Zöllner, "Enhanced biological carbon consumption in a high CO_2 ocean", Nature 450, pp. 545-548, 2007, doi:10.1038/nature06267.

[54] A. M. P. McDonnell, K. O. Buesseler, "Variability in the average sinking velocity of marine particles", Limnology and Oceanography 55, pp. 2085–2096, 2010. DOI:10.4319/lo.2010.55.5.2085.

[55] T. Weber, J. A. Cram, S. W. Leung, T. DeVries, C. Deutsch, "Deep ocean nutrients imply large latitudinal variation in particle transfer efficiency", PNAS 113 no. 31, pp. 8606–8611, 2016, doi: 10.1073/pnas.1604414113.

[56] F. Abrantes, P. Cermeno, C. Lopes, O. Romero, L. Matos, J. Van Iperen, M. Rufino, V. Magalhães, "Diatoms Si uptake capacity drives carbon export in coastal upwelling systems", Biogeosciences 13, pp. 4099–4109, 2016, https://doi.org/10.5194/bg-13-4099-2016

[57] M. Stuiver, H. A. Polach, "Discussion Reporting of ^{14}C Data", RADIOCARBON 19, No. 3, pp. 355-363, 1977.

On the decadal rates of sea level change during the twentieth century

S. J. Holgate[1]

Received 17 October 2006; accepted 21 November 2006; published 4 January 2007.

[1] Nine long and nearly continuous sea level records were chosen from around the world to explore rates of change in sea level for 1904–2003. These records were found to capture the variability found in a larger number of stations over the last half century studied previously. Extending the sea level record back over the entire century suggests that the high variability in the rates of sea level change observed over the past 20 years were not particularly unusual. The rate of sea level change was found to be larger in the early part of last century (2.03 ± 0.35 mm/yr 1904–1953), in comparison with the latter part (1.45 ± 0.34 mm/yr 1954–2003). The highest decadal rate of rise occurred in the decade centred on 1980 (5.31 mm/yr) with the lowest rate of rise occurring in the decade centred on 1964 (−1.49 mm/yr). Over the entire century the mean rate of change was 1.74 ± 0.16 mm/yr. **Citation:** Holgate, S. J. (2007), On the decadal rates of sea level change during the twentieth century, *Geophys. Res. Lett.*, *34*, L01602, doi:10.1029/2006GL028492.

1. Introduction

[2] In a previous paper, *Holgate and Woodwo th* [2004] (hereinafter referred to as HW04), rates of mean "global" sea level change (i.e., global coastal sea level change) were calculated from a large number of tide gauge records (177) for the period 1955–1998. HW04 found that the highest and lowest rates of change in the 1955–1998 period occurred in the last 20 years of the record. In this paper it is examined whether a few high quality tide gauge records can replace the many used by HW04. On the basis of these high quality records the work of HW04 is then extended back to the early twentieth century to examine whether the rates of sea level change experienced in recent decades are unusual.

[3] On a decadal timescale, the length scales of sea level change are very large (O(1000) km) though not necessarily global. As a result, many tide gauges in a given region are highly correlated with each other. This paper demonstrates that a few high quality records from around the world can be used to examine large spatial-scale decadal variability as well as many gauges from each region are able to.

2. Method

[4] When it comes to calculating long term global sea level means from tide gauge data, there are a number of problems. Firstly there is a bias in the distribution of tide gauges towards certain regions, notably Northern Europe and North America [*Douglas*, 1991]. Secondly there is the problem that not all tide gauge records are of equivalent quality. This can either be due to their location (being for example in an earthquake-prone region or an area of high glacial isostatic adjustment, GIA) or due to the quality of the instrumental record (being perhaps too discontinuous or lacking critical datum information to account for local vertical land movements).

[5] As a result of these two problems, there are very few high quality, long tide gauge records in different regions suitable for calculating global mean sea level change. An alternative approach is to make use of regional composites of shorter records as in HW04.

[6] In order to test whether a few high quality records could provide similar information to the composites, nine tide gauge records were carefully selected from the database of the Permanent Service for Mean Sea Level (PSMSL, available at http://www.p l.ac.uk/psmsl) [*Woodworth and Player*, 2003]: New York (1856–2003), Key West (1913–2003), San Diego (1906–2003), Balboa (1908–1996), Honolulu (1905–2003), Cascais (1882–1993), Newlyn (1915–2004) Trieste (1905–2004), and Auckland (1903–2000). The nine long records thus enable the study of HW04 into variability of decadal rates of sea level change to be extended over a much longer period. The locations of these tide gauge stations are shown in Figure 1.

[7] These tide gauge stations are part of the Revised Local Reference (RLR) data set of the PSMSL in which each time series is recorded relative to a consistent reference level on the nearby land. Annual values in the RLR data set of the PSMSL are only calculated if there are at least 11 months of data and each month must have less than 15 missing days. Hence the tide gauge data presented here is of the very highest quality available. All these records are almost continuous and are far away from regions with high rates of vertical land movement due to GIA or tectonics.

[8] Although most of these tide gauge records continue to the present, submissions of data to the PSMSL are often a year or two in arrears and hence most of these sea level records have data up until only 2003 or 2004. The current analysis begins in 1904 and ends in 2003 which ensures at least 70% completeness of the record in every decade.

[9] Following the method described in HW04, consecutive, overlapping decadal mean rates were calculated for each sea level record. The advantage of calculating decadal rates in this way is that the tide gauge records can then be combined into a single mean sea level time series, despite the different gauges having different datums. Furthermore, decadal rates remove any minor data discontinuities and introduce an element of smoothing. The rates of change at each station are corrected for GIA using the ICE-4G model of *Peltier* [2001] and for inverse barometer effects using the HadSLP2 air pressure data set [*Allan and Ansell*, 2006].

[10] The standard error of a sea level trend estimate, based on the assumption that each annual mean is inde-

[1]Proudman Oceanographic Laboratory, Liverpool, UK.

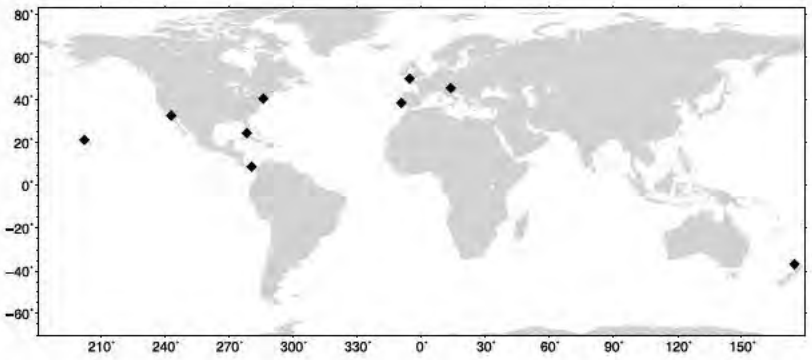

Figure 1. The distribution of the nine tide gauge records used in this study. Data are obtained from the Revised Local Reference data set of the Permanent Service for Mean Sea Level.

pendent, under-estimates the true error as the serial correlation is not accounted for [*Douglas*, 2001; *Nerem and Mitchum*, 2002]. Here serial correlation within each time-series is accommodated by reducing the number of degrees of freedom, using the lag-1 auto-correlation of the time-series [*World Meteorological Organization*, 1966; *Maul and Martin*, 1993]. The effect of calculating errors in this way increases one standard error for the trend over the 1904–2003 period from typically 0.02 mm/yr to 0.15 mm/yr.

3. Results

[11] Figure 2 compares the global decadal mean rates of change from the 177 stations of HW04 which were grouped into 13 regions (Figure 1 in HW04) with the global mean rates from the 9 long records. Although there are some differences between the two records, in particular the larger rate of rise in the 9 records during the 1950s, the two curves have overlapping error bars (based on one standard error). The global mean rates are similar for the second half of the 20th century (1953–97), 1.47 mm/yr and 1.41 mm/yr for the 177 and 9 stations respectively, with most of the disparity between the two due to differences in the 1950s. This comparison relies on using the HadSLP2 data set for pressure correction for both the 177 and 9 stations. HW04 used the NCEP pressure data set which gives a global mean rate for 177 stations of 1.64 mm/yr over the period 1953–97. Hence some uncertainty in the global mean rate of sea level rise is attributable to the commensurate uncertainty in the sea level pressure correction, which arises largely due to the difference in resolution between the two data sets (2.5° × 2.5° for NCEP and 5° × 5° for HadSLP2). Over the full 1904–2003 period, the mean global rate from the nine stations, corrected with HadSLP2, is 1.74 ± 0.16 mm/yr.

[12] Figure 3 shows that, not only is there considerable decadal variability in the individual sea level records, but there is generally little correlation between them. Stations which are in close proximity and which are affected by similar ocean and atmospheric processes show the greatest correlation. For example, Balboa and San Diego are both heavily influenced by the El Niño/Southern Oscillation (ENSO) and are similar (correlation of their decadal trends = 0.77), despite being over 4500 km apart. However, high correlation at a decadal scale does not imply that the long term trends are the same.

[13] The global mean sea level rates for the nine stations in Figure 2 show that the two highest decadal rates of change were recorded in the decades centred on 1980 (5.31 mm/yr) and 1939 (4.68 mm/yr) with the most negative decadal rates of change over the past 100 years during the decades centred on 1964 (−1.49 mm/yr) and 1987 (−1.33 mm/yr). There were also significant high decadal rates of change during the late 1910s, 1950s and 1990s. Negative decadal rates of change are seen in the early 1920s and early 1970s.

[14] Despite the high decadal rates of change in the latter part of the 20th century, it is found that the first half of the record (1904–1953) has a higher rate of rise overall (2.03 ± 0.35 mm/yr) than the 1954–2003 period which had a rate of 1.45 ± 0.34 mm/yr.

[15] The highest rates of sea level change over the common period for all gauges (1918–1996), occurred in New York (mean rate = 2.64 ± 0.44 mm/yr), San Diego (2.02 ± 0.31 mm/yr), Key West (2.00 ± 0.36 mm/yr) and

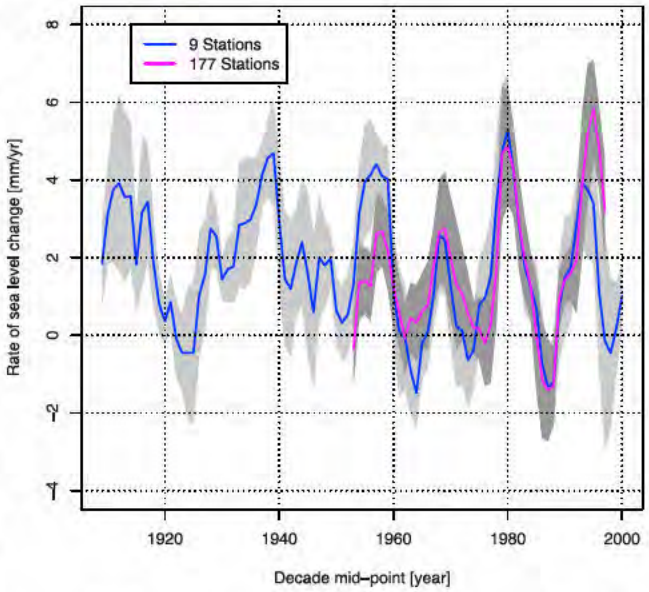

Figure 2. Comparison of the global mean decadal rates of sea level change based on the nine records with the rates from the 177 stations used in HW04. All rates are corrected for glacial isostatic adjustment and inverse barometer effects. The shaded region indicates ±1 standard error.

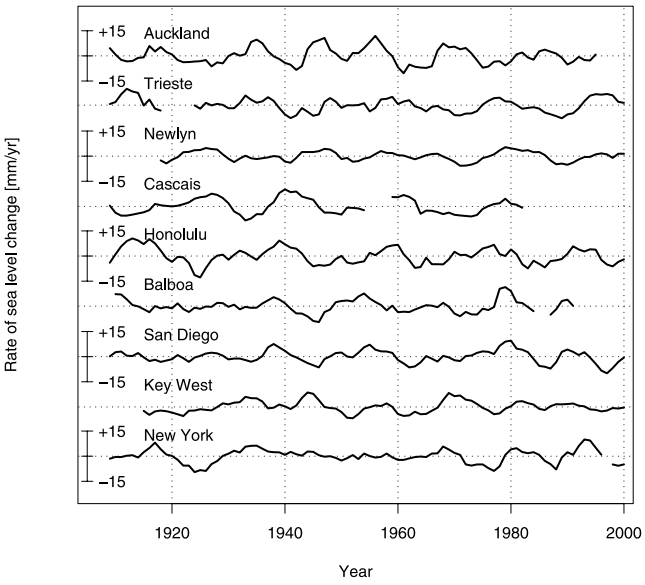

Figure 3. Comparison of the decadal rates of sea level change for each of the nine records. All rates are corrected for glacial isostatic adjustment and inverse barometer effects.

Cascais (1.85 ± 0.37 mm/yr). The smallest changes in sea level are seen in Trieste (1.25 ± 0.23 mm/yr) and Newlyn (1.46 ± 0.30 mm/yr).

[16] San Diego has the highest correlation with the global mean rates (r = 0.62) over the 1904–2003 period, followed by Honolulu (r = 0.58), New York (r = 0.56), Balboa (r = 0.55) and Trieste (r = 0.42). Cascais and Auckland have insignificant correlations at the 95% confidence level while the correlations with Newlyn (r = 0.29) and Key West (r = 0.25) are significant but low.

4. Discussion

[17] The nine stations selected here as high quality records capture the mean decadal rates of change described by the larger set of stations used in HW04 and also have a similar global mean rate over the common period of the two analyses (1953–1997). This provides confidence that the nine station set can be used to study decadal rates of global mean sea level change throughout the twentieth century.

[18] All the stations in this study show a significant increase in sea level over the period 1904–2003 with an average increase of 174 mm during that time (Figure 4). This mean rate of 1.74 mm/yr is at the upper end of the range of estimates for the 20th century in the Intergovernmental Panel on Climate Change, Third Assessment Report (IPCC TAR) [*Church et al.*, 2001], and consistent with other recent estimates [*Holgate and Woodworth*, 2004; *Church and White*, 2006].

[19] The rates for individual stations are consistent with those published by other authors [*Douglas*, 2001; *Peltier*, 2001; *Hannah*, 1990]. As has been noted previously [*Woodworth*, 1990], the rates for northern European tide gauges are consistently lower than the global mean. Trieste, along with other Mediterranean tide gauge stations, has shown a much lower rate of increase since 1960 [*Douglas*, 1997; *Tsimplis and Baker*, 2000]. However, the difference between the global mean and Trieste is 0.49 in comparison with the difference between the global mean and New York (the highest individual rate) which is 0.62. It would therefore seem that Trieste no more biases the mean low than New York biases the mean high. Nevertheless, excluding Trieste from the results would slightly increase the global mean from 1.74 to 1.80 mm/yr.

[20] Although the mean rate of change of global mean sea level is found to be greater in the first half of the twentieth century, the two rates are consistent with being the same at the 95% confidence level, given their individual standard errors. However, a greater rate of rise in the early part of the record is consistent with previous analyses of tide gauge records which suggested a general deceleration in sea level rise during the 20th century [*Woodworth*, 1990; *Douglas*, 1992; *Jevrejeva et al.*, 2006]. A twentieth century deceleration is consistent with the work of *Church and White* [2006] who, although finding evidence for a post-1870 acceleration based on an EOF reconstruction of global sea level, found that much of the overall acceleration occurred in the first half of the 20th century. *Church and White* [2006] suggested that the greater rate of sea level rise observed in the first half of last century was due to reduced volcanic emissions (and hence also lower variability in sea level) during the 1930s to 1960s. This idea is supported by results from the HadCM3 model which suggest that the simulated global mean sea level did not accelerate through the twentieth century due to the offsetting of anthropogenic warming by reduced natural forcing [*Gregory et al.*, 2006].

[21] The decadal rates of sea level change shown in Figure 2 are qualitatively similar to the corresponding rates in Figure 2 of *Church and White* [2006], with the exception of the period 1930–1940 which shows lower variability in the work of *Church and White* [2006]. The variability in the second half of the century is also similar to that found by

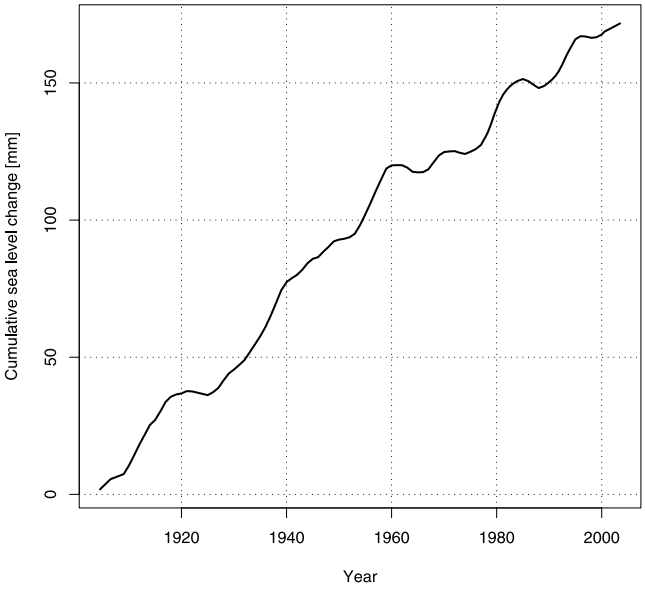

Figure 4. The mean sea level record from the nine tide gauges over the period 1904–2003 based on the decadal trend values for 1907–1999. The sea level curve here is the integral of the rates presented in Figure 2.

Chambers et al. [2002] though the lower number of gauges in the present study results in a greater level of variance.

5. Summary and Conclusions

[22] Based on a selection of nine long, high quality tide gauge records, the mean rate of sea level rise over the period 1904–2003 was found to be 1.74 ± 0.16 mm/yr after correction for GIA using the ICE-4G model [*Peltier*, 2001] and for inverse barometer effects using HadSLP2 [*Allan and Ansell*, 2006]. The mean rate of rise was greater in the first half of this period than the latter half, though the difference in rates was not found to be significant. The use of a reduced number of high quality sea level records was found to be as suitable in this type of analysis as using a larger number of regionally averaged gauges.

[23] Finally, in extending the work of HW04 to cover the whole century, it is found that the high decadal rates of change in global mean sea level observed during the last 20 years of the record were not particularly unusual in the longer term context.

[24] **Acknowledgments.** I'd like to thank Phil Woodworth, Simon Williams, and Svetlana Jevrejeva for discussion and comments which have helped to improve this paper.

References

Allan, R., and T. Ansell (2006), A new globally complete monthly historical mean sea level pressure data set (HadSLP2): 1850 2004, *J. Clim*, in press.

Chambers, D. P., C. A. Mehlhaff, T. J. Urban, D. Fujii, and R. S. Ner m (2002), Low-frequency variations in global mean sea level: 1950 2000, *J. Geophys. Res.*, *107*(C4), 3026, doi:10.1029/2001JC001089.

Church, J. A., and N. J. White (2006), A 20th century acceleration in global sea level rise, *Geophys. Res. Lett.*, *33*, L01602, doi:10.1029/2005GL024826.

Church, J. A., J. Gregory, P. Huybrechts, M. Kuhn, K. Lambeck, M. Nhuan, D. Qin, and P. Woodworth (2001), Changes in sea level, in *Climate Change 2001: The Scientific Basis: Contribution of Working Group to the Third Assessment Report of the Intergovernmental Panel on Climate Change*, edited by J. T. Houghton et al., chap. 11, pp. 639 694, Cambridge Univ. Press, New York.

Douglas, B. C. (1991), Global sea level rise, *J. Geophys. Res.*, *96*, 6981 6992.

Douglas, B. C. (1992), Global sea level acceleration, *J. Geophys. Res.*, *97*, 12,699 12,706.

Douglas, B. C. (1997), Global sea rise: A redetermination, *Surv. Geophys.*, *18*, 279 292.

Douglas, B. C. (2001), Sea level change in the era of the recording tide gauge, in *Sea Level Rise: History and Consequences*, *Int. Geophys. Ser.*, vol. 75, edited by B. C. Douglas, M. S. Kearney, and S. P. Leatherman, chap. 3, pp. 37 64, Elsevier, New York.

Gregory, J., J. Lowe, and S. Tett (2006), Simulated global-mean sea-level changes over the last half-millenium, *J. Clim.*, *19*, 4576 4591.

Hannah, J. (1990), Analysis of mean sea level data from New Zealand for the period 1899 1988, *J. Geophys. Res.*, *95*, 12,399 12,405.

Holgate, S. J., and P. L. Woodworth (2004), Evidence for enhanced coastal sea level rise during the 1990s, *Geophys. Res. Lett.*, *31*, L07305, doi:10.1029/2004GL019626.

Jevrejeva, S., A. Grinsted, J. C. Moore, and S. Holgate (2006), Nonlinear trends and multi-year cycles in sea level trends, *J. Geophys. Res.*, *111*, C09012, doi:10.1029/2005JC003229.

Maul, G. A., and D. M. Martin (1993), Sea level rise at Key West, Florida, 1846 1992: America's longest ins rument record?, *Geophys. Res. Lett.*, *20*, 1955 1958.

Nerem, R. S., and G. T. Mitchum (2002), Estimates of vertical crustal motion derived from differences of TOPEX/POSEIDON and tide gauge sea level measurements, *Geophys. Res. Lett.*, *29*(19), 1934, doi:10.1029/2002GL015037.

Peltier, W. (2001), Global glacial isostatic adjustment and modern instrumental records of relative s a level history, in *Sea Level Rise: History and Consequences*, *Int. Geophys. Ser.*, vol. 75, edited by B. C. Douglas, M. S. Kearney, a d S. P. Leath rman, chap. 4, pp. 65 95, Elsevier, New York.

Tsimplis, M. N., and T. F. Baker (2000), Sea level drop in the Mediterranean Sea: An indicator of deep water salinity and temperature changes?, *G phys. Res. Lett.*, *27*, 1731 1734.

Woodworth, P. (1990), A search for accelerations in records of European mean sea level, *Int. J. Climatol.*, *10*, 129 143.

Woodworth, P., and R. Player (2003), The Permanent Service for Mean Sea Level: An update to the 21st century, *J. Coastal Res.*, *19*(2), 287 295.

World Meteorological Organization (1966) Report of a working group on the commission for climatology, *Tech. Rep. 79*, 79 pp., World Meteorol. Organ., Geneva, Switzerland.

S. J. Holgate, Proudman Oceanographic Laboratory, Joseph Proudman Building, 6 Brownlow Street, Liverpool L3 5DA, UK. (simonh@pol.ac.uk)

Environment Pollution and Climate Change

Nikolov and Zeller, Environ Pollut Climate Change 2017, 1:2

Research Article OMICS International

New Insights on the Physical Nature of the Atmospheric Greenhouse Effect Deduced from an Empirical Planetary Temperature Model

Ned Nikolov* **and Karl Zeller**

Ksubz LLC, 9401 Shoofly Lane, Wellington CO 80549, USA

Abstract

A recent study has revealed that the Earth's natural atmospheric greenhouse effect is around 90 K or about 2.7 times stronger than assumed for the past 40 years. A thermal enhancement of such a magnitude cannot be explained with the observed amount of outgoing infrared long-wave radiation absorbed by the atmosphere (i.e. ≈ 158 W m^{-2}), thus requiring a re-examination of the underlying Greenhouse theory. We present here a new investigation into the physical nature of the atmospheric thermal effect using a novel empirical approach toward predicting the Global Mean Annual near-surface equilibrium Temperature (GMAT) of rocky planets with diverse atmospheres. Our method utilizes Dimensional Analysis (DA) applied to a vetted set of observed data from six celestial bodies representing a broad range of physical environments in our Solar System, i.e. Venus, Earth, the Moon, Mars, Titan (a moon of Saturn), and Triton (a moon of Neptune). Twelve relationships (models) suggested by DA are explored via non-linear regression analyses that involve dimensionless products comprised of solar irradiance, greenhouse-gas partial pressure/density and total atmospheric pressure/density as forcing variables, and two temperature ratios as dependent variables. One non-linear regression model is found to statistically outperform the rest by a wide margin. Our analysis revealed that GMATs of rocky planets with tangible atmospheres and a negligible geothermal surface heating can accurately be predicted over a broad range of conditions using only two forcing variables: top-of-the-atmosphere solar irradiance and total surface atmospheric pressure. The hereto discovered interplanetary pressure-temperature relationship is shown to be statistically robust while describing a smooth physical continuum without climatic tipping points. This continuum fully explains the recently discovered 90 K thermal effect of Earth's atmosphere. The new model displays characteristics of an emergent macro-level thermodynamic relationship heretofore unbeknown to science that has important theoretical implications. A key entailment from the model is that the atmospheric 'greenhouse effect' currently viewed as a radiative phenomenon is in fact an adiabatic (pressure-induced) thermal enhancement analogous to compression heating and independent of atmospheric composition. Consequently, the global down-welling long-wave flux presently assumed to drive Earth's surface warming appears to be a product of the air temperature set by solar heating and atmospheric pressure. In other words, the so-called 'greenhouse back radiation' is globally a result of the atmospheric thermal effect rather than a cause for it. Our empirical model has also fundamental implications for the role of oceans, water vapour, and planetary albedo in global climate. Since produced by a rigorous attempt to describe planetary temperatures in the context of a cosmic continuum using an objective analysis of vetted observations from across the Solar System, these findings call for a paradigm shift in our understanding of the atmospheric 'greenhouse effect' as a fundamental property of climate.

Keywords: Greenhouse effect; Emergent model; Planetary temperature; Atmospheric pressure; Greenhouse gas; Mars temperature

Introduction

In a recent study Volokin and ReLlez [1] demonstrated that the strength of Earth's atmospheric Greenhouse Effect (GE) is about 90 K instead of 33 K as presently assumed by most researchers [2-7]. The new estimate corrected a long-standing mathematical error in the application of the Stefan–Boltzmann (SB) radiation law to a sphere pertaining to Hölder's inequality between integrals. Since the current greenhouse theory strives to explain GE solely through a retention (trapping) of outgoing long-wavelength (LW) radiation by atmospheric gases [2,5,7-10], a thermal enhancement of 90 K creates a logical conundrum, since satellite observations constrain the global atmospheric LW absorption to 155–158 W m^{-2} [11-13]. Such a flux might only explain a surface warming up to 35 K. Hence, more than 60% of Earth's 90 K atmospheric effect appears to remain inexplicable in the context of the current theory. Furthermore, satellite- and surface-based radiation measurements have shown [12-14] that the lower troposphere emits 42-44% more radiation towards the surface (i.e. 341-346 W m^{-2}) than the net shortwave flux delivered to the Earth-atmosphere system by the Sun (i.e. 240 W m^{-2}). In other words, the lower troposphere contains significantly more kinetic energy than expected from solar heating alone, a conclusion also supported by the new 90 K GE estimate. A similar but more extreme situation is observed on Venus as well, where the atmospheric down-welling LW radiation near the surface (>15,000 W m^{-2}) exceeds the total absorbed solar flux (65–150 W m^{-2}) by a factor of 100 or more [6]. The radiative greenhouse theory cannot explain this apparent paradox considering the fact that infrared-absorbing gases such as CO_2, water vapor and methane only re-radiate available LW emissions and do not constitute significant heat storage or a net source of additional energy to the system. This raises a fundamental question about the origin of the observed energy surplus in the lower troposphere of terrestrial planets with respect to the solar input. The above inconsistencies between theory and observations prompted us to take a new look at the mechanisms controlling the atmospheric thermal effect.

We began our study with the premise that processes controlling the Global Mean Annual near-surface Temperature (GMAT) of Earth are also responsible for creating the observed pattern of planetary temperatures across the Solar System. Thus, our working hypothesis was that a general physical model should exist, which accurately describes equilibrium GMATs of planets using a common set of drivers. If true, such a model would also reveal the forcing behind the atmospheric thermal effect.

Instead of examining existing mechanistic models such as 3-D

***Corresponding author:** Ned Nikolov, Ksubz LLC, 9401 Shoofly Lane, Wellington CO 80549, USA, Tel: 970-980-3303, 970-206-0700; E-mail: ntconsulting@comcast.net

Received November 11, 2016; **Accepted** February 06, 2017; **Published** February 13, 2017

Citation: Nikolov N, Zeller K (2017) New Insights on the Physical Nature of the Atmospheric Greenhouse Effect Deduced from an Empirical Planetary Temperature Model. Environ Pollut Climate Change 1: 112

GCMs, we decided to try an empirical approach not constrained by a particular physical theory. An important reason for this was the fact that current process-oriented climate models rely on numerous theoretical assumptions while utilizing planet-specific parameterizations of key processes such as vertical convection and cloud nucleation in order to simulate the surface thermal regime over a range of planetary environments [15]. These empirical parameterizations oftentimes depend on detailed observations that are not typically available for planetary bodies other than Earth. Hence, our goal was to develop a simple yet robust planetary temperature model of high predictive power that does not require case-specific parameter adjustments while successfully describing the observed range of planetary temperatures across the Solar System.

Methods and Data

In our model development we employed a 'top-down' empirical approach based on Dimensional Analysis (DA) of observed data from our Solar System. We chose DA as an analytic tool because of its ubiquitous past successes in solving complex problems of physics, engineering, mathematical biology, and biophysics [16-21]. To our knowledge DA has not previously been applied to constructing predictive models of macro-level properties such as the average global temperature of a planet; thus, the following overview of this technique is warranted.

Dimensional analysis background

DA is a method for extracting physically meaningful relationships from empirical data [22-24]. The goal of DA is to restructure a set of original variables deemed critical to describing a physical phenomenon into a smaller set of independent dimensionless products that may be combined into a dimensionally homogeneous model with predictive power. Dimensional homogeneity is a prerequisite for any robust physical relationship such as natural laws. DA distinguishes between measurement units and physical dimensions. For example, mass is a physical dimension that can be measured in gram, pound, metric ton etc.; time is another dimension measurable in seconds, hours, years, etc. While the physical dimension of a variable does not change, the units quantifying that variable may vary depending on the adopted measurement system.

Many physical variables and constants can be described in terms of four fundamental dimensions, i.e. mass [M], length [L], time [T], and absolute temperature [Θ]. For example, an energy flux commonly measured in W m^{-2} has a physical dimension [M T^{-3}] since 1 W m^{-2} = 1 J s^{-1} m^{-2} = 1 (kg m^2 s^{-2}) s^{-1} m^{-2} = kg s^{-3}. Pressure may be reported in units of Pascal, bar, atm., PSI or Torr, but its physical dimension is always [M L^{-1} T^{-2}] because 1 Pa = 1 N m^{-2} = 1 (kg m s^{-2}) m^{-2} = 1 kg m^{-1} s^{-2}. Thinking in terms of physical dimensions rather than measurement units fosters a deeper understanding of the underlying physical reality. For instance, a comparison between the physical dimensions of energy flux and pressure reveals that a flux is simply the product of pressure and the speed of moving particles [L T^{-1}], i.e. [M T^{-3}] = [M L^{-1} T^{-2}] [L T^{-1}]. Thus, a radiative flux F_R (W m^{-2}) can be expressed in terms of photon pressure P_{ph} (Pa) and the speed of light c (m s^{-1}) as $F_R = c\,P_{ph}$. Since c is constant within a medium, varying the intensity of electromagnetic radiation in a given medium effectively means altering the pressure of photons. Thus, the solar radiation reaching Earth's upper atmosphere exerts a pressure (force) of sufficient magnitude to perturb the orbits of communication satellites over time [25,26].

The simplifying power of DA in model development stems from the Buckingham Pi Theorem [27], which states that a problem involving n dimensioned x_i variables, i.e.

$$f(x_1, x_2, \ldots, x_n) = 0$$

can be reformulated into a simpler relationship of (n-m) dimensionless π_i products derived from x_i, i.e.

$$\phi(\pi_1, \pi_2, \ldots, \pi_{n-m}) = 0$$

where m is the number of fundamental dimensions comprising the original variables. This theorem determines the number of non-dimensional π_i variables to be found in a set of products, but it does not prescribe the number of sets that could be generated from the original variables defining a particular problem. In other words, there might be, and oftentimes is more than one set of (n-m) dimensionless products to analyze. DA provides an objective method for constructing the sets of π_i variables employing simultaneous equations solved via either matrix inversion or substitution [22].

The second step of DA (after the construction of dimensionless products) is to search for a functional relationship between the π_i variables of each set using regression analysis. DA does not disclose the best function capable of describing the empirical data. It is the investigator's responsibility to identify a suitable regression model based on prior knowledge of the phenomenon and a general expertise in the subject area. DA only guarantees that the final model (whatever its functional form) will be dimensionally homogeneous, hence it may qualify as a physically meaningful relationship provided that it (*a*) is not based on a simple polynomial fit; (*b*) has a small standard error; (*c*) displays high predictive skill over a broad range of input data; and (*d*) is statistically robust. The regression coefficients of the final model will also be dimensionless, and may reveal true constants of Nature by virtue of being independent of the units utilized to measure the forcing variables.

Selection of model variables

A planet's GMAT depends on many factors. In this study, we focused on drivers that are remotely measurable and/or theoretically estimable. Based on the current state of knowledge we identified seven physical variables of potential relevance to the global surface temperature: 1) top-of-the-atmosphere (TOA) solar irradiance (S); 2) mean planetary surface temperature in the absence of atmospheric greenhouse effect, hereto called a reference temperature (T_r); 3) near-surface partial pressure of atmospheric greenhouse gases (P_{gh}); 4) near-surface mass density of atmospheric greenhouse gases (ρ_{gh}); 5) total surface atmospheric pressure (P); 6) total surface atmospheric density (ρ); and 7) minimum air pressure required for the existence of a liquid solvent at the surface, hereto called a reference pressure (P_r). Table 1 lists the above variables along with their SI units and physical dimensions. Note that, in order to simplify the derivation of dimensionless products, pressure and density are represented in Table 1 by the generic variables P_x and ρ_x, respectively. As explained below, the regression analysis following the construction of π_i variables explicitly distinguished between models involving partial pressure/density of greenhouse gases and those employing total atmospheric pressure/density at the surface. The planetary Bond albedo (α_p) was omitted as a forcing variable in our DA despite its known effect on the surface energy budget, because it is already dimensionless and also partakes in the calculation of reference temperatures discussed below.

Appendix A details the procedure employed to construct the π_i variables. DA yielded two sets of π_i products, each one consisting of two

Planetary Variable	Symbol	SI Units	Physical Dimension
Global mean annual near-surface temperature (GMAT), the dependent variable	T_s	K	[Θ]
Stellar irradiance (average shortwave flux incident on a plane perpendicular to the stellar rays at the top of a planet s atmosphere)	S	W m^{-2}	[M T^{-3}]
Reference temperature (the planet's mean surface temperature in the absence of an atmosphere or an atmospheric greenhouse effect)	T_r	K	[Θ]
Average near-surface gas pressure representing either partial pressure of greenhouse gases or total atmospheric pressure	P_x	Pa	[M L^{-1} T^{-2}]
Average near-surface gas density representing either greenhouse-gas density or total atmospheric density	ρ_x	kg m^{-3}	[M L^{-3}]
Reference pressure (the minimum atmospheric pressure required a liquid solvent to exists at the surface)	P_r	Pa	[M L^{-1} T^{-2}]

Table 1: Variables employed in the Dimensional Analysis aimed at deriving a general planetary temperature model. The variables are comprised of 4 fundamental physical dimensions: mass [M], length [L], time [T] and absolute temperature [Θ].

dimensionless variables, i.e.

$$\pi_1 = \frac{T_s}{T_r}; \qquad \pi_2 = \frac{P_x^3}{\rho_x S^2}$$

and

$$\pi_1 = \frac{T_s}{T_r}; \qquad \pi_2 = \frac{P_x}{P_r}$$

This implies an investigation of two types of dimensionally homogeneous functions (relationships):

$$\frac{T_s}{T_r} = f\left(\frac{P_x^3}{\rho_x S^2}\right) \tag{1}$$

and

$$\frac{T_s}{T_r} = f\left(\frac{P_x}{P_r}\right) \tag{2}$$

Note that $\pi_1 = T_s/T_r$ occurs as a dependent variable in both relationships, since it contains the sought temperature T_s. Upon replacing the generic pressure/density variables P_x and ρ_x in functions (1) and (2) with either partial pressure/density of greenhouse gases (P_{gh} and ρ_{gh}) or total atmospheric pressure/density (P and ρ), one arrives at six prospective regression models. Further, as explained below, we employed two distinct kinds of reference temperature computed from different formulas, i.e. an effective radiating equilibrium temperature (T_e) and a mean 'no-atmosphere' spherical surface temperature (T_{na}). This doubled the π_i instances in the regression analysis bringing the total number of potential models for investigation to twelv

Reference temperatures and reference pressure

A reference temperature (T_r) characterizes the average thermal environment at the surface of a planetary body in the absence of atmospheric greenhouse effect; hence, T_r is different for each body and depends on solar irradiance and surface albedo. The purpose of T_r is to provide a baseline for quantifying the thermal effect of planetary atmospheres. Indeed, the T_s/T_r ratio produced by DA can physically be interpreted as a Relative Atmospheric Thermal Enhancement (RATE) ideally expected to be equal to or greater than 1.0. Expressing the thermal effect of a planetary atmosphere as a non-dimensional quotient instead of an absolute temperature difference (as done in the past) allows for an unbiased comparison of the greenhouse effects of celestial bodies orbiting at different distances from the Sun. This is because the absolute strength of the greenhouse effect (measured in K) depends on both solar insolation and atmospheric properties, while RATE being a radiation-normalized quantity is expected to only be a function of a planet's atmospheric environment. To our knowledge, RATE has not previously been employed to measure the thermal effect of planetary atmospheres.

Two methods have been proposed thus far for estimating the average surface temperature of a planetary body without the greenhouse effect, both based on the SB radiation law. The first and most popular approach uses the planet's global energy budget to calculate a single radiating equilibrium temperature T_e (also known as an effective emission temperature) from he average absorbed solar flux [6,9,28], i.e.

$$T_e = \left[\frac{S(1-\alpha_p)}{4\varepsilon\sigma}\right]^{0.25} \tag{3}$$

Here, S is the solar irradiance (W m^{-2}) defined as the TOA shortwave flux incident on a plane perpendicular to the incoming rays, α_p is he planetary Bond albedo (decimal fraction), ε is the planet's LW emissivity (typically $0.9 \leq \varepsilon < 1.0$; in this study we assume $\varepsilon = 0.98$ b sed on lun r regolith measurements reported by Vasavada et al. [29], and $\sigma = 5.6704 \times 10^{-8}$ W m^{-2} K^{-4} is the SB constant. The term $S(1-\alpha_p)/4$ represents a globally averaged shortwave flux absorbed by the planet-atmosphere system. The rationale behind Eq. (3) is that the TOA energy b l nce presumably defines a baseline temperature at a certain height in he free atmosphere (around 5 km for Earth), which is related to the planet's mean surface temperature via the infrared optical depth of the atmosphere [9,10]. Equation (3) was introduced to planetary science in the early 1960s [30,31] and has been widely utilized ever since to calculate the average surface temperatures of airless (or nearly airless) bodies such as Mercury, Moon and Mars [32] as well as to quantify the strength of the greenhouse effect of planetary atmospheres [2-4,6,9,28]. However, Volokin and ReLlez [1] showed that, due to Hölder's inequality between integrals [33], T_e is a non-physical temperature for spheres and lacks a meaningful relationship to the planet's T_s.

The second method attempts to estimate the average surface temperature of a planet (T_{na}) in the complete absence of an atmosphere using an explicit spatial integration of the SB law over a sphere. Instead of calculating a single bulk temperature from the average absorbed shortwave flux as done in Eq. (3), this alternative approach first computes the equilibrium temperature at every point on the surface of an airless planet from the local absorbed shortwave flux using the SB relation, and then spherically integrates the resulting temperature field to produce a global temperature mean. While algorithmically opposite to Eq. (3), this method mimics well the procedure for calculating Earth's global temperature as an area-weighted average of surface observations.

Rubincam [34] proposed an analytic solution to the spherical integration of the SB law (his Eq. 15) assuming no heat storage by the regolith and zero thermal inertia of the ground. Volokin and ReLlez [1] improved upon Rubincam's formulation by deriving a closed-form integral expression that explicitly accounts for the effect of subterranean heat storage, cosmic microwave background radiation (CMBR) and geothermal heating on the average global surface temperature of airless bodies. The complete form of their analytic Spherical Airless-Temperature (SAT) model reads:

$$T_{na} = \frac{2}{5}\left\{\frac{\left[(1-\eta_e)S(1-\alpha_e)+R_c+R_g\right]^{5/4}-\left(R_C+R_g\right)^{5/4}}{(1-\eta_e)S(1-\alpha_e)(\varepsilon\sigma)^{1/4}}+\frac{\left[0.754\eta_e S(1-\alpha_e)+R_c+R_g\right]^{5/4}-\left(R_C+R_g\right)^{5/4}}{0.754\eta_e S(1-\alpha_e)(\varepsilon\sigma)^{1/4}}\right\} \quad (4a)$$

where α_e is the effective shortwave albedo of the surface, η_e is the effective ground heat storage coefficient in a vacuum, $R_c = \sigma\, 2.725^4 = 3.13 \times 10^{-6}$ W m^{-2} is the CMBR [35], and R_g is the spatially averaged geothermal flux (W m^{-2}) emanating from the subsurface. The heat storage term η_e is defined as a fraction of the absorbed shortwave flux conducted into the subsurface during daylight hour and subsequently released as heat at night.

Since the effect of CMBR on T_{na} is negligible for $S > 0.15$ W m^{-2} [1] and the geothermal contribution to surface temperatures is insignificant for most planetary bodies, one can simplify Eq. (4a) by substituting $R_c = R_g = 0$ This produces:

$$T_{na} = \frac{2}{5}\left[\frac{S(1-\alpha_e)}{\varepsilon\sigma}\right]^{0.25}\left[(1-\eta_e)^{0.25}+0.932\eta_e^{0.25}\right] \quad (4b)$$

where $0.932 = 0.754^{0.25}$. The complete formula (4a) must only be used if $S \le 0.15$ W m^{-2} and/or the magnitude of R_g is significantly greater than zero. For comparison, in the Solar System, the threshold $S \le 0.15$ W m^{-2} is encountered beyond 95 astronomical unis (AU) in the region of the inner Oort cloud. Volokin and ReLlez [1] verified Equations (4a) and (4b) against Moon temperature data provided by the NASA Diviner Lunar Radiometer Experiment [29,36]. These authors also showed that accounting for the subterranean heat storage (η_e) markedly improves the physical realism and accuracy of the SAT model compared to the original formulation by Rubincam [34].

The conceptual difference between Equations (3) and (4b) is that T_e represents the equilibrium temperature of a blackbody disk orthogonally illuminated by shortwave radiation with an intensity equal to the average solar flux absorbed by a sphere having a Bond albedo α_p, while T_{na} is the area-weighted average temperature of a thermally heterogeneous airless sphere [1,37]. In other words, for spherical objects T_e is an abstract mathematical temperature, while T_{na} is the average kinetic temperature of an airless surface. Due to Hölder's inequality between integrals, one always finds $T_e >> T_{na}$ when using equivalent values of stellar irradiance and surface albedo in Equations (3) and (4b) [1].

To calculate the T_{na} temperatures for planetary bodies with tangible atmospheres, we assumed that the airless equivalents of such objects would be covered with a regolith of similar optical and thermo-physical properties as the Moon surface. This is based on the premise that, in the absence of a protective atmosphere, the open cosmic environment would erode and pulverize exposed surfaces of rocky planets over time in a similar manner [1]. Also, properties of the Moon surface are the best studied ones among all airless bodies in the Solar System. Hence, one could further simplify Eq. (4b) by combining the albedo, the heat storage fraction and the emissivity parameter into a single constant using applicable values for the Moon, i.e. $\alpha_e = 0.132$, $\eta_e = 0.00971$ and $\varepsilon = 0.98$ [1,29]. This produces:

$$T_{na} = 32.44\, S^{0.25} \quad (4c)$$

Equation (4c) was employed to estimate the 'no-atmosphere' reference temperatures of all planetary bodies participating in our analysis and discussed below.

For a reference pressure, we used the gas-liquid-solid triple point of water, i.e. $P_r = 611.73$ Pa [38] defining a baric threshold, below which water can only exists in a solid/vapor phase and not in a liquid form. The results of our analysis are not sensitive to the particular choice of a reference-pressure value; hence, the selection of P_r is a matter of convention.

Regression analysis

Finding the best function to describe the observed variation of GMAT among celestial bodies requires that the π_i variables generated by DA be subjected to regression analyses. As explained in Appendix A, twelve pairs of π_i variables hereto called Models were investigated. In order to ease the curve fitting and simplify the visualization of results, we utilized natural logarithms of the constructed π_i variable rather than their absolute values, i.e. we modeled the relationship $\ln(\pi_1) = f(\ln(\pi_2))$ instead of $\pi_1 = f(\pi_2)$. In doing so we focused on monotonic functions of conservative shapes such as exponential, sigmoidal, hyperbolic, and logarithmic, for their fitting coefficients might be interpretable in physically meaningful terms. A key advantage of this type of functions (provided the existence of a good fit, of course) is that they also tend to yield reliable results outside the data range used to determine their coefficients. We specifically avoided non-monotonic functions such as polynomials because of their ability to accurately fit almost any dataset given a sufficiently large number of regression coefficients while at the same time showing poor predictive skills beyond the calibration data range. Due to their highly flexible shape, polynomials can easily fit random noise in a dataset, an outcome we particularly tried to avoid.

The following four-parameter exponential-growth function was found to best meet our criteria:

$$y = a\exp(bx) + c\exp(dx) \quad (5)$$

where $x = \ln(\pi_2)$ and $y = \ln(\pi_1)$ are the independent and dependent variable respectively while *a, b, c* and *d* are regression coefficients. This function has a rigid shape that can only describe specific exponential patterns found in our data. Equation (5) was fitted to each one of the 12 planetary data sets of logarithmic π_i pairs suggested by DA using the standard method of least squares. The skills of the resulting regression models were evaluated via three statistical criteria: coefficient of determination (R^2), adjusted R^2, and standard error of the estimate (σ_{est}) [39,40]. All calculations were performed with SigmaPlot™ 13 graphing and analysis software.

Planetary data

To ensure proper application of the DA methodology we compiled a dataset of diverse planetary environments in the Solar System using the best information available. Celestial bodies were selected for the analysis based on three criteria: (*a*) presence of a solid surface; (*b*) availability of reliable data on near-surface temperature, atmospheric composition, and total air pressure/density preferably from direct observations; and (*c*) representation of a broad range of physical environments defined in terms of TOA solar irradiance and atmospheric properties. This resulted in the selection of three planets: Venus, Earth, and Mars; and three natural satellites: Moon of Earth, Titan of Saturn, and Triton of Neptune.

Each celestial body was described by nine parameters shown in Table 2 with data sources listed in Table 3. In an effort to minimize the effect of unforced (internal) climate variability on the derivation of our temperature model, we tried to assemble a dataset of means representing an observational period of 30 years, i.e. from 1981 to 2010. Thus, Voyager measurements of Titan from the early 1980s suggested an average surface temperature of 94 ± 0.7 K [41]. Subsequent observations by the Cassini mission between 2005 and 2010 indicated a mean global temperature of 93.4 ± 0.6 K for that moon [42,43]. Since

Parameter	Venus	Earth	Moon	Mars	Titan	Triton
Average distance to the Sun, r_{au} (AU)	0.7233	1.0	1.0	1.5237	9.582	30.07
Average TOA solar irradiance, S (W m^{-2})	2,601.3	1,360.9	1,360.9	586.2	14.8	1.5
Bond albedo, α_p (decimal fraction)	0.900	0.294	0.136	0.235	0.265	0.650
Average absorbed shortwave radiation, $S_a = S(1-\alpha_p)/4$ (W m^{-2})	65.0	240.2	294.0	112.1	2.72	0.13
Global average surface atmospheric pressure, P (Pa)	9,300,000.0 ± 100,000	98,550.0 ± 6.5	$2.96 \times 10^{-10} \pm 10^{-10}$	685.4 ± 14.2	146,700.0 ± 100	4.0 ± 1.2
Global average surface atmospheric density, ρ (kg m^{-3})	65 868 ± 0.44	1.193 ± 0.002	$2.81 \times 10^{-15} \pm 9.4 \times 10^{-15}$	$0.019 \pm 3.2 \times 10^{-4}$	5.161 ± 0.03	$3.45 \times 10^{-4} \pm 9.2 \times 10^{-5}$
Chemical composition of the lower atmosphere (% of volume)	96.5 CO_2 3.48 N_2 0.02 SO_2	77.89 N_2 20.89 O_2 0.932 Ar 0.248 H_2O 0.040 CO_2	26.7 ^{4}He 26.7 ^{20}Ne 23.3 H_2 20.0 ^{40}Ar 3.3 ^{22}Ne	95.32 CO_2 2.70 N_2 1.60 Ar 0.13 O_2 0.08 CO 0.021 H_2O	95.1 N_2 4.9 CH_4	99.91 N_2 0.060 CO 0.024 CH_4
Molar mass of the lower atmosphere, M (kg mol^{-1})	0.0434	0.0289	0.0156	0.0434	0.0274	0.0280
GMAT, T_s (K)	737.0 ± 3.0	287.4 ± 0.5	197.35 ± 0.9	190.56 ± 0.7	93.7 ± 0.6	39.0 ± 1 0

Table 2: Planetary data set used in the Dimensional Analysis compiled from sources listed in Table 3. The estimation of Mars' GMAT and the average surface atmospheric pressure are discussed in Appendix B. See text for details about the computational methods employed for some parameters.

Planetary Body	Information Sources
Venus	[32,44-48]
Earth	[12,13,32,49-55]
Moon	[1,29,32,48,56-59]
Mars	[32,48,60-63], Appendix B
Titan	[32,41-43,64-72]
Triton	[48,73-75]

Table 3: Literature sources of the planetary data presented in Table 2.

Saturn's orbital period equals 29.45 Earth years, we averaged th above global temperature values to arrive at 93.7 ± 0.6 K as an estimate of Titan's 30-year GMAT. Similarly, data gathered in the late 1970s by the Viking Landers on Mars were combined with more recent Curiosity-Rover surface measurements and 1999-2005 remote observations by the Mars Global Surveyor (MGS) spacecraft to derive representative estimates of GMAT and atmospheric urface pressure for the Red Planet. Some parameter values reported in the literature did not meet our criteria for global representativeness nd/or physical plausibility and were recalculated using available bservations a described below.

The mean solar irradiances of all bodies were calculated as $S = S_E r_{au}^{-2}$ where r_{au} is the body's average distance (semi major axis) to the Sun (AU) and S_E = 1,360.9 W m^{-2} is the Earth's new lower irradiance at 1 AU according to recent satellite observations reported by Kopp and Lean [49]. Due to a design flaw in earlier spectrometers, the solar irradiance at Earth's distance has been overestimated by ≈ 5 W m^{-2} prior to 2003 [49]. Consequently, our calculations yielded slightly lower irradiances for bodies such as Venus and Mars compared to previously published data. Our decision to recalculate S was based on the assumption that the orbital distances of planets are known with much greater accuracy than TOA solar irradiances. Hence, a correction made to Earth's irradiance requires adjusting the 'solar constants' of all other planets as well.

We found that quoted values for the mean global temperature and surface atmospheric pressure of Mars were either improbable or too uncertain to be useful for our analysis. Thus, studies published in the last 15 years report Mars' GMAT being anywhere between 200 K and 240 K with the most frequently quoted values in the range 210–220 K [6,32,76-81]. However, in-situ measurements by Viking Lander 1 suggest that the average surface air temperature at a low-elevation site in the Martian subtropics does not exceed 207 K during the summer-fall season (Appendix B). Therefore, the Red Planet's GMAT must be lower than 207 K. The Viking records also indicate that average diurnal temperatures above 210 K can only occur on Mars during summertime. Hence, all such values must be significantly higher than the actual mean annual temperature at any Martian latitude. This is also supported by results from a 3-D global circulation model of the Red Planet obtained by Fenton et al. [82]. The surface atmospheric pressure on Mars varies appreciably with season and location. Its global average value has previously been reported between 600 Pa and 700 Pa [6,32,78,80,83,84], a range that was too broad for the target precision of our study. Hence our decision to calculate new annual global means of near-surface temperature and air pressure for Mars via a thorough analysis of available data from remote-sensing and *in-situ* observations. Appendix B details our computational procedure with the results presented in Table 2. It is noteworthy that our independent estimate of Mars' GMAT (190.56 ± 0.7 K), while significantly lower than values quoted in recent years, is in perfect agreement with spherically integrated brightness temperatures of the Red Planet derived from remote microwave measurements in the late 1960s and early 1970s [85-87].

Moon's GMAT was also not readily extractable from the published literature. Although lunar temperatures have been measured for more than 50 years both remotely and *in situ* [36] most studies focus on observed temperature extremes across the lunar surface [56] and rarely discuss the Moon's average global temperature. Current GMAT estimates for the Moon cluster around two narrow ranges: 250–255 K and 269–271 K [32]. A careful examination of the published data reveals that the 250–255 K range is based on subterranean heat-flow measurements conducted at depths between 80 and 140 cm at the Apollo 15 and 17 landing sites located at 26°N; 3.6°E and 20°N; 30.6°E, respectively [88]. Due to a strong temperature dependence of the lunar regolith thermal conductivity in the topmost 1-2 cm soil, the Moon's average diurnal temperature increases steadily with depth. According to Apollo measurements, the mean daily temperature at 35 cm belowground is 40–45 K higher than that at the lunar surface [88]. The diurnal temperature fluctuations completely vanish below a depth of 80 cm. At 100 cm depth, the temperature of the lunar regolith ranged from 250.7 K to 252.5 K at the Apollo 15 site and between 254.5 K and 255.5 K at the Apollo 17 site [88]. Hence, reported Moon average temperatures in the range 250-255 K do not describe surface conditions. Moreover, since measured in the lunar subtropics, such temperatures do not likely even represent Moon's global thermal environment at these depths. On the other hand, frequently quoted Moon global temperatures of ~270 K have actually been calculated from Eq. (3) and are not based on surface measurements. However, as demonstrated by Volokin and ReLlez [1],

Eq. (3) overestimates the mean global surface temperature of spheres by about 37%. In this study, we employed the spherical estimate of Moon's GMAT (197.35 K) obtained by Volokin and ReLlez [1] using output from a NASA thermo-physical model validated against Diviner observations [29].

Surprisingly, many publications report incorrect values even for Earth's mean global temperature. Studies of terrestrial climate typically focus on temperature anomalies and if Earth's GMAT is ever mentioned, it is often loosely quoted as 15 C (~288 K) [2-4,6]. However, observations archived in the HadCRUT4 dataset of the UK Met Office's Hadley Centre [50,89] and in the Global Historical Climatology Network [51,52,90,91] indicate that, between 1981 and 2010, Earth's mean annual surface air temperature was 287.4 K (14.3 C) ± 0.5 K. Some recent studies acknowledge this more accurate lower value of Earth's absolute global temperature [92]. For Earth's mean surface atmospheric pressure we adopted the estimate by Trenberth et al. [53] (98.55 kPa), which takes into account the average elevation of continental landmasses above sea level; hence, it is slightly lower than the typical sea-level pressure of ≈ 101.3 kPa.

The average near-surface atmospheric densities (ρ, kg m^{-3}) of planetary bodies were calculated from reported means of total atmospheric pressure (P), molar mass (M, kg mol^{-1}) and temperature (T_s) using the Ideal Gas Law, i.e.

$$\rho = \frac{P\,M}{R\,T_s} \tag{6}$$

where R = 8.31446 J mol^{-1} K^{-1} is the universal gas constant. This calculation was intended to make atmospheric densities physically consistent with independent data on pressure and temperature utilized in our study. The resulting ρ values were similar to previously published data for individual bodies. Standard errors of the air-density estimates were calculated from reported errors of P and T_s for each body using Eq. (6).

Data in Table 2 were harnessed to compute several intermediate variables and all dimensionless π_i products necessary for the regression analyses. The results from these computations are shown in Table 4. Greenhouse gases in planetary atmospheres represented by the major constituents carbon dioxide (CO_2), methane (CH_4) and water vapor (H_2O) were collectively quantified via three bulk parameters: average molar mass (M_{gh}, kg mol^{-1}), combined partial pressure (P_{gh}, Pa) and combined partial density (ρ_{gh}, kg m^{-3}). These parameters were estimated from reported volumetric concentrations of individual greenhouse gases (C_x, %) and data on total atmospheric pressure and density in Table 2 using the formulas:

$$M_{gh} = \left(0.044 C_{CO2} + 0.016 C_{CH4} + 0.018 C_{H2O}\right) / C_{gh} \tag{7}$$

$$P_{gh} = P\left(0.01 C_{gh}\right) \tag{8}$$

$$\rho_{gh} = \rho\left(0.01 C_{gh}\right)\left(M_{gh} / M\right) \tag{9}$$

where $C_{gh} = C_{CO2} + C_{CH4} + C_{H2O}$ is the total volumetric concentration of major greenhouse gases (%). The reference temperatures T_e and T_{na} were calculated from Equation (3) and (4c), respectively.

Results

Function (5) was fitted to each one of the 12 sets of logarithmic π_i pairs generated by Equations (1) and (2) and shown in Table 4. Figures 1 and 2 display the resulting curves of individual regression models with planetary data plotted in the background for reference. Table 5 lists the statistical scores of each non-linear regression. Model 12 depicted in Figure 2f had the highest R^2 = 0.9999 and the lowest standard error σ_t = 0.0078 among all regressions. Model 1 (Figure 1a) provided the second best fit with R^2 = 0.9844 and σ_{est} = 0.1529. Notably, Model 1 shows almost a 20-time larger standard error on the logarithmic scale than Model 12. Figure 3 illustrates the difference in predictive skills between the two top-performing Models 1 and 12 upon conversion of vertical axes to a linear scale. Taking an antilogarithm weakens the relationship of Model 1 to the point of becoming immaterial and highlights the superiority of Model 12. The statistical results shown in Table 5 indicate that the explanatory power and descriptive accuracy of Model 12 surpass those of all other models by a wide margin.

Since Titan and Earth nearly overlap on the logarithmic scale of Figure 2f, we decided to experiment with an alternative regression for Model 12,

Intermediate Variable or Dimensionless Product	Venus	Earth	Moon	Mars	Titan	Triton
Average molar mass of greenhouse gases, M_{gh} (kg mol^{-1}) (Eq. 7)	0.0440	0.0216	0.0	0.0440	0.0160	0.0160
Near-surface partial pressure of greenhouse gases, P_{gh} (Pa) (Eq. 8)	8,974,500.0 ± 96,500	283.8 ± 0.02	0.0	667.7 ± 13.8	7,188.3 ± 4.9	$9.6 \times 10^{-4} \pm 2.9 \times 10^{-4}$
Near-surface density of greenhouse gases ρ_{gh} (kg m^{-3}) (Eq. 9)	64.441 ± 0.429	$2.57 \times 10^{-3} \pm 4.3 \times 10^{-6}$	0.0	$0.018 \pm 3.1 \times 10^{-4}$	$0.148 \pm 8.4 \times 10^{-4}$	$4.74 \times 10^{-8} \pm 1.3 \times 10^{-8}$
Radiating equilibrium temperature, T_e (K) (Eq. 3)	185.0	256.4	269.7	211.9	83.6	39.2
Average airless spherical temperature, T_{na} (K) (Eq. 4c)	231.7	197.0	197 0	159.6	63.6	35.9
T_s / T_e	3.985 ± 0.016	1.121 ± 0.002	0.732 ± 0.003	0.899 ± 0.003	1.120 ± 0.008	0.994 ± 0 026
T_s / T_{na}	3.181 ± 0.013	1.459 ± 0.002	1.002 ± 0.004	1.194 ± 0.004	1.473 ± 0.011	1.086 ± 0 028
$\ln(T_s / T_e)$	1.3825 ± 0.0041	0.1141 ± 0.0017	-0.3123 ± 0.0046	-0.1063 ± 0.0037	0.1136 ± 0.0075	$-5.2 \times 10^{-3} \pm 0.0256$
$\ln(T_s / T_{na})$	1.1573 ± 0.0041	0.3775 ± 0.0017	$1.59 \times 10^{-3} \pm 0.0046$	0.1772 ± 0.0037	0.3870 ± 0.0075	0.0828 ± 0 0256
$\ln[P_{gh}^3 / (\rho_{gh} S^2)]$	28.1364	8.4784	Undefine	10.7520	23.1644	-4.7981
$\ln[P^3 / (\rho_{gh} S^2)]$	28 2433	26.0283	+∞	10.8304	32.2122	20.2065
$\ln[P_{gh}^3 / (\rho S^2)]$	28.1145	2.3370	Undefine	10.7396	19.6102	-13.6926
$\ln[P_{gh} / P_r]$	9.5936	-0.7679	Undefine	0.0876	2.4639	-13.3649
$\ln[P^3 / (\rho S^2)]$	28 2214	19.8869	-46.7497	10.8180	28.6580	11.3120
$\ln(PIP_r)$	9.6292 ± 0.0108	$5.0820 \pm 6.6 \times 10^{-5}$	-28.3570 ± 0.3516	0.1137 ± 0.0207	$5.4799 \pm 6.8 \times 10^{-4}$	-5.0300 ± 0.3095

Table 4: Intermediate variables and dimensionless products required for the regression analyses and calculated from data in Table 2. Equations used to compute intermediate variables are shown in parentheses. The reference pressure is set to the barometric triple point of water, i e. P_r = 611.73 Pa.

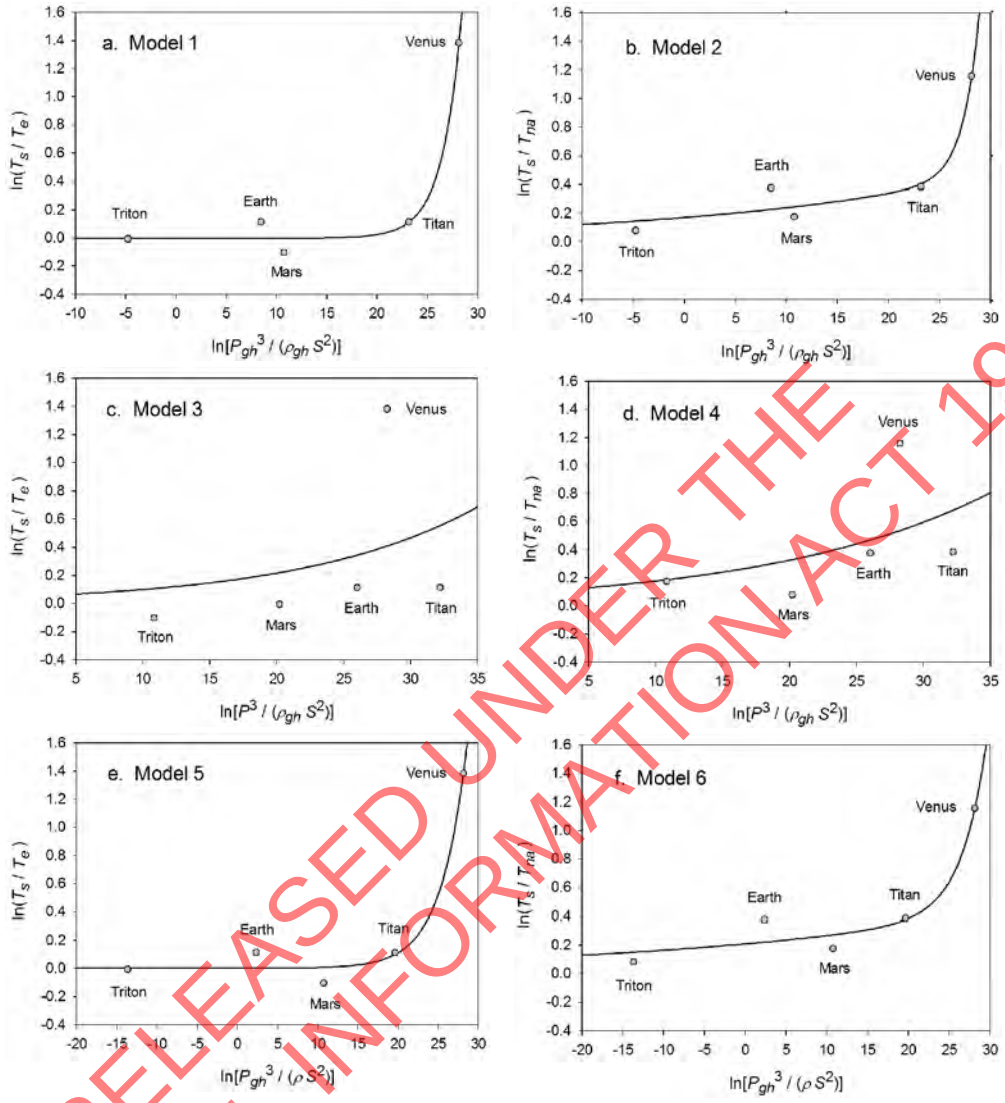

Figure 1: The rela ive atmospheric thermal enhancement (T_s/T_r) as a function of various dimensionless forcing variables generated by DA using data on solar irradiance, near-surface partial pressure/den ity of greenhouse gases, and total atmospheric pressure/density from Table 4. Panels *a* through *f* depict six regression models suggested by DA with the underlying celestial bodies plotted in the background for reference. Each pair of horizontal graphs represents different reference temperatures (T_r) defined as either $T_r = T_e$ (left) or $T_r = T_{na}$ (right).

which excludes Titan from the input dataset. This new curve had R^2 = 1.0 and σ_{est} = 0.0009. Although the two regression equations yield similar results over most of the relevant pressure range, we chose the one without Titan as final for Model 12 based on the assumption that Earth's GMAT is likely known with a much greater accuracy than Titan's mean annual temperature. Taking an antilogarithm of the final regression equation, which excludes Titan, yielded the following expression for Model 12:

$$\frac{T_s}{T_{na}} = \exp\left[0.174205\left(\frac{P}{P_r}\right)^{0.150263} + 1.83121 \times 10^{-5}\left(\frac{P}{P_r}\right)^{1.04193}\right] \quad (10a)$$

The regression coefficients in Eq. (10a) are intentionally shown in full precision to allow an accurate calculation of RATE (i.e. the T_s/T_{na} ratios) provided the strong non-linearity of the relationship and to facilitate a successful replication of our results by other researchers. Figure 4 depicts Eq. (10a) as a dependence of RATE on the average surface air pressure. Superimposed on this graph are the six planetary bodies from Table 4 along with their uncertainty ranges.

Equation (10a) implies that GMATs of rocky planets can be calculated as a product of two quantities: the planet's average surface temperature in the absence of an atmosphere (T_{na}, K) and a non-dimensional factor ($E_a \geq 1.0$) quantifying the relative thermal effect of the atmosphere, i.e.

$$T_s = T_{na}\, E_a \quad (10b)$$

where T_{na} is obtained from the SAT model (Eq. 4a) and E_a is a function of total pressure (P) given by:

$$E_a(P) = \exp\left[0.174205\left(\frac{P}{P_r}\right)^{0.150263}\right]\exp\left[1.83121\times10^{-5}\left(\frac{P}{P_r}\right)^{1.04193}\right] \quad (11)$$

Note that, as P approaches 0 in Eq. (11), E_a approaches the physically realistic limit of 1.0. Other physical aspects of this equation are discussed below.

For bodies with tangible atmospheres (such as Venus, Earth,

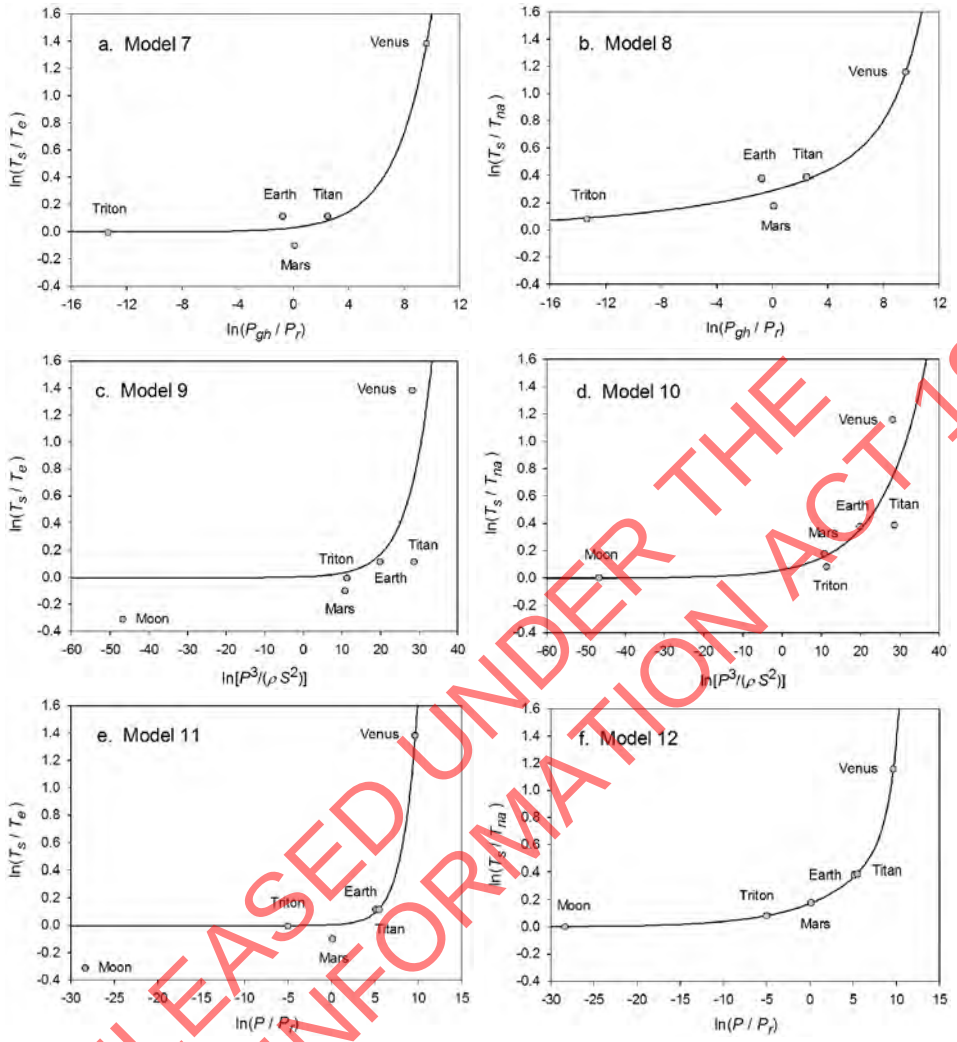

Figure 2: The same as in Figure 1 but for six additional regression models (panels *a* through *f*).

Mars, Titan and Triton), one must calculate T_{na} using α_e = 0.132 and η_e = 0.00971, which assumes a Moon-like airless reference surface in accordance with our pre-analysis premise. For bodies with tenuous atmospheres (such as Mercury, the Moon, Calisto and Europa), T_{na} should be calculated from Eq. (4a) (or Eq. 4b respectively if $S > 0.15$ W m^{-2} and/or Rg ≈ 0 W m^{-2}) using the body's observed values of Bond albedo α_e and ground heat storage fraction η_e. In the context of this model, a tangible atmosphere is defined as one that has significantly modified the optical and thermo-physical properties of a planet's surface compared to an airless environment and/or noticeably impacted the overall planetary albedo by enabling the formation of clouds and haze. A tenuous atmosphere, on the other hand, is one that has not had a measurable influence on the surface albedo and regolith thermo-physical properties and is completely transparent to shortwave radiation. The need for such delineation of atmospheric masses when calculating T_{na} arises from the fact that Eq. (10a) accurately describes RATEs of planetary bodies with tangible atmospheres over a wide range of conditions without explicitly accounting for the observed large differences in albedos (i.e. from 0.235 to 0.90) while assuming constant values of α_e and η_e for the airless equivalent of these bodies. One possible explanation for this counterintuitive empirical result is that atmospheric pressure alters the planetary albedo and heat storage properties of the surface in a way that transforms these parameters from independent controllers of the global temperature in airless bodies to intrinsic byproducts of the climate system itself in worlds with appreciable atmospheres. In other words, once atmospheric pressure rises above a certain level, the effects of albedo and ground heat storage on GMAT become implicitly accounted for by Eq. (11). Although this hypothesis requires a further investigation beyond the scope of the present study, one finds an initial support for it in the observation that, according to data in Table 2, GMATs of bodies with tangible atmospheres do not show a physically meaningful relationship with the amounts of absorbed shortwave radiation determined by albedos. Our discovery for the need to utilize different albedos and heat storage coefficients between airless worlds and worlds with tangible atmospheres is not unique as a methodological approach. In many areas of science and engineering, it is sometime necessary to use disparate model parameterizations to successfully describe different aspects of the same phenomenon. An example is the distinction made in fluid mechanics between laminar and turbulent flow, where the non-dimensional Reynold's number is employed to separate the two regimes that are subjected to different mathematical treatments.

No.	Functional Model	Coefficient of Determination (R^2)	Adjusted R^2	Standard Error σ_{est}
1	$\frac{T_s}{T_e} = f\left(\frac{P_{gh}^{\ 3}}{\rho_{gh} S^2}\right)$	0.9844	0.9375	0.1529
2	$\frac{T_s}{T_{na}} = f\left(\frac{P_{gh}^{\ 3}}{\rho_{gh} S^2}\right)$	0.9562	0.8249	0.1773
3	$\frac{T_s}{T_e} = f\left(\frac{P^3}{\rho_{gh} S^2}\right)$	0.1372	-2.4511	1.1360
4	$\frac{T_s}{T_{na}} = f\left(\frac{P^3}{\rho_{gh} S^2}\right)$	0.2450	-2.0200	0.7365
5	$\frac{T_s}{T_e} = f\left(\frac{P_{gh}^{\ 3}}{\rho S^2}\right)$	0.9835	0.9339	0.1572
6	$\frac{T_s}{T_{na}} = f\left(\frac{P_{gh}^{\ 3}}{\rho S^2}\right)$	0.9467	0.7866	0.1957
7	$\frac{T_s}{T_e} = f\left(\frac{P_{gh}}{P_r}\right)$	0.9818	0.927	0.1648
8	$\frac{T_s}{T_{na}} = f\left(\frac{P_{gh}}{P_r}\right)$	0.9649	0.8598	0.1587
9	$\frac{T_s}{T_e} = f\left(\frac{P^3}{\rho S^2}\right)$	0.4488	-0.3780	0.7060
10	$\frac{T_s}{T_{na}} = f\left(\frac{P^3}{\rho S^2}\right)$	0.6256	0.0639	0.4049
11	$\frac{T_s}{T_e} = f\left(\frac{P}{P_r}\right)$	0.9396	0.8489	0.2338
12	$\frac{T_s}{T_{na}} = f\left(\frac{P}{P_r}\right)$	0.9999	0.9997	0.0078

Table 5: Performance statistics of the twelve regression models suggested by DA. Statistical scores refer to the model logarithmic forms shown in Figures 1 and 2.

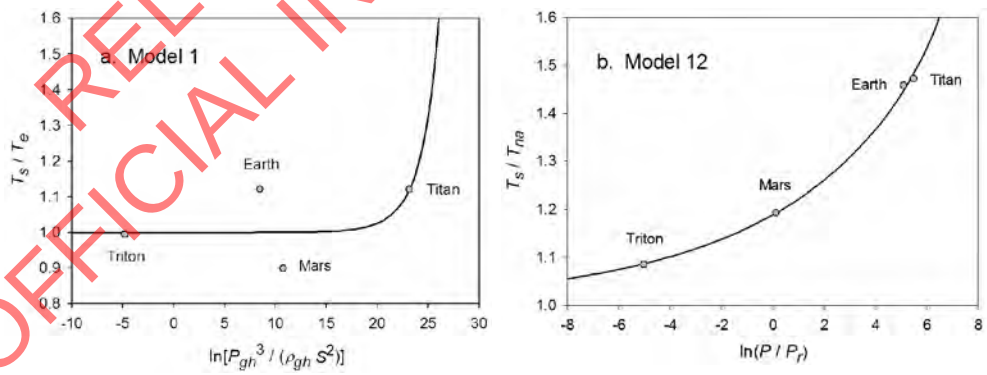

Figure 3: Comparison of the two best-performing regression models according to statistical scores listed in Table 5. Vertical axes use linear scales to better illustrate he difference in skills between the models.

We do not currently have sufficient data to precisely define the limit between *tangible* and *tenuous* atmospheres in terms of total pressure for the purpose of this model. However, considering that an atmospheric pressure of 1.0 Pa on Pluto causes the formation of layered haze [93], we surmise that this limit likely lies significantly below 1.0 Pa. In this study, we use 0.01 Pa as a tentative threshold value. Thus, in the context of Eq. (10b), we recommend computing T_{na} from Eq. (4c) if $P > 10^{-2}$ Pa, and from Eq. (4a) (or Eq. 4b, respectively) using observed values of α_e and η_e if $P \leq 10^{-2}$ Pa. Equation (4a) should also be employed in cases, where a significant geothermal flux exists such as on the Galilean moons of Jupiter due to tidal heating, and/or if $S \leq 0.15$ W m^{-2}. Hence, the 30-year mean global equilibrium surface temperature of rocky planets depends in general on five factors: TOA stellar irradiance (S), a reference airless surface albedo (α_e), a reference airless ground heat storage fraction

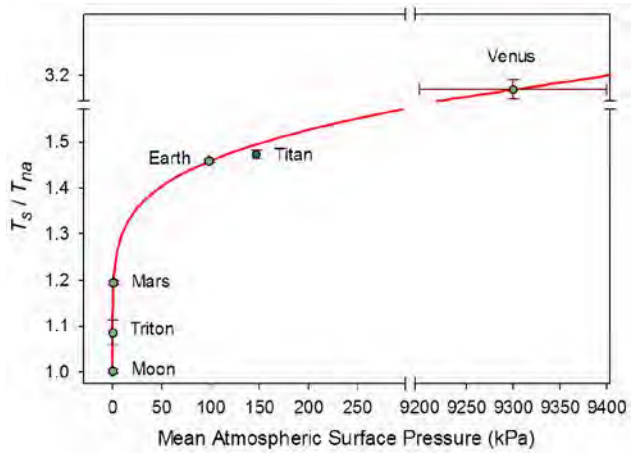

Figure 4: The relative atmospheric thermal enhancement (T_s/T_{na} ratio) as a function of the average surface air pressure according to Eq. (10a) derived from data representing a broad range of planetary environments in the solar system. Saturn's moon Titan has been excluded from the regression analysis leading to Eq. (10a). Error bars of some bodies are not clearly visible due to their small size relative to the scale of the axes. See Table 2 for the actual error estimates.

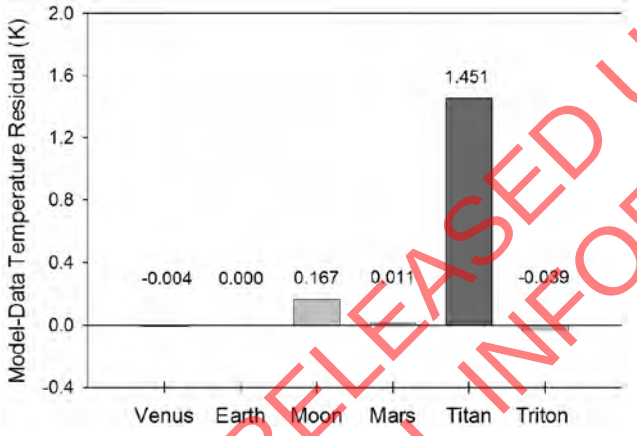

Figure 5: Absolute differences between modeled average global temperatures by Eq. (10b) and observed GMATs (Table 2) for the studied celestial bodies. Saturn's moon Titan represents an independent data point, since it was excluded from the regression analysis leading to Eq. (10a).

(η_e), the average geothermal flux reaching the surface (R_g), and the total surface atmospheric pressure (P). For planets with tangible atmospheres ($P > 10^{-2}$ Pa) and a negligible geothermal heating of the surface ($R_g \approx 0$), the equilibrium GMAT becomes only a function of two factors: S and P, i.e. $T_s = 32.44\ S^{0.25} E_a(P)$. The final model (Eq. 10b) can also be cast in terms of T_s as a function of a planet's distance to the Sun (r_{au}, AU) by replacing S in Equations (4a), (4b) or (4c) with $1360.9\ r_{au}^{-2}$.

Environmental scope and numerical accuracy of the new model

Figure 5 portrays the residuals between modeled and observed absolute planetary temperatures. For celestial bodies participating in the regression analysis (i.e. Venus, Earth, Moon, Mars and Triton), the maximum model error does not exceed 0.17 K and is well within the uncertainty of observations. The error for Titan, an independent data point, is 1.45 K or 1.5% of that moon's current best-known GMAT (93.7 K). Equation (10b) produces 95.18 K for Titan at Saturn's semi-major axis (9.582 AU) corresponding to a solar irradiance $S = 14.8$ W m^{-2}. This estimate is virtually identical to the 95 K average surface temperature reported for that moon by the NASA JPL Voyager Mission website [94]. The Voyager spacecraft 1 and 2 reached Saturn and its moons in November 1980 and August 1981, respectively, when the gas giant was at a distance between 9.52 AU and 9.60 AU from the Sun corresponding approximately to Saturn's semi-major axis [95].

Data acquired by Voyager 1 suggested an average surface temperature of 94 ± 0.7 K for Titan, while Voyager 2 indicated a temperature close to 95 K [41]. Measurements obtained between 2005 and 2010 by the Cassini-Huygens mission revealed $T_s \approx 93.4 \pm 0.6$ K [42,43]. Using Saturn's perihelion (9.023 AU) and aphelion (10.05 AU) one can compute Titan's TOA solar irradiance at the closest and furthest approach to the Sun, i.e 16.7 W m^{-2} and 13.47 W m^{-2}, respectively. Inserting these values into Eq. (10b) produces the expected upper and lower limit of Titan's mean global surface temperature according to our model, i.e. $92.9\ \text{K} \le T_s \le 98.1$ K. Notably this range encompasses all current observation-based estimates of Titan's GMAT. Since both Voyager and Cassini mission covered shorter periods than a single Titan season (Saturn's orbital period is 29.45 Earth years), the available measurements may not well represent that moon's annual thermal cycle. In addition, due to a thermal inertia, Titan's average surface temperature likely lags variations in the TOA solar irradiance caused by Saturn's orbital eccentricity. Thus, the observed 1.45 K discrepancy between our independent model prediction and Titan's current best-known GMAT seems to be within the range of plausible global temperature fluctuations on that moon. Hence, further observations are needed to more precisely constrain Titan's long-term GMAT.

Measurements conducted by the Voyager spacecraft in 1989 indicated a global mean temperature of 38 ± 1.0 K and an average atmospheric pressure of 1.4 Pa at the surface of Triton [73]. Even though Eq. (10a) is based on slightly different data for Triton (i.e. T_s = 39 ±1.0 K and P = 4.0 Pa) obtained by more recent stellar occultation measurements [73], employing the Voyager-reported pressure in Eq. (10b) produces T_s = 38.5 K for Triton's GMAT, a value well within the uncertainty of the 1989 temperature measurements.

The above comparisons indicate that Eq. (10b) rather accurately describes the observed variation of the mean surface temperature across a wide range of planetary environments in terms of solar irradiance (from 1.5 W m^{-2} to 2,602 W m^{-2}), total atmospheric pressure (from near vacuum to 9,300 kPa) and greenhouse-gas concentrations (from 0.0% to over 96% per volume). While true that Eq. (10a) is based on data from only 6 celestial objects, one should keep in mind that these constitute virtually all bodies in the Solar System meeting our criteria for availability and quality of measured data. Although function (5) has 4 free parameters estimated from just 5-6 data points, there are no signs of model overfitting in this case because (*a*) Eq. (5) represents a monotonic function of a rigid shape that can only describe well certain exponential pattern as evident from Figures 1 and 2 and the statistical scores in Table 5; (*b*) a simple scatter plot of $\ln(P/P_r)$ vs. $\ln(T_s/T_{na})$ visibly reveals the presence of an exponential relationship free of data noise; and (*c*) no polynomial can fit the data points in Figure 2f as accurately as Eq. (5) while also producing a physically meaningful response curve similar to known pressure-temperature relationships in other systems. These facts indicate that Eq. (5) is not too complicated to cause an over-fitting but just right for describing the data at hand.

The fact that only one of the investigated twelve non-linear regressions yielded a tight relationship suggests that Model 12 describes

a macro-level thermodynamic property of planetary atmospheres heretofore unbeknown to science. A function of such predictive power spanning the entire breadth of the Solar System cannot be just a result of chance. Indeed, complex natural systems consisting of myriad interacting agents have been known to sometime exhibit emergent responses at higher levels of hierarchical organization that are amenable to accurate modeling using top-down statistical approaches [96]. Equation (10a) also displays several other characteristics discussed below that lend further support to the above notion.

Model robustness

Model robustness defines the degree to which a statistical relationship would hold when recalculated using a different dataset. To test the robustness of Eq. (10a) we performed an alternative regression analysis, which excluded Earth and Titan from the input data and only utilized logarithmic pairs of T_s/T_{na} and P/P_r for Venus, the Moon, Mars and Triton from Table 4. The goal was to evaluate how well the resulting new regression equation would predict the observed mean surface temperatures of Earth and Titan. Since these two bodies occupy a highly non-linear region in Model 12 (Figure 2f), eliminating them from the regression analysis would leave a key portion of the curve poorly defined. As in all previous cases, function (5) was fitted to the incomplete dataset (omitting Earth and Titan), which yielded the following expression:

$$\frac{T_s}{T_{na}} = \exp\left[0.174222\left(\frac{P}{P_r}\right)^{0.150275} + 5.25043\times10^{-15}\left(\frac{P}{P_r}\right)^{3.32375}\right] \quad (12a)$$

Substituting the reference temperature T_{na} in Eq. (12a) with its equivalent from Eq. (4c) and solving for T_s produces

$$T_s = 32.44 S^{0.25} \exp\left[0.174222\left(\frac{P}{P_r}\right)^{0.150275}\right]\exp\left[5.25043\times10^{-15}\left(\frac{P}{P_r}\right)^{3.32375}\right] \quad (12b)$$

It is evident that the regression coefficients in the first exponent term of Eq. (12a) are nearly identical to those in Eq. (10a). This term dominates the T_s-P relationship over the pressure range 0-400 kPa accounting for more than 97.5% of the predicted temperature magnitudes. The regression coefficients of the second exponent differ somewhat between the two formulas causing a divergence of calculated RATE values over the pressure interval 400–9,100 kPa. The models converge again between 9,000 kPa and 9,300 kPa. Figure 6 illustrates the similarity of responses between Equations (10a) and (12a) over the pressure range 0–300 kPa with Earth and Titan plotted in the foreground for reference.

Equation (12b) reproduces the observed global surface temperature of Earth with an error of 0.4% (-1.0 K) and that of Titan with an error of 1.0% (+0.9 K). For Titan, the error of the new Eq. (12b) is even slightly smaller than that of the original model (Eq. 10b). The ability of Model 12 to predict Earth's GMAT with an accuracy of 99.6% using a relationship inferred from disparate environments such as those found on Venus, Moon, Mars and Triton indicates that (*a*) this model is statistically robust, and (*b*) Earth's temperature is a part of a cosmic thermodynamic continuum well described by Eq. (10b). The apparent smoothness of this continuum for bodies with tangible atmospheres (illustrated in Figure 4) suggests that planetary climates are well-buffered and have no 'tipping points' in reality, i.e. states enabling rapid and irreversible changes in the global equilibrium temperature as a result of destabilizing positive feedbacks assumed to operate within climate systems. This robustness test also serves as a cross-validation suggesting that the new model has a universal nature and it is not a product of overfitting.

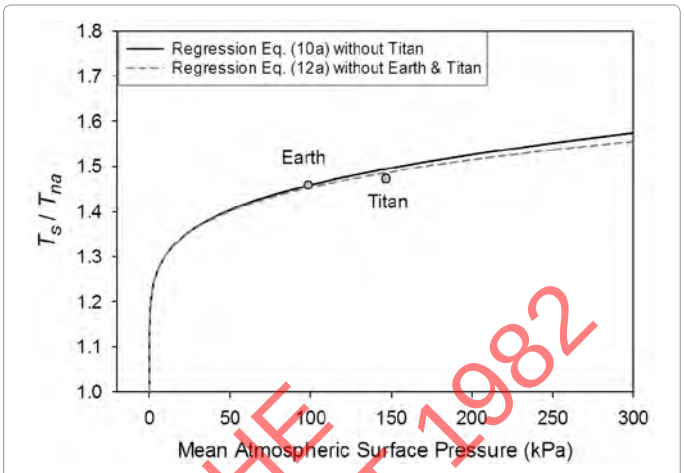

Figure 6: Demonstration of the robustness of Model 12. The solid black curve depicts Eq. (10a) based on data from 5 celestial bodies (i.e. Venus, Earth, Moon, Mars and Triton). The dashed grey curve portrays Eq. (12a) derived from data of only 4 bodies (i.e. Venus, Moon, Mars and Triton) while excluding Earth and Titan from the regression analysis. The alternative Eq. (12b) predicts the observed GMATs of Earth and Titan with accuracy greater than 99% indicating that Model 12 is statistically robust.

The above characteristics of Eq. (10a) including dimensional homogeneity, high predictive accuracy, broad environmental scope of validity and statistical robustness indicate that it represents an emergent macro-physical model of theoretical significance deserving further investigation. This conclusive result is also supported by the physical meaningfulness of the response curve described by Eq. (10a).

Discussion

Given the high statistical scores of the new model discussed above, it is important to address its physical significance, potential limitations, and broad implications for the current climate theory.

Similarity of the new model to Poisson's formula and the SB radiation law

The functional response of Eq. (10a) portrayed in Figure 4 closely resembles the shape of the dry adiabatic temperature curve in Figure 7a described by the Poisson formula and derived from the First Law of Thermodynamics and the Ideal Gas Law [4], i.e.

$$\frac{T}{T_o} = \left(\frac{p}{p_o}\right)^{R/c_p} \quad (13)$$

Here, T_o and p_o are reference values for temperature and pressure typically measured at the surface, while T and p are corresponding scalars in the free atmosphere, and c_p is the molar heat capacity of air (J mol^{-1} K^{-1}). For the Earth's atmosphere, $R/c_p = 0.286$. Equation (13) essentially describes the direct effect of pressure p on the gas temperature (T) in the absence of any heat exchange with the surrounding environment.

Equation (10a) is structurally similar to Eq. (13) in a sense that both expressions relate a temperature ratio to a pressure ratio, or more precisely, a relative thermal enhancement to a ratio of physical forces. However, while the Poisson formula typically produces $0 \le T/T_o \le 1.0$, Eq. (10a) always yields $T_s/T_{na} \ge 1.0$. The key difference between the two models stems from the fact that Eq. (13) describes vertical temperature changes in a free and dry atmosphere induced by a gravity-controlled pressure gradient, while Eq. (10a) predicts the equilibrium response of a planet's global surface air temperature to variations in total atmospheric

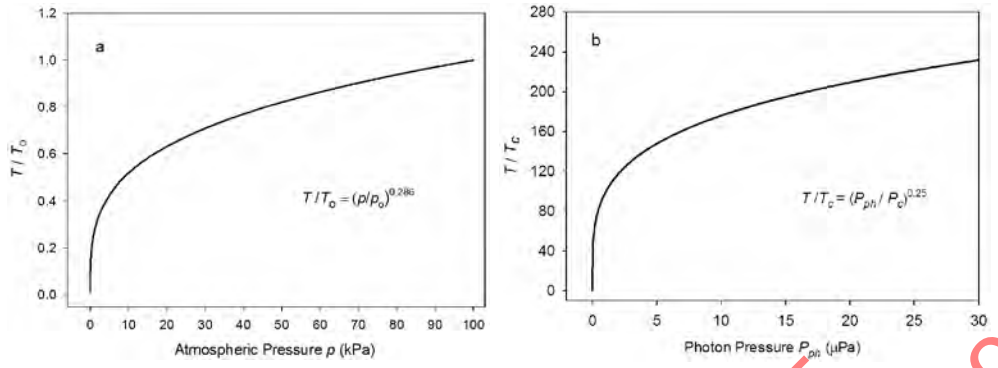

Figure 7: Known pressure-temperature kinetic relations: (*a*) Dry adiabatic response of the air/surface temperature ratio to pressure changes in a free dry atmosphere according to Poisson's formula (Eq. 13) with a reference pressure set to p_o = 100 kPa; (*b*) The SB radiation law expressed as a response of a blackbody temperature ratio to variations in photon pressure (Eq. 14). Note he qualitative striking similarity of shapes between these curves and the one portrayed in Figure 4 depicting the new planetary temperature model (Eq. 10a).

pressure. In essence, Eq. (10b) could be viewed as a predictor of the reference temperature T_o in the Poisson formula. Thus, while qualitatively similar, Equations (10a) and (13) are quantitatively rather different. Both functions describe effects of pressure on temperature but in the context of disparate physical systems. Therefore, estimates obtained from Eq. (10a) should not be confused with results inferred from the Poisson formula. For example, Eq. (10b) cannot be expected to predict the temperature lapse rate and/or vertical temperature profiles within a planetary atmosphere as could be using Eq. (13). Furthermore, Eq. (10a) represents a top-down empirical model that implicitly accounts for a plethora of thermodynamic and radiative processes and feedbacks operating in real climate systems, while the Poisson formula (derived from the Ideal Gas Law) only describes pressure-induced temperature changes in a simple mixture of dry gases without any implicit or explicit consideration of planetary-scale mechanisms such as latent heat transport and cloud radiative forcing.

Equation (10a) also shows a remarkable similarity o the SB law relating the equilibrium skin temp rature f an isotherma blackbody (T_b, K) to the electromagnetic radiati e flux (I, W m^{-2}) absorbed/emitted by the body's surface, i $T = (I/\sigma)^{0.25}$. Dividing each side of this fundamental relationship by the irreducible temperature of deep Space T_c = 2.725 K and its causative CMBR R_c = 3.13 × 10^{-6} W m^{-2} respectively, yields $T_b/T_c = (I/R_c)^{0.25}$. Further, expressing the radiative fluxes I and R_c on the right-hand side as products of photon pressure and the speed of light (c, m s^{-1}) in a vacuum, i.e. $I = cP_{ph}$ and $R_c = cP_c$, leads to the following alternative f rm of the SB law:

$$\frac{T_b}{T_c} = \left(\frac{P_{ph}}{P_c}\right)^{0.25} \quad (14)$$

where P_c = 1.043 × 10^{-14} Pa is the photon pressure of CMBR. Clearly, Eq. (10a) is analogous to Eq. (14), while the latter is structurally identical to the Poisson formula (13). Figure 7b depicts Eq. (14) as a dependence of the T_b/T_c ratio on photon pressure P_{ph}.

It is evident from Figures 4 and 7 that formulas (10a), (13) and (14) describe qualitatively very similar responses in quantitatively vastly different systems. The presence of such similar relations in otherwise disparate physical systems can fundamentally be explained by the fact that pressure as a force per unit area represents a key component of the internal kinetic energy (defined as a product of gas volume and pressure), while temperature is merely a physical manifestation of this energy. Adding a force such as gas pressure to a physical system inevitably boosts the int rnal kinetic energy and raises its temperature, a process known in thermodynamics as compression heating. The direct effect of pressure on a system's temperature is thermodynamically described by adi batic proce ses. The pressure-induced thermal enhancement at a planetary lev l portrayed in Figure 4 and accurately quantified by Eq (10a or 11) is analogous to a compression heating, but not fully i entical to an adiabatic process. The latter is usually characterized by a limited duration and oftentimes only applies to finite-size parcels of air moving vertically through the atmosphere. Equation (11), on the other hand, describes a surface thermal effect that is global in scope and permanent in nature as long as an atmospheric mass is present within the planet's gravitational field. Hence, the planetary RATE (T_s/T_{na} ratio) c uld be understood as a net result of countless simultaneous adiabatic processes continuously operating in the free atmosphere. Figures 4 and 7 also suggest that the pressure control of temperature is a universal thermodynamic principle applicable to systems ranging in complexity from a simple isothermal blackbody absorbing a homogeneous flux of electromagnetic radiation to diverse planetary atmospheres governed by complex non-linear process interactions and cloud-radiative feedbacks. To our knowledge, this cross-scale similarity among various pressure-temperature relationships has not previously been identified and could provide a valuable new perspective on the working of planetary climates.

Nevertheless, important differences exist between Eq. (10a) and these other simpler pressure-temperature relations. Thus, while the Poisson formula and the SB radiation law can mathematically be derived from 'first principles' and experimentally tested in a laboratory, Eq. (10a) could neither be analytically deduced from known physical laws nor accurately simulated in a small-scale experiment. This is because Eq. (10a) describes an emergent macro-level property of planetary atmospheres representing the net result of myriad process interactions within real climate systems that are not readily computable using mechanistic (bottom-up) approaches adopted in climate models or fully reproducible in a laboratory setting.

Potential limitations of the planetary temperature model

Equation (10b) describes long-term (30-year) equilibrium GMATs of planetary bodies and does not predict inter-annual global temperature variations caused by intrinsic fluctuations of cloud albedo and/or ocean heat uptake. Thus, the observed 0.82 K rise of Earth's global temperature since 1880 is not captured by our model, as this warming was likely

not the result of an increased atmospheric pressure. Recent analyses of observed dimming and brightening periods worldwide [97-99] suggest that the warming over the past 130 years might have been caused by a decrease in global cloud cover and a subsequent increased absorption of solar radiation by the surface. Similarly, the mega shift of Earth's climate from a 'hothouse' to an 'icehouse' evident in the sedimentary archives over the past 51 My cannot be explained by Eq. (10b) unless caused by a large loss of atmospheric mass and a corresponding significant drop in surface air pressure since the early Eocene. Pleistocene fluctuations of global temperature in the order of 3.0–8.0 K during the last 2 My revealed by multiple proxies [100] are also not predictable by Eq. (10b) if due to factors other than changes in total atmospheric pressure and/or TOA solar irradiance.

The current prevailing view mostly based on theoretical considerations and results from climate models is that the Pleistocene glacial-interglacial cycles have been caused by a combination of three forcing agents: Milankovitch orbital variations, changes in atmospheric concentrations of greenhouse gases, and a hypothesized positive ice-albedo feedback [101,102]. However, recent studies have shown that orbital forcing and the ice-albedo feedback cannot explain key features of the glacial-interglacial oscillations such as the observed magnitudes of global temperature changes, the skewness of temperature response (i.e. slow glaciations followed by rapid meltdowns), and the mid-Pleistocene transition from a 41 Ky to 100 Ky cycle length [103-105]. The only significant forcing remaining in the present paleo-climatological toolbox to explicate the Pleistocene cycles are variations in greenhouse-gas concentrations. Hence, it is difficult to explain, from a standpoint of the current climate theory, the high accuracy of Eq. (11) describing the relative thermal effect of diverse planetary atmospheres without any consideration of greenhouse gases. If presumed forcing agents such as greenhouse-gas concentrations and the planetary albedo were ind ed responsible for the observed past temperature dynamics on Earth, why did these agents not show up as predictors of contemporary planetary temperatures in our analysis as well? Could it be because the e agents have not really been driving Earth's climate on geological time scales? We address the potential role of greenhouse gases in more d tails below. Since the relationship portrayed in Figure 4 is undoubtedly real, our model results point toward the need to reexamine some fundamental climate processes thought to be well understood for decades. For example, we are currently testing a hypo hesi that Pleistocene glacial cycles might have been caused by variations in Earth's total atmospheric mass and surface air pressure. Preliminary results based on the ability of an extended version of our planetary model (simulating meridional temperature gradients) to predict the observed polar amplification during the Last Glacial Maximum indicate that such a hypothesis is not unreasonable. However conclusive findings from this research will be discussed elsewhere.

According to the present understanding, Earth's atmospheric pressure has remained nearly invariant during the Cenozoic era (last 65.5 My). However, this notion is primarily based on theoretical analyses [106], since there are currently no known geo-chemical proxies permitting a reliable reconstruction of past pressure changes in a manner similar to that provided by various temperature proxies such as isotopic oxygen 18, alkenones and TEX_{86} in sediments, and Ar-N isotope ratios and deuterium concentrations in ice. The lack of independent pressure proxies makes the assumption of a constant atmospheric mass throughout the Cenozoic *a priori* and thus questionable. Although this topic is beyond the scope of our present study, allowing for the possibility that atmospheric pressure on Earth might have varied significantly over the past 65.5 My could open exciting new research venues in Earth sciences in general and paleoclimatology in particular.

Role of greenhouse gasses from a perspective of the new model

Our analysis revealed a poor relationship between GMAT and the amount of greenhouse gases in planetary atmospheres across a broad range of environments in the Solar System (Figures 1-3 and Table 5). This is a surprising result from the standpoint of the current Greenhouse theory, which assumes that an atmosphere warms the surface of a planet (or moon) via trapping of radiant heat by certain gases controlling the atmospheric infrared optical depth [4,9,10]. The atmospheric opacity to LW radiation depends on air density and gas absorptivity, which in turn are functions of total pressure, temperature and greenhouse-gas concentrations [9]. Pressure also controls the broadening of infrared absorption lines in individual gases. Therefore, the higher the pressure, the larger the infrared optical depth of an atmosphere, and the stronger the expected greenhouse effect would be. According to the current climate theory, pressure only indirectly affects global surface temperature through the atmospheric infrared opacity and its presumed constraint on the planet's LW emission to Space [9,107].

There are four plausible explanations for the apparent lack of a close relationship between GMAT and atmospheric greenhouse gasses in ur results: 1) The amounts of greenhouse gases considered in our analysis only refer to near-surface atmospheric compositions and do not de cribe the infrared optical depth of the entire atmospheric column; 2) The analysis lumped all greenhouse gases together and did not take into account differences in the infrared spectral absorptivity of individual gasses; 3) The effect of atmospheric pressure on broadening the infrared gas absorption lines might be stronger in reality than simulated by current radiative-transfer models, so that total pressure overrides the effect of a varying atmospheric composition across a wide range of planetary environments; and 4) Pressure as a force per unit area directly impacts the internal kinetic energy and temperature of a system in accordance with thermodynamic principles inferred from the Gas Law; hence, air pressure might be the actual physical causative factor controlling a planet's surface temperature rather than the atmospheric infrared optical depth, which merely correlates with temperature due to its co-dependence on pressure.

Based on evidence discussed earlier, we argue that option #4 is the most likely reason for the poor predictive skill of greenhouse gases with respect to planetary GMATs revealed in our study (Figures 1-3). By definition, the infrared optical depth of an atmosphere is a dimensionless quantity that carries no units of force or energy [3,4,9]. Therefore, it is difficult to fathom from a fundamental physics standpoint of view, how this non-dimensional parameter could increase the kinetic energy (and temperature) of the lower troposphere in the presence of free convection provided that the latter dominates the heat transport in gaseous systems. Pressure, on the other hand, has a dimension of force per unit area and as such is intimately related to the internal kinetic energy of an atmosphere E (J) defined as the product of gas pressure (P, Pa) and gas volume (V, m^3), i.e. E (J) = PV. Hence, the direct effect of pressure on a system's internal energy and temperature follows straight from fundamental parameter definitions in classical thermodynamics. Generally speaking, kinetic energy cannot exist without a pressure force. Even electromagnetic radiation has pressure.

In climate models, the effect of infrared optical depth on surface temperature is simulated by mathematically decoupling radiative transfer from convective heat exchange. Specifically, the LW

radiative transfer is calculated in these models without simultaneous consideration of sensible- and latent heat fluxes in the solution matrix. Radiative transfer modules compute the so-called heating rates (K/day) strictly as a function of atmospheric infrared opacity, which under constant-pressure conditions solely depends on greenhouse-gas concentrations. These heating rates are subsequently added to the thermodynamic portion of climate models and distributed throughout the atmosphere. In this manner, the surface warming becomes a function of an increasing atmospheric infrared opacity. This approach to modeling of radiative-convective energy transport rests on the principle of superposition, which is only applicable to linear systems, where the overall solution can be obtained as a sum of the solutions to individual system components. However, the integral heat transport within a free atmosphere is inherently nonlinear with respect to temperature. This is because, in the energy balance equation, radiant heat transfer is contingent upon power gradients of absolute temperatures, while convective cooling/heating depends on linear temperature differences in the case of sensible heat flux and on simple vapor pressure gradients in the case of latent heat flux [4]. The latent heat transport is in turn a function of a solvent's saturation vapor pressure, which increases exponentially with temperature [3]. Thus, the superposition principle cannot be employed in energy budget calculations. The artificial decoupling between radiative and convective heat-transfer processes adopted in climate models leads to mathematically and physically incorrect solutions with respect to surface temperature. The LW radiative transfer in a real climate system is intimately intertwined with turbulent convection/advection as both transport mechanisms occur simultaneously. Since convection (and especially the moist one) is orders of magnitude more efficient in transferring energy than LW radiation [3,4], and because heat preferentially travels along the path of least resistance, a properly coupled radiative-convective algorithm of energy exchange will produce quantitatively and qualitatively different temperature solutions in response to a changing atmospheric composition than the ones obtained by current climate models. Specifically, a correctly coupled convective-radiative system will render the surface temperature insensitive to variations in the atmospheric infrared optical depth, a result indirectly supported by our analysis as well. This topic requires further investigation beyond the scope of the present study.

The direct effect of atmospheric pressure on the global surface temperature has received virtually no attention in climate science thus far. However, the results from our empirical data analysis suggest that it deserves a serious consideration in the future.

Theoretical implications of the new interplanetary relationship

The hereto discovered pressure-temperature relationship quantified by Eq. (10a) and depicted in Figure 4 has broad theoretical implications that can be summarized as follows:

Physical nature of the atmospheric 'greenhouse effect': According to Eq. (10b), the heating mechanism of planetary atmospheres is analogous to a gravity-controlled adiabatic compression acting upon the entire surface. This means that the atmosphere does not function as an insulator reducing the rate of planet's infrared cooling to space as presently assumed [9,10], but instead adiabatically boosts the kinetic energy of the lower troposphere beyond the level of solar input through gas compression. Hence, the physical nature of the atmospheric 'greenhouse effect' is a pressure-induced thermal enhancement (PTE) independent of atmospheric composition. This mechanism is fundamentally different from the hypothesized 'trapping' of LW radiation by atmospheric trace gases first proposed in the 19th century and presently forming the core of the Greenhouse climate theory. However, a radiant-heat trapping by freely convective gases has never been demonstrated experimentally. We should point out that the hereto deduced adiabatic (pressure-controlled) nature of the atmospheric thermal effect rests on an objective analysis of vetted planetary observations from across the Solar System and is backed by proven thermodynamic principles, while the 'trapping' of LW radiation by an unconstrained atmosphere surmised by Fourier, Tyndall and Arrhenius in the 1800s was based on a theoretical conjecture. The latter has later been coded into algorithms that describe the surface temperature as a function of atmospheric infrared optical depth (instead of pressure) by artificially decoupling radiative transfer from convective heat exchange. Note also that the Ideal Gas Law ($PV = nRT$) forming the basis of atmospheric physics is indifferent to the gas chemical composition.

Effect of pressure on temperature: Atmospheric pressure provides in and of itself only a relative thermal enhancement (RATE) to the surface quantified by Eq. (11). The absolute thermal effect of an atmosphere depends on both pressure and the TOA solar irradiance. For example, at a total air pressure of 98.55 kPa, Earth's RATE is 1.459, which keeps our planet 90.4 K warmer in its present orbit than it would be in the absence of an atmosphere. Hence, our model fully explains the new ~90 K estimate of Earth's atmospheric thermal effect derived by Volokin and ReLlez [1] using a different line of reasoning. If one moves Earth to the orbit of Titan (located at ~9.6 AU from the Sun) without changing the overall pressure, our planet's RATE will remain the same, but the absolute thermal effect of the atmosphere would drop to about 29.2 K due to a vastly reduced solar flux. In other words, the absolute effect of pressure on a system's temperature depends on the background energy level of the environment. This implies that the absolute temperature of a gas may not follow variations of pressure if the gas energy absorption changes in opposite direction to that of pressure. For instance, the temperature of Earth's stratosphere increases with altitude above the tropopause despite a falling air pressure, because the absorption of UV radiation by ozone steeply increases with height, thus offsetting the effect of a dropping pressure. If the UV absorption were constant throughout the stratosphere, the air temperature would decrease with altitude.

Atmospheric back radiation and surface temperature: Since (according to Eq. 10b) the equilibrium GMAT of a planet is mainly determined by the TOA solar irradiance and surface atmospheric pressure, the down-welling LW radiation appears to be globally a product of the air temperature rather than a driver of the surface warming. In other words, on a planetary scale, the so-called back radiation is a consequence of the atmospheric thermal effect rather than a cause for it. This explains the broad variation in the size of the observed down-welling LW flux among celestial bodies irrespective of the amount of absorbed solar radiation. Therefore, a change in this thermal flux brought about by a shift in atmospheric LW emissivity cannot be expected to impact the global surface temperature. Any variation in the global infrared back radiation caused by a change in atmospheric composition would be compensated for by a corresponding shift in the intensity of the vertical convective heat transport. Such a balance between changes in atmospheric infrared heating and the upward convective cooling at the surface is required by the First Law of Thermodynamics. However, current climate models do not simulate this compensatory effect of sensible and latent heat fluxes due to an improper decoupling between radiative transfer and turbulent convection in the computation of total energy exchange.

Role of planetary albedos: The fact that Eq. (10b) accurately describes planetary GMATs without explicitly accounting for the observed broad range of albedos, i.e. from 0.136 to 0.9 (Table 2), indicates that the shortwave reflectivity of planetary atmospheres is mostly an intrinsic property (a byproduct) of the climate system itself rather than an independent driver of climate as currently believed. In other words, it is the internal energy of the atmosphere maintained by solar irradiance and air pressure that controls the bulk of the albedo. An indirect support for this unorthodox conclusion is provided by the observation that the amounts of absorbed shortwave radiation determined by albedos show no physically meaningful relationship with planetary GMATs. For example, data in Table 2 indicate that Venus absorbs 3.7 times less solar energy per unit area than Earth, yet its surface is about 450 K hotter than that of Earth; the Moon receives on average 54 W m^{-2} more net solar radiation than Earth, but it is about 90 K cooler on average than our planet. The hereto proposed passive nature of planetary albedos does not imply that the global cloud cover could not be influenced by an external forcing such as solar wind, galactic cosmic rays, and/or gravitational fields of other celestial objects. Empirical evidence strongly suggests that it can [108-113], but the magnitude of such influences is expected to be small compared to the total albedo due to the presence of stabilizing negative feedbacks within the system. We also anticipate that the sensitivity of GMATs to an albedo change will greatly vary among planetary bodies. Viewing the atmospheric reflectivity as a byproduct of the available internal energy rather than a driver of climate can also help explain the observed remarkable stability of Earth's albedo [54,114].

Climate stability: Our semi-empirical model (Equations 4a, 10b and 11) suggests that, as long as the mean annual TOA solar flux and the total atmospheric mass of a planet are stationary, the equilibrium GMAT will remain stable. Inter-annual and decadal variations of global temperature forced by fluctuations of cloud cover, for example, are expected to be small compared to the magnitude of the background atmospheric warming because of strong negative feedbacks limiting the albedo changes. This implies a relatively stable climate for a planet such as Earth absent significant shifts in the total atmospheric mass and the planet's orbital distance to the Sun. Hence, planetary climates appear to be free of tipping points, i.e. functional states fostering rapid and irreversible changes in the global temperature as a result of hypothesized positive feedbacks thought to operate within the system. In other words, our results suggest that the Earth's climate is well buffered against sudden changes.

Effect of oceans and water vapor on global temperature: The new model shows that the Earth's global equilibrium temperature is a part of a cosmic thermodynamic continuum controlled by atmospheric pressure and total solar irradiance. Since our planet is the only one among studied celestial bodies harboring a large quantity of liquid water on the surface, Eq. (10b) implies that the oceans play virtually no role in determining Earth's GMAT. This finding may sound inexplicable from the standpoint of the radiative Greenhouse theory, but it follows logically from the new paradigm of a pressure-induced atmospheric warming. The presence of liquid water on the surface of a planet requires an air pressure greater than 612 Pa and an ambient temperature above 273.2 K. These conditions are provided by the planet's size and gravity, its distance to the Sun, and the mass of the atmosphere. Hence, the water oceans on Earth seem to be a thermodynamic consequence of particular physical conditions set by cosmic arrangements rather than an active controller of the global climate. Similarly, the hydrocarbon lakes on the surface of Titan [115,116] are the result of a high atmospheric pressure and an extremely cold environment found on that moon. Thus, our analysis did not reveal evidence for the existence of a feedback between planetary GMAT and a precipitable liquid solvent on the surface as predicted by the current climate theory. Consequently, the hypothesized *runaway greenhouse*, which requires a net positive feedback between global surface temperature and the atmospheric LW opacity controlled by water vapor [117], appears to be a model artifact rather than an actual physical possibility. Indeed, as illustrated in Figure 4, the hot temperature of Venus often cited as a product of a 'runaway greenhouse' scenario [117,118] fits perfectly within the pressure-dependent climate continuum described by Equations (10b) and (11).

Model Application and Validation

Encouraged by the high predictive skill and broad scope of validity of Model 12 (Figure 2f) we decided to apply Eq. (10b) to four celestial bodies spanning the breadth of the Solar System, i.e. Mercury, Europa, Callisto and Pluto which global surface temperatures are not currently known with certainty. Each body is the target of either ongoing or planned robotic exploration missions scheduled to provide surface thermal data among other observations, thus offering an opportunity to validate our planetary temperature model against independent measurements.

The MESSENGER spacecraft launched in 2004 completed the first comprehensive mapping of Mercury in March 2013 (http://messenger.jhuapl.edu/). Among other things, the spacecraft also took infrared measurements of the planet's surface using a special spectrometer [119] that should soon become available. The New Horizons spacecraft launched in January 2006 [120] reached Pluto in July of 2015 and performed a thermal scan of the dwarf planet during a flyby. The complete dataset from this flyby were received on Earth in October of 2016 and are currently being analyzed. A proposed joint Europa-Jupiter System Mission by NASA and the European Space Agency is planned to study the Jovian moons after year 2020. It envisions exploring Europa's physical and thermal environments both remotely via a NASA Orbiter and *in situ* by a Europa Lander [121].

All four celestial bodies have somewhat eccentric orbits around the Sun. However, while Mercury's orbital period is only 88 Earth days, Europa and Callisto circumnavigate the Sun once every 11.9 Earth years while Pluto takes 248 Earth years. The atmospheric pressure on Pluto is believed to vary between 1.0 and 4.0 Pa over the course of its orbital period as a function of insolation-driven sublimation of nitrogen and methane ices on the surface [122]. Each body's temperature was evaluated at three orbital distances from the Sun: aphelion, perihelion, and the semi-major axis. Since Mercury, Europa and Callisto harbor tenuous atmospheres ($P << 10^{-2}$ Pa), the reference temperature T_{na} in Eq. (10b) must be calculated from Eq. (4a), which requires knowledge of the actual values of α_e, η_e, and R_g. We assumed that Mercury had R_g = 0.0 W m^{-2}, α_e = 0.068 [123] and Moon-like thermo-physical properties of the regolith (η_e = 0.00971). Input data for Europa and Callisto were obtained from Spencer et al. [124] and Moore et al. [125], respectively. Specifically, in order to calculate η_e and R_g for these moons we utilized equatorial temperature data provided by Spencer et al. [124] in their Figure 1, and by Moore et al. [125] in their Fig. 17.7 along with a theoretical formula for computing the average nighttime surface temperature T at the equator based on the SB law, i.e.

$$T = \left[\frac{S(1-\alpha)\eta_e + R_g}{0.98\sigma}\right]^{0.25} \quad (15)$$

where $S(1-\alpha)\eta_e$ is the absorbed solar flux (W m^{-2}) stored as heat into the subsurface. The geothermal heat flux on Europa is poorly known. However, based on thermal observations of Io reported by Veeder et al. [126], we assumed R_g = 2.0 W m^{-2} for Europa. Using S = 50.3 W m^{-2}, an observed nighttime equatorial temperature T = 90.9 K and an observed average night-side albedo α = 0.58 [124], we solved Eq. (15) for the surface heat storage fraction to obtain η_e = 0.085 for Europa. A similar computational procedure was employed for Callisto using α = 0.11 and equatorial surface temperature data from Fig. 17.7 in Moore et al. [125]. This produced R_g = 0.5 W m^{-2} and η_e = 0.057. Using these values in Eq. (15) correctly reproduced Callisto's nighttime equatorial surface temperature of ≈ 86.0 K. The much higher η_e estimates for Europa and Callisto compared to η_e = 0.00971 for the Moon can be explained with the large water-ice content on the surface of these Galilean moons. Europa is almost completely covered by a thick layer of water ice, which has a much higher thermal conductivity than the dry regolith. Also, sunlight penetrates deeper into ice than it does into powdered regolith. All this enables a much larger fraction of the absorbed solar radiation to be stored into the subsurface as heat and later released at night boosting the nighttime surface temperatures of these moons. Volokin and ReLlez [1] showed that GMAT of airless bodies is highly sensitive to η_e.

Table 6 lists the average global surface temperatures of the four celestial bodies predicted by Eq. (10b) along with the employed input data. According to our model, Mercury is about 117 K cooler on average than NASA's current estimate of 440 K [32], which is based on Eq. (3) and does not represent a spherically averaged surface temperature [1]. Our prediction of Europa's GMAT, 99.4 K, agrees well with the ≈ 100 K estimate reported for this moon by Sotin et al. [127]. Our estimate of Pluto's average surface temperature at perihelion (38.6 K) is similar to the mean temperature computed for that dwarf planet by Olkin et al. [124] using a mechanistic model of nitrogen ice volatilization at the surface. Stern et al. [128] and Gladstone et al. [93] reported initial results from flyby observations of Pluto taken by the Radio Experiment (REX) instrument aboard the New Horizons spacecraft in July 2015, when the dwarf planet was approximately at 32.9 AU from the Sun. Using the observed surface pressure of 1.05 ± 0.1 Pa (10.5 ± 1 μbar) [93] our model predicts an average global temperature of 36.7 K for Pluto. Stern et al. [128] reported a near-surface temperature of ≈ 38 K. However, this value was calculated from pre-flyby global brightness measurements rather than derived via spherical integration of spatially resolved surface temperatures (Stern, personal communication). Since global brightness temperatures tend to be higher than spherically averaged kinetic surface temperatures [1], our model prediction may well be within the uncertainty of Pluto's true global temperature. We will know more about this in 2017 when spatially resolved thermal measurements obtained by New Horizons become available.

One should use caution when comparing results from Eq. (10b) to remotely sensed 'average temperatures' commonly quoted for celestial bodies with tenuous atmospheres such as the moons of Jupiter and Neptune. Studies oftentimes report the so-called 'brightness temperatures' retrieved at specific wavelengths that have not been subjected to a proper spherical integration. As pointed out by Volokin and ReLlez [1], due to Hölder's inequality between integrals, calculated brightness temperatures of spherical objects can be significantly higher than actual mean kinetic temperatures of the surface. Since Eq. (10b) yields spherically averaged temperatures, its predictions for airless bodies are expected to be lower than the disk integrated brightness temperatures typically quoted in the literature.

Conclusion

For 190 years the atmosphere has been thought to warm Earth by absorbing a portion of the outgoing LW infrared radiation and reemitting it back toward the surface, thus augmenting the incident solar flux. This conceptualized continuous absorption and downward reemission of thermal radiation enabled by certain trace gases known to be transparent to solar rays while opaque to electromagnetic long wavelengths has been likened to the trapping of heat by glass greenhouses, hence the term 'atmospheric greenhouse effect'. Of course, we now know that real greenhouses preserve warmth not by trapping infrared radiation but by physically obstructing the convective heat exchange between a greenhouse interior and the exterior environment. Nevertheless, the term 'greenhouse effect' stuck in science.

The hypothesis that a freely convective atmosphere could retain (trap) radiant heat due its opacity has remained undisputed since its introduction in the early 1800s even though it was based on a theoretical conjecture that has never been proven experimentally. It is important to note in this regard that the well-documented enhanced absorption of thermal radiation by certain gases does not imply an ability of such gases to trap heat in an open atmospheric environment. This is because, in gaseous systems, heat is primarily transferred (dissipated) by convection (i.e. through fluid motion) rather than radiative exchange. If gases of high LW absorptivity/emissivity such as CO_2, methane and water vapor were indeed capable of trapping radiant heat, they could be used as insulators. However, practical experience has taught us that thermal radiation losses can only be reduced by using materials of very low LW

	Surface Atmospheric Pressure (Pa)	α_e (fraction) η_e (fraction) R_g (W m^2)	Predicted Average Global Surface Temperature at Specific Orbital Distances from the Sun		
			Aphelion	Semi-major Axis	Perihelion
Mercury	5 × 10^{-10}	α_e = 0.068 η_e = 0.00971 R_g = 0.0	296.8 K (0.459 AU)	323.3 K (0.387 AU)	359.5 K (0.313 AU)
Europa	10^{-7}	α_e = 0.62 η_e = 0.085 R_g = 2.0	98.1 K (5.455 AU)	99.4 K (5.203 AU)	100.7 K (4.951 AU)
Callisto	7.5 × 10^{-7}	α_e = 0.11 η_e = 0.057 R_g = 0.5	101.2 K (5.455 AU)	103.2 K (5.203 AU)	105.4 K (4.951 AU)
Pluto	1.05	α_e = 0.132 η_e = 0.00971 R_g = 0.0	30.0 K (49.310 AU)	33.5 K (39.482 AU)	38.6 K (29.667 AU)

Table 6: Average global surface temperatures predicted by Eq. (10b) for Mercury, Europa, Calisto and Pluto. Input data on orbital distances (AU) and total atmospheric pressure (Pa) were obtained from the NASA Solar System Exploration [48] website, the NASA Planetary Factsheet [32] and Gladstone et al. [93]. Solar irradiances required by Eq. (10b) were calculated from reported orbital distances as explained in the text. Values of α_e, η_e and R_g for Europa and Callisto were estimated from observed data by Spencer et al. [124] and Moore et al. [125] respectively (see text for details).

absorptivity/emissivity and correspondingly high thermal reflectivity such as aluminum foil. These materials are known among engineers at NASA and in the construction industry as *radiant barriers* [129]. It is also known that high-emissivity materials promote radiative cooling. Yet, all climate models proposed since 1800s are built on the premise that the atmosphere warms Earth by limiting radiant heat losses of the surface through the action of infrared absorbing gases aloft.

If a trapping of radiant heat occurred in Earth's atmosphere, the same mechanism should also be expected to operate in the atmospheres of other planetary bodies. Thus, the Greenhouse concept should be able to mathematically describe the observed variation of average planetary surface temperatures across the Solar System as a continuous function of the atmospheric infrared optical depth and solar insolation. However, to our knowledge, such a continuous description (model) does not exist. Furthermore, measured magnitudes of the global down-welling LW flux on planets with thick atmospheres such as Earth and Venus indicate that the lower troposphere of these bodies contains internal kinetic energy far exceeding the solar input [6,12,14]. This fact cannot be explained via re-radiation of absorbed outgoing thermal emissions by gases known to supply no additional energy to the system. The desire to explicate the sizable energy surplus evident in the tropospheres of some terrestrial planets provided the main impetus for this research.

We combined high-quality planetary data from the last three decades with the classical method of dimensional analysis to search for an empirical model that might accurately and meaningfully describe the observed variation of global surface temperatures throughout the Solar System while also providing a new perspective on the nature of he atmospheric thermal effect. Our analysis revealed that the equilibrium global surface temperatures of rocky planets with tangible a mospheres and a negligible geothermal surface heating can reli bly be estimated across a wide range of atmospheric compositions and radiative regimes using only two forcing variables: TOA solar irradiance and total surf ce atmospheric pressure (Eq. 10b with T_{na} computed from Eq. 4c). Furthermore, the relative atmospheric thermal enhancement (RATE) defined as a ratio of the planet's actual global surface temperature to the temperature it would have had in the ab ence of a mosphere is fully explicable by the surface air pressure lone (Eq. 10a and Figure 4). At the same time, greenhouse-gas oncentrations and/or partial pressures did not show any meaningful relationship to surface temperatures across a broad span of plan tary environments considered in our study (see Figures 1 and 2 and Table 5).

Based on statistical criter a including numerical accuracy, robustness, dimensional homogeneity and a broad environmental scope of validity, the new relationship (Figure 4) quantified by Eq. (10a) appears to describe an emergent macro-level thermodynamic property of planetary atmospheres heretofore unbeknown to science. The physical significance of this empirical model is further supported by its striking qualitative resemblance to the dry adiabatic temperature curve described by the Poisson formula (Eq. 13) and to the photon-pressure form of the SB radiation law (Eq. 14). Similar to these well-known kinetic relations, Eq. (10a) also predicts the direct effect of pressure on temperature albeit in the context of a different macro-physical system. To our knowledge, this is the first model accurately describing the average surface temperatures of planetary bodies throughout the Solar System in the context of a thermodynamic continuum using a common set of drivers.

The planetary temperature model consisting of Equations (4a), (10b), and (11) has several fundamental theoretical implications, i.e.

- The 'greenhouse effect' is not a radiative phenomenon driven by the atmospheric infrared optical depth as presently believed, but a pressure-induced thermal enhancement analogous to adiabatic heating and independent of atmospheric composition;
- The down-welling LW radiation is not a global driver of surface warming as hypothesized for over 100 years but a product of the near-surface air temperature controlled by solar heating and atmospheric pressure;
- The albedo of planetary bodies with tangible atmospheres is not an independent driver of climate but an intrinsic property (a byproduct) of the climate system itself. This does not mean that the cloud albedo cannot be influenced by external forcing such as solar wind or galactic cosmic rays. However, the magnitude of such influences s expected to be small due to the stabilizing effect of negative feedbacks operating within the system. This understanding explains the observed remarkable stability of planetary albedos;
- The equilibrium surface temperature of a planet is bound to remain stable (i.e. within ± 1 K) as long as the atmospheric mass and the TOA mean solar irradiance are stationary. Hence, Earth's climate system is well buffered against sudden changes and has n tipping points;

  The proposed net positive feedback between surface temperature and the atmospheric infrared opacity controlled by water vapor appears to be a model artifact resulting from a mathematical decoupling of the radiative-convective heat transfer rather than a physical reality.

The hereto reported findings point toward the need for a paradigm shift in our understanding of key macro-scale atmospheric properties and processes. The implications of the discovered planetary thermodynamic relationship (Figure 4, Eq. 10a) are fundamental in nature and require careful consideration by future research. We ask the scientific community to keep an open mind and to view the results presented herein as a possible foundation of a new theoretical framework for future exploration of climates on Earth and other worlds.

Appendices

Appendix A. Construction of the Dimensionless π Variables

Table 1 lists 6 generic variables (T_s, T_r, S, P_x, P_r and ρ_x) composed of 4 fundamental dimensions: mass [M], length [L], time [T], and absolute temperature [Θ]. According to the Buckingham Pi theorem [27], this implies the existence of two dimensionless π_i products per set. To derive the π_i variables we employed the following objective approach. First, we hypothesized that a planet's GMAT (T_s) is a function of all 5 independent variables listed in Table 1, i.e.

$$T_s = f\left(T_r, S, P_x, P_r, \rho_x\right) \tag{A.1}$$

This unknown function is described to a first approximation as a simple product of the driving variables raised to various powers, i.e.

$$T_s \approx T_r^a S^b P_x^c P_r^d \rho_x^e \tag{A.2}$$

where a, b, c, d and e are rational numbers. In order to determine the power coefficients, Eq. (A.2) is cast in terms of physical dimensions of the participating variables, i.e.

$$[\Theta] \approx [\Theta]^a \left[\mathrm{M\,T^{-3}}\right]^b \left[\mathrm{M\,L^{-1}\,T^{-2}}\right]^c \left[\mathrm{M\,L^{-1}\,T^{-2}}\right]^d \left[\mathrm{M\,L^{-3}}\right]^e \tag{A.3}$$

Satisfying the requirement for dimensional homogeneity of Eq.

(A.2) implies that the sum of powers of each fundamental dimension must be equal on both sides of Eq. (A.3). This allows us to write four simultaneous equations (one per fundamental dimension) containing five unknowns, i.e.

$$\begin{cases} a = 1 & :[\Theta] \\ b + c + d + e = 0 & :[M] \\ -c - d - 3e = 0 & :[L] \\ -3b - 2c - 2d = 0 & :[T] \end{cases} \quad \text{(A.4)}$$

System (A.4) is underdetermined and has the following solution: $a = 1$, $b = 2e$, and $c = -(3e + d)$. Note that, in the DA methodology, one oftentimes arrives at underdetermined systems of equations, simply because the number of independent variables usually exceeds the number of fundamental physical dimensions comprising such variables. However, this has no adverse effect on the derivation of the sought dimensionless π_i products.

Substituting the above roots in Eq. (A.2) reduces the original five unknowns to two: d and e, i.e.

$$T_s \approx T_r^1 \; S^{2e} \; P_x^{-(3e+d)} \; P_r^d \; \rho_x^e \quad \text{(A.5a)}$$

These solution powers may now be assigned arbitrary values, although integers such as 0, 1 and -1 are preferable, for they offer the simplest solution leading to the construction of proper π_i variables. Setting $d = 0$ and $e = -1$ reduces Eq. (A.5a) to

$$T_s \approx T_r^1 \, S^{-2} \, P_x^3 \, \rho_x^{-1} \quad \text{(A.5b)}$$

providing the first pair of dimensionless products:

$$\pi_1 = \frac{T_s}{T_r}; \qquad \pi_2 = \frac{P_x^3}{\rho_x S^2} \quad \text{(A.6)}$$

The second pair of π_i variables emerges upon setting $d = -1$ and $e = 0$ in Eq. (A.5a), i.e.

$$\pi_1 = \frac{T_s}{T_r}; \qquad \pi_2 = \frac{P_x}{P_r} \quad \text{(A.7)}$$

Thus, the original function (A.1) consisting of six dimensioned variables has been reduced to a relationship between two dimensionless quantities, i.e. $\pi_1 = f(\pi_2)$. This relationship must further be investigated through regression analysis

Appendix B. Estimation of Mars' GMAT and Surface Atmospheric Pressure

Although Mars is the third most studied planetary body in the Solar System after Earth and the Moon, there is currently no consensus among researchers regarding its mean global surface temperature (T_M). T_M values reported over the past 15 years span a range of 40 K. Examples of disparate GMATs quoted for the Red Planet include 200 K [79], 202 K [82,130], 210 K [32], 214 K [80], 215 K [6,81], 218 K [77], 220 K [76], 227 K [131] and 240 K [78]. The most frequently cited temperatures fall between 210 K and 220 K. However, a close examination of the available thermal observations reveals a high improbability for any of the above estimates to represent Mars' true GMAT.

Figure B.1 depicts hourly temperature series measured at 1.5 m aboveground by Viking Landers 1 and 2 (VL1 and VL2 respectively) in the late 1970s [60]. The VL1 record covers about half of a Martian year, while the VL2 series extends to nearly 1.6 years. The VL1 temperature series captures a summer-fall season on a site located at about 1,500 m below Datum elevation in the subtropics of Mars' Northern Hemisphere (22.5° N). The arithmetic average of the series is 207.3 K (Fig. B.1a). Since the record lacks data from the cooler winter-spring season, this value is likely higher than the actual mean annual temperature at that location. Furthermore, observations by the Hubble telescope from the mid-1990s indicated that the Red Planet may have cooled somewhat since the time of the Viking mission [132,133]. Because of a thin atmosphere and the absence of significant cloud cover and perceptible water, temperature fluctuations near the surface of Mars are tightly coupled to diurnal, seasonal and latitudinal variations in incident solar radiation. This causes sites located at the same latitude and equivalent altitudes to have similar annual temperature means irrespective of their longitudes [134]. Hence, one could reliably estimate a latitudinal temperature average on Mars using point observations from any elevation by applying an appropriate lapse-rate correction for the average terrain elevation of said latitude.

At 22.5° absolute latitude, the average elevation between Northern and Southern Hemisphere on Mars is close to Datum level, i.e. about 1,500 m above the VL1 site. Adjusting the observed 207.3 K temperature average at VL1 to Datum elevation using a typical near-surface Martian lapse rate of -4.3 K km^{-1} [78] produces ~201 K for the average summer-fall temperature at that latitude. Since the mean surface temperature

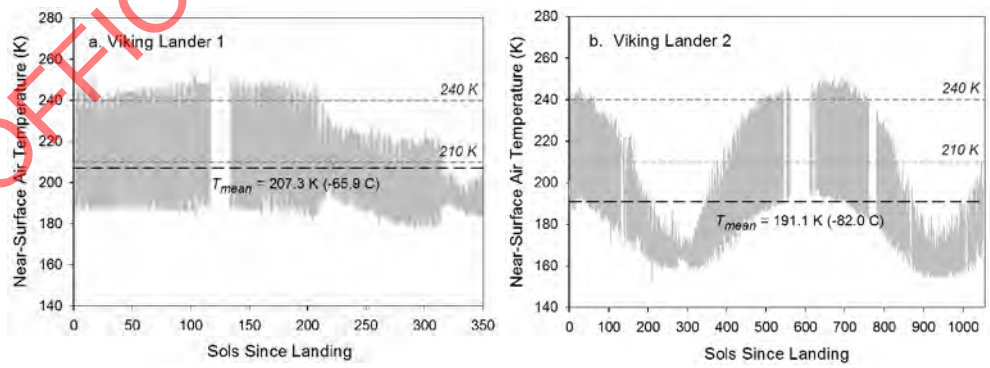

Figure B.1: Near-surface hourly temperatures measured on Mars by (*a*) Viking Lander 1 at Chryse Planitia (22.48° N, 49.97° W, Elevation: -1,500 m); and (*b*) Viking Lander 2 at Utopia Planitia (47.97° N, 225.74° W, Elevation: -3,000 m) (Kemppinen et al. [60]; data downloaded from: http://www-k12.atmos.washington.edu/k12/resources/mars_data-information/data.html). Black dashed lines mark the arithmetic average (T_{mean}) of each series. Grey dashed lines highlight the range of most frequently reported GMAT values for Mars, i.e. 210–240 K. The average diurnal temperature can only exceed 210 K during the summer; hence, all Martian latitudes outside the Equator must have mean annual temperatures significantl lower than 210 K.

of a sphere is typically lower than its subtropical temperature average, we can safely conclude based on Figure B.1a that Mars' GMAT is likely below 201 K. The mean temperature at the VL2 site located at ~48° N latitude and 3,000 m below Datum elevation is 191.1 K (Fig. B.1b). The average terrain elevation between Northern and Southern Hemisphere at 48° absolute latitude is about -1,500 m. Upon adjusting the VL2 annual temperature mean to -1,500 m altitude using a lapse rate of -4.3 K km^{-1} we obtain 184.6 K. Since a planet's GMAT numerically falls between the mean temperature of the Equator and that of 42° absolute latitude, the above calculations suggest that Mars' GMAT is likely between 184 K and 201 K.

A close examination of the Viking record also reveals that average diurnal temperatures above 210 K only occur on Mars during the summer season and, therefore, cannot possibly represent an annual mean for any Martian latitude outside the Equator. On the other hand, frequently reported values of Mars' GMAT in excess of 210 K appear to be based on the theoretical expectation that a planet's average surface temperature should exceed the corresponding effective radiating temperature produced by Eq. (3) [6,78], which is $T_e \approx 212$ K for Mars. This presumption is rooted in the a priori assumption that T_e represents a planet's average surface temperature in the absence of atmospheric greenhouse effect. However, Volokin and ReLlez [1] have shown that, due to Hölder's inequality between integrals, the mean physical temperature of a spherical body with a tenuous atmosphere is always lower than its effective radiating temperature computed from the globally integrated absorbed solar flux. In other words, Eq. (3) yield non-physical temperatures for spheres. Indeed, based on results from a 3-D climate model Haberle [130] concluded that Mars' mean global surface temperature is at least 8 K cooler than the planet's effective radiating temperature. Therefore, Mars' GMAT must be inferred from actual measurements rather than from theoretical calculations.

In order to obtain a reliable estimate of Mars' GMAT, we calculated the mean annual temperatures at several Martian latitudes employing near-surface time series measured *in-situ* by Viking Landers and the Curiosity Rover, and remotely by the Mars Global Surveyor (MGS) spacecraft. The Radio Science Team (RST) at Stanford University utilized radio occultation of MGS refra tion data to retrieve seasonal time-series of near-surface atmosph ric temperature and pressure on Mars [61,62,135]. We utilized MGS-RST data obtained between 1999 and 2005. Calculated mean temperatures from *in-situ* measurements were adjusted to corresponding average errain elevations of target latitudes using a lapse rate of -4.3 K km^{-1} [78]. Figure B.2 portrays the estimated Mean Annual n ar surface Temperatures (MAT) at five absolute Martian latitudes (gray dots) along with their standard errors (vertical bars). The equatorial MAT was calculated from Curiosity Rover observations; tempera ures at absolute latitudes 0.392 rad (22.48°) and 0.837 rad (47.97°) were derived from VL measurements, while these at latitudes 1.117 rad (64°) and 1.396 rad (80°) were estimated from MGS-RST data. The black curve represents a third-order polynomial fitted through the latitudinal temperature averages and described by the polynomial:

$$T(L) = 202.888 - 0.781801L - 22.3673L^2 - 3.16594L^3 \qquad (B.1)$$

with L being the absolute latitude (rad). MAT values predicted by Eq. (B.1) for Mars' Equatorial and Polar Regions agree well with independent near-surface temperatures remotely measured by the Mars Climate Sounder (MCS), a platform deployed after MGS in 2006 [136]. Shirley et al. [136] showed that, although separated in time by 2-5 years, MCS temperature profiles match quite well those retrieved by MGS-RST especially in the lower portion of the Martian atmosphere. Figures 2 and 3 of Shirley et al. [136] depict nighttime winter temperature profiles over the Mars' northern and southern Polar Regions, respectively at about 75° absolute latitude. The average winter surface temperature between the two Hemispheres for this latitude is about 148.5 K. This compares favorably with 156.4 K produced by Eq. (B.1) for 75° (1.309 rad) latitude considering that MAT values are expected to be higher than winter temperature averages. Figures 4 and 5 of Shirley et al. [136] portray average temperature profiles retrieved by MGS-RST and MCS over lowlands (165° – 180° E) and highlands (240° - 270° E) of the Mars' equatorial region (8° N - 8° S), respectively. For highlands (≈5 km above Datum), the near-surface temperature appears to be around 200 K, while for lowlands (≈2.5 km below Datum) it is ≈211 K. Since most of Mars' equatorial region lies above Datum, it is likely that Mars' equatorial MAT would be lower than 205.5 K and close to our independent estimate of ≈203 K based on Curiosity Rover measurements.

Mars' GMAT (T_M) was calculated via integration of polynomial (B.1) using the formula:

$$T_M = \int_0^{\pi/2} T(L)\cos L\, dL \qquad (B.2)$$

where $0 \le \cos L \le 1$ is a polar-coordinate area-weighting factor. The result is $T_M = 190.56 \pm 0.7$ K (Figure B.2). This estimate, while significantly lower than GMAT values quoted in recent publications, agrees quite well with spherically integrated brightness temperatures of Mars retrieved from remote microwave observations during the late 1960s and early 1970s [85-87]. Thus, according to Hobbs et al. [85] and Klein [86], the Martian mean global temperature (inferred from measurements at wavelengths between 1 and 21 cm) is 190 – 193 K. Our T_M estimate is also consistent with the new mean surface temperature of the Moon (197.35 K) derived by Volokin and ReLlez [1] using output from a validated NASA thermo-physical model [29]. Since Mars receives 57% less solar ittadiance than the Moon and has a thin atmosphere that only delivers a weak greenhouse effect [9], it makes a physical sense that the Red Planet would be on average cooler than our Moon (i.e. $T_M < 197.3$K). Moreover, if the average temperature

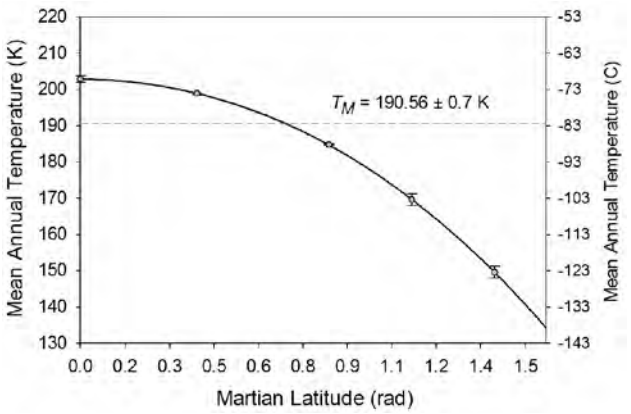

Figure B.2: Mean annual surface air temperatures at five Martian absolute latitudes (gray dots) es imated from data provided by Viking Landers, Curiosity Rover, and the Mars Global Surveyor Radio Science Team. Each dot represents a mean annual temperature corresponding to the average terrain elevation between Northern and Southern Hemisphere for particular latitude. The black curve depicts a third-order polynomial (Eq. B.1) fitted through the latitudinal temperature means using a non-linear regression. Mars' GMAT, T_M = 190.56 K (marked by a horizontal gray dashed line) was calculated via integration of polynomial (B.1) using formula (B.2).

of the lunar equator (Moon's warmest latitude) is 213 K as revealed by NASA Diviner observations [1,29], it is unlikely that Mars' mean global temperature would be equal to or higher than 213 K as assumed by many studies [6,76-78,80,131]

Published values of Mars' average surface atmospheric pressures range from 600 Pa to 700 Pa [6,32,78,80,83,84]. Since this interval was too broad for the target precision of our study, we employed MGS-RST data retrieved from multiple latitudes and seasons between 1999 and 2005 to calculate a new mean surface air pressure for the Red Planet. Our analysis produced $P = 685.4 \pm 14.2$ Pa, an estimate within the range of previously reported values.

Funding Sources

This research did not receive any specific grant from funding agencies in the public, commercial, or not-for-profit sectors

References

1. Volokin D, ReLlez L (2014) On the average temperature of airless spherical bodies and the magnitude of Earth's atmospheric thermal effect. Springer Plus 3: 723.
2. Hansen J, Johnson D, Lacis A, Lebedeff S, Lee P, et al. (1981) Climate impact of increasing atmospheric carbon dioxide. Science 213: 957-966.
3. Peixoto JP, Oort AH (1992) Physics of climate. Springer-Verlag, New York.
4. Wallace JM, Hobbs PV (2006) Atmospheric science: An Introductory survey, Academic Press, California.
5. Lacis AA, Schmidt GA, Rind D, Ruedy RA (2010) Atmospheric CO_2: Principal control knob governing Ear h's temperature. Science 330.
6. Lacis AA, Hansen JE, Russell GL, Oinas V, Jonas J (2013) The role of long lived greenhouse gases as principal LW control knob that governs the global surface temperature for past and future climate change. Tellus B 65: 19734.
7. Schmidt GA, Ruedy R, Miller RL, Lacis AA et al. (2010) The attribution of he present-day total greenhouse effect. J Geophys Res 115: D20106.
8. RamanathanV, Inamdar A (2006) The radiative forcing due to clouds and water vapor. Frontiers of Climate Modeling. Cambridge University Press, Cambridg , pp. 119-151.
9. Pierrehumbert R (2010) Principles of planeta y climate. Cambridge University Press, New York.
10. Pierrehumbert R (2011) Infrared radiat on and planetary temperature. Phys Today 64: 33-38.
11. Trenberth KE, Fasullo JT, Kiehl J (2009) Earth's global energy budget. B Am Meteorol Soc March: 311-323.
12. Stephens GL, Li1 J, Wild M, Clayson CA, Loeb N, et al. (2012) An update on Earth's energy balance in light of the latest global observations. Nat Geosci 5: 691–696.
13. Wild M, Folini D, Schär C, Loeb N, Dutton EG, et al. (2013) The global energy balance from a surface perspective. Clim Dyn 40: 3107–3134.
14. Wild M, Folini D, Hakuba MZ, Schar C, Seneviratne SI, et al. (2015) The energy balance over land and oceans: An assessment based on direct observations and CMIP5 climate models. Clim Dyn 44: 3393.
15. Bengtsson L, Bonnet R-M, Grinspoon D, Koumoutsaris D, Lebonnois S, et al. (2013) Towards understanding the climate of Venus: Applications of terrestrial models to our sister planet, ISSI scientifi report series, Springer.
16. Rashevsky N (1960) Mathematical biophysics: Physico-mathematical foundations of biology. Dover Publications, New York.
17. Albertson ML, Barton JR, Simons DB (1961) Fluid mechanics for engineers. Prentice Hall, New Jersey.
18. Yalin MS (1971) Theory of hydraulic models. MacMillan.
19. Taylor ES (1974) Dimensional analysis for engineers. Clarendon Press, Oxford.
20. Bender EA, (1978) An introduction to mathematical modeling. John Wiley and Sons, NY.
21. Vignaux GA, Jain S (1988) An approximate inventory model based on dimensional analysis. Asia-Pacifi Journal of Operational Research 5: 117-123.
22. Huntley HE (1967) Dimensional analysis. Dover Publications, New York.
23. Vignaux GA (1991) Dimensional analysis in data modeling. In: Smith CR, Erickson G, Neudorfer PO (eds) Maximum entropy and Bayesian methods. Kluwer Academic Publishers, Seattle, pp 121-126
24. Vignaux GA, Scott JL (1999) Theory and methods: Simplifying regression models using dimensional analysis. Aust N Z J Stat 41: 31–42.
25. Van Der Ha JC, Lappas VJ (2007) Long-term attitude drift of spinning spacecraft under solar radiation torques. Journal of Guidance, Control and Dynamics 30: 1470-1479.
26. McMahon J, Scheeres D (2010) A new navigation force model for solar radiation pressure. Journal of Guidance, Control and Dynamics 33: 1418-1428.
27. Buckingham E (1914) On physically similar systems: Illustrations of the use of dimensional equations. Phys Rev 4: 345-376.
28. Taylor FW (2010a) Planeta y a mospheres. Oxford University Press, USA.
29. Vasavada AR, Bandfiel JL, Greenhagen BT, Hayne PO, Siegler MA, et al. (2012) Lunar equa orial surface temperatures and regolith properties from the diviner lunar radiometer experiment. J Geophy Res 117: E00H18.
30. Blanco VM, McCuskey SW (961) Basic physics of the solar system. Addison-Wesley, R ading MA.
31. Mölle F (1964) Optics of he lower atmosphere. Appl Optics 3: 157-166.
32. Will ams DR (2015) NASA Planetary Factsheet. NASA online.
33. Beckenbach EF, Bellman R (1983) Inequalities. Springer Verlag, Berlin.
34. Rubincam DP (2004) Black body temperature, orbital elements, the Milankovitch precession index and the Sever smith psychroterms. Theor Appl Climatol 79: 111–131.
35. Fix en DJ (2009) The temperature of the cosmic microwave background. Ap J 707: 916.
36. Paige DA, Foote MC, Greenhagen BT, Schofiel JT, Calcutt S, et al. (2010) The lunar reconnaissance orbiter diviner lunar radiometer experiment. Space Sci Rev 150: 125–160.
37. Leconte J, Forget F, Charnay B, Wordsworth R, Selsis F, et al. (2013) 3D climate modeling of close-in land planets: circulation patterns, climate moist bistability and habitability. Astron Astrophys 554, A69.
38. Cengel YA, Turner RH (2004) Fundamentals of thermal-flui sciences. McGraw-Hill, Boston.
39. Steel RGD, Torrie J H (1960) Principles and procedures of statistics with special reference to the biological sciences. McGraw Hill.
40. Zwillinger D (2003) Standard mathematical tables and formulae. Chapman & Hall/CRC, p: 912.
41. Atreya SK, Lorenz RD, Waite JH (2009) Volatile origin and cycles: Nitrogen and methane. In: Brown RH, Lebreton JP, Waite JH (eds) Titan from Cassini-Huygens. Springer, New York, pp: 177–200
42. Jennings DE, Flasar FM, Kunde VG, Samuelson RE, Pearl JC, et al. (2009) Titan's surface brightness temperatures. Astrophys J 691: L103–L105.
43. Cottini V, Nixona CA, Jennings DE, et al. (2012) Spatial and temporal variations in Titan's surface temperatures from Cassini CIRS observations. Planetary Space Sci 60: 62–71.
44. Fegley B, Zolotov MY, Lodders K (1997) The oxidation state of the lower atmosphere and surface of Venus. Icarus 125: 416-439.
45. Basilevsky AT, Head JW (2003) The surface of Venus. Rep Prog Phys 66: 1699–1734.
46. Mallama A, Wang D, Howard RA (2006) Venus phase function and forward scattering from H_2SO_4. Icarus 182: 10–22.
47. Basilevsky AT, McGill GE (2007) Surface evolution of Venus: Esposito LW Exploring Venus as a Terrestrial Planet (Geophysical Monograph Series), Wiley 176: 23-43.
48. NASA Solar System Exploration (2014) Planets.

49. Kopp G, Lean JL (2011) A new, lower value of total solar irradiance: Evidence and climate significanc . Geophys Res Lett 38: L01706.

50. Jones PD, New M, Parker DE, Martin S, Rigor IG (1999) Surface air temperature and its changes over the past 150 years, Rev Geophys 37: 173–199.

51. NOAA National Climatic Data Center (2014) Global surface temperature anomalies. Online publication by NOAA.

52. Smith TM, Reynolds RW, Peterson TC, Lawrimore J, et al. (2008) Improvements to NOAA's Historical Merged Land-Ocean Surface Temperature Analysis (1880-2006). J Climate 21: 2283-2296.

53. Trenberth KE, Smith L (2005) The mass of the atmosphere: A constraint on global analyses. J Climate 18: 864-875.

54. Stephens GL, O'Brien D, Webster PJ, Pilewski P, Kato S, et al. (2015) The albedo of Earth. Rev Geophys 53.

55. Loeb NG, Wielicki BA, Doelling DR, Smith GL, Keyes DF, et al. (2009) Toward optimal closure of the Earth's top-of-atmosphere radiation budget. J Climate 22:748–766.

56. Lucey, P Korotev RL, Gillis JJ, Taylor LA, Lawrence D, et al. (2006) Understanding the lunar surface and space-Moon interactions. Reviews in Mineralogy and Geochemistry 60: 83–219.

57. Keihm SJ (1984) Interpretation of the lunar microwave brightness temperature spectrum: feasibility of orbital heat flo mapping. Icarus 60: 568–589.

58. Vasavada AR, Paige DA, Wood SE (1999) Near-surface temperatures on Mercury and the Moon and the stability of polar ice deposits. Icarus 141: 179–193.

59. Mat hews G (2008) Celestial body irradiance determination from an underfille satellite radiometer: Application to albedo and thermal emission measurements of the Moon using CERES. Applied Optics 47: 4981-4993.

60. Kemppinen O, Tillman JE, Schmidt W, Harri AM (2013) New analysis software for Viking Lander meteorological data. Geosci Instrum Me hod Data Syst 2: 61–69.

61. Hinson DP, Smith MD, Conrath BJ (2004) Comparison of atmospheric temperatures obtained through infrared sounding and radio occultation by Ma s Global Surveyor. J Geophys Res 109: E12002.

62. Hinson DP (2006) Radio occultation measurements of tran ient eddies in he northern hemisphere of Mars. J Geophys Res 11 : E05002.

63. Bandfiel JL, Wolff MJ, Smith MD, Daniel JM (2013) Radiome ric comparison of Mars Climate Sounder and Thermal Emis ion spectrometer measurements. Icarus 225: 28-39.

64. Younkin RL (1974) The albedo of Titan. Ic rus 21: 219–229.

65. Hanel RA, Pearl JC, Samuelson RE (1985) The bolometric bond albedo of Titan. Bulletin of the Astronomical Society 17: 739.

66. Neff JS, Ellis TA, Apt J, Bergstralh JT (1985) Bolometric albedos of Titan, Uranus, and Neptune. Icarus 62: 425–432.

67. Fulchignoni M, Ferri F, Angrilli F, Ball A , Nub-Bar A, et al. (2005) *In situ* measurements of the physical characte istics of Titan's environment. Nature 438: 785-791.

68. Niemann HB, Atreya SK, Bauer SJ, Carignan GR, Demick JE, et al. (2005) The abundances of constituents of Titan's atmosphere from the GCMS instrument on the Huygens probe. Nature 438: 779–784.

69. Griffit CA (2007) Titan's lower atmosphere. AIP Conf Proc 930: 3-36.

70. Mitri G, Showmana AP, Lunine JI, Lorenz RD (2007) Hydrocarbon lakes on Titan. Icarus 186: 385–394.

71. Li L, Nixon CA, Achterberg RK, Smith MA, Gorius NJP, et al. (2011) The global energy balance of Titan. Geophys Res Lett 38: L23201.

72. Schinder PJ, Flasar FM, Marouf EA, French RG, Mcghee-French C, et al. (2012) The structure of Titan's atmosphere from Cassini radio occultation: Occultation from the Prime and Equinox missions. Icarus 221: 1020–1031.

73. Lellouch E, de Bergh C, Sicardy B, Ferron S, Kaufl HU (2010) Detection of CO in Triton's atmosphere and the nature of surface-atmosphere interac ions. Astron Astrophys 512: L8.

74. Nelson RM, Burattl BJ, Wallis BD, Smythe WD, Horn LJ, et al. (1990) Spectral geometric albedo and bolometric Bond albedo of Neptune's satellite Triton from Voyager observations. Geophys Res Lett 17: 1761–1764.

75. Elliot JL, Hammel HB, Wasserman LH, Franz OG, McDonald SW, et al. (1998) Global warming on Triton. Nature 393: 765-767.

76. Smil V (2003) The Earth's biosphere: Evolution, dynamics and change. MIT Press.

77. Vázquez M. Hanslmeier A (2006) Ultraviolet radiation in the solar system. Springer, The Netherlands.

78. Barlow N (2008) Mars: An introduction to its interior, surface and atmosphere. Cambridge University Press, Cambridge.

79. Rapp D (2008) Human missions to Mars: Enabling technologie for exploring the red planet. Springer, Germany.

80. Taylor FW (2010b) The scientifi exploration of Mars Cambridge University Press, Cambridge NY

81. Lissauer JJ, Pater I (2013) Fundamental planetary science: Physics, chemistry and habitability. Cambridge University Press, New York NY.

82. Fenton LK, Geis ler PE, Haberle RM (2007) Global warming and climate forcing by recent a bedo changes on Mars. Nature 446: 647-649.

83. Jakosky BM, Phillips RJ (2001) Mars' vo atile and climate history. Nature 412: 237-244

84. Catling DC, Leovy C (2007) Ma s atmosphere: History and surface interactions. In: Encyclopedia of the Solar System. Academic Press, pp: 301-314.

85. Hobbs RW, McCullough TP, Waak JA (1968) Measurements of Mars at 1.55 cm and 0.95 cm wavelengths. Icarus 9: 360–363.

86. Klein MJ (1971) Mars: measurements of its brightness temperature at 1.85 and 3.75 cm wave ength. Icarus 14: 210-213.

87. Briggs FH, Drake FD (1972) Interferometric observations of Mars at 21 cm wavel ngth. Icarus 17: 543-547.

88. Van man D, Reedy R, Heiken G, Haskin L, Greive R, et al. (1991) The lunar environment. In: Lunar Sourcebook: A User's Guide to he Moon. Cambridge University Press, Cambridge, pp 27-60

89. Morice CP, Kennedy JJ, Rayner NA, Jones PD (2012) Quantifying uncertainties in global and regional temperature change using an ensemble of observational estimates: The HadCRUT4 data set. J Geophys Res 117: D08101.

90. Peterson TC, Vose RS (1997) An overview of the global historical climatology network temperature database. Bull Am Meteorol Soc 78: 2837-2849

91. Smith TM, Reynolds RW (2005) A global merged land air and sea surface temperature reconstruction based on historical observations (1880-1997). J Climate 18: 2021-2036.

92. Hansen J, Sato M, Russell G, Kharecha P (2013) Climate sensitivity, sea level and atmospheric carbon dioxide. Phil Trans R Soc A 371: 20120294.

93. Gladstone GR, Stern SA, Ennico K, Olkin CB, Weaver HA, et al. (2016) The atmosphere of Pluto as observed by New Horizons. Science 351.

94. NASA JPL Voyager Mission (2013) Titan. Online publica ion by the California Institute of Technology.

95. NASA JPL Ephemeris (2014) Horizons web interface: California Institute of Technology.

96. Stolk H, Gates K, Hanan J (2003) Discovery of emergent natural laws by hierarchical multi-agent systems. In: Proceedings of the International Conference on Intelligent Agent Technology. IEEE/WIC International Conference on Intelligent Agent Technology, Halifax, Canada, pp: 75-82.

97. Wild M (2009) Global dimming and brightening: A review. J Geophys Res 114: D00D16.

98. Herman J, DeLand MT, Huang L-K, Labow G, Larko D, et al (2013) A net decrease in the Earth's cloud, aerosol, and surface 340 nm reflectivit during the past 33 years (1979–2011). Atmos Chem Phys 13: 8505–8524.

99. Stanhill GO, Rosa AR, Cohen S, Achiman O (2014) The cause of solar dimming and brightening at the Earth's surface during he last half century: Evidence from measurements of sunshine dura ion J Geophys Res Atmos 119: 10902–10911.

100. Snyder CW (2016) Evolution of global temperature over the past two million years. Nature 538: 226–228.

101. Heinemann M, Timmermann A, Timm OE, Saito F, Abe-Ouchi A (2014) Deglacial ice sheet meltdown: orbital pace making and CO_2 effects. Clim Past 10: 1567–1579.

102. Stap LB, van de Wal RSW, de Boer B, Bintanja R, Lourens LJ (2014) Interaction of ice sheets and climate during the past 800 000 years. Clim Past 10: 2135–2152.

103. McGehee R, Lehman C (2012) A paleoclimate model of ice-albedo feedback forced by variations in Earth's orbit. Siam J App Dyn Sys 11: 684–707.

104. Doughty AM, Schaefer JM, Putnam AE, Denton GH, Kaplan MR, et al. (2015) Mismatch of glacier extent and summer insolation in Southern Hemisphere mid-latitudes. Geology G36477.1.

105. Maslin MA, Brierley CM (2015) The role of orbital forcing in the early middle Pleistocene transition. Quat Int 389: 47–55

106. Berner RA (2006) Geological nitrogen cycle and atmospheric N_2 over Phanerozoic ime. Geology 34: 413-415.

107. Vladilo G, Murante G, Silva L, Provenzale A, Ferri G, et al. (2013) The habitable zone of Earth-like planets with different levels of atmospheric pressure. Astrophys J 767: 65.

108. Svensmark H, Bondo T, Svensmark J (2009) Cosmic ray decreases affect atmospheric aerosols and clouds. Geophys Res Lett 36: L15101.

109. Svensmark J, Enghoff MB, Svensmark H (2012) Effects of cosmic ray decreases on cloud microphysics. Atmos Chem Phys Discuss 12: 3595–3617.

110. Svensmark J, Enghoff MB, Shaviv N, Svensmark H (2016) The response of clouds and aerosols to cosmic ray decreases. J Geophys Res Space Physics 121: 8152-8181.

111. Voiculescu M, Usoskin I, Condurache-Bota S (2013) Clouds blown by the solar wind. Environ Res Lett 8: 045032.

112. Scafetta N (2016) High resolu ion coherence analysis between planetary and climate oscillations. Adv Space Res 57: 2121–2135.

113. Kirkby J, Duplissy J, Sengupta K, Frege C, Gordon H, et al. (2016) Ion induced nucleation of pure biogenic particles. Nature 533: 521–526.

114. Palle E, Goode PR, Montañés-Rodríguez P, Shumko A, Gonzalez-Merino B, et al. (2016) Earth's albedo variations 1998–2014 as measured from ground-based earthshine observations. Geophys Res Lett 43: 4531–4538.

115. Raulin F (2008) Planetary science: Organic lakes on Titan. Nature 454: 587-589.

116. Sharma P, Byrne S (2011) Comparison of Titan's north polar lakes with terrestrial analogs. Geophys Res Lett 38: L24203.

117. Goldblatt C, Watson AJ (20 2) The runaway greenhouse: Implications for future climate change, geoengineering and planetary atmospheres. Phil Trans R Soc A 370: 4197–4216.

118. Kasting JF (1988) Runaway and moist greenhouse atmospheres and the evolution of Earth and Venus. Icarus 74: 72-494.

119. McClintock WE, Lankton MR (2007) The Mercury atmospheric and surface composition spectrometer for the MESSENGER mission. Space Sci Rev 131: 481-521.

120. Stern SA (2008) The New Horizons Pluto Kuiper belt mission: An overview with historical context. Sp Sci Rev 140: 3-21.

121. Pappalardo RT, Vance S, Bagenal F, Bills BG, Blaney DL, et al. (2013) Science potential from a Europa lander. Astrobiology 13: 740-773.

122. Olkin CB, Young LA, Borncamp D, Pickles A, Sicardy B, et al. (2013) Pluto's atmosphere does not collapse. Cornell University Library, USA.

123. Mallama A, Wang D, Howard RA (2002) Photometry of Mercury from SOHO/LASCO and Earth. Icarus 155: 253–264.

124. Spencer JR, Tamppari LK, Martin TZ, Travis LD (1999) Temperatures on Europa from Galileo photopolarimeter-radiometer: Nighttime thermal anomalies. Science 284: 1514-1516.

125. Moore JM, Chapman CR, Bierhaus EB, Greeley R, Chuang FC, et al. (2004) Callisto. In: Jupiter: The planet, satellites and magnetosphere. Cambridge University Press, pp 397-426.

126. Veeder GJ, Matson DL, J hnson TV, Blaney DL, Goguen JD (1994) Io's heat flo from infrared radiometry: 1983–1993. J Geophys Res 99: 17095–17162.

127. Sotin C, Head II JW, Tobie G (2002) Europa: Tidal heating of upwelling thermal plumes and the origin of lenticulae and chaos melting. Geophys Res Lett 29: 74-1–74-4.

128. Stern SA, Bagenal F, Ennico K, Gladstone GR, Grundy WM, et al. (2015) The Pluto system: initial results from its exploration by New Horizons. Science 350.

129. Asadi A, Hassan MM (2014) E aluation of the thermal performance of a roof-mo nted radiant b rrier in residential buildings: Experimental study. J Building Phys 38: 66–80.

130. Haberle RM (2013) Estimating the power of Mars' greenhouse effect. Icarus 223: 619-620.

131. Schulze Makuch D, Méndez A, Fairén AG, von Paris P, Turse C, et al. (2011) A two-tiered approach to assessing the habitability of exoplanets. Astrobiology 11: 1041–1052.

132. Savage D, Jones T, Villard R (1995) Hubble monitors weather on neighboring planets. Hubble News Release Archive.

133. Clancy RT, Grossman AW, Wolff MJ, James PB, Rudy DJ, et al. (1996) Water vapor saturation at low altitudes around Mars aphelion: A key to Mars climate? Icarus 122: 36–62.

134. Wilson RJ, Richardson MI (2000) The Martian atmosphere during the Viking mission: I Infrared measurements of atmospheric temperatures revisited. Icarus 145: 555–579.

135. Mars Global Surveyor Radio Science Team (2007) The Daily Martian Weather Report. Online publication by Stanford University, USA.

136. Shirley JH, Schofiel J, Kleinböhl A, Abbatt JPD, Lollar BS, et al. (2011) Comparison of MGS Radio Science Mean temperature profile with Mars Climate Sounder (MCS) results. In: Forget CF et al. (eds), 'The Fourth International Workshop on the Mars Atmosphere: Modelling and observation', Paris, France.

Citation: Nikolov N, Zeller K (2017) New Insights on the Physical Nature of the Atmospheric Greenhouse Effect Deduced from an Empirical Planetary Temperature Model. Environ Pollut Climate Change 1: 112.

Local Government New Zealand leads on global warming

Bryan
Leyland

Posted on July 1, 2018 By Bryan Leyland

Local Government New Zealand have embarked on a "Climate Change Project" focused on adapting and mitigating "climate change" – properly described as man-made global warming.

When faced with a potential risk, the rational approach is to make sure that the risk is real, assess its magnitude, decide if anything needs to be done, and if so, what is the cheapest and most effective solution.

In spite of the fact that no one has any convincing evidence based on observations that man-made global warming real and dangerous LGNZ have jumped to the conclusion that the risk is real, urgent action is needed and lots of our money and resources must be spent on "fighting climate change". Taking an objective look at all the evidence never even crossed their minds.

If they had looked at the evidence, they would have got a big surprise.

They would have discovered that world temperatures have increased by about half the predicted amount over the last 20 years and New Zealand has hardly warmed it all. This would – or should – tell them that the computer models which the climate scientists rely upon for predicting future climate are worthless. There is nothing abnormal about the modest amount of warming that has occurred as we recover from the Little Ice Age.

They would also discover that sea level rise in New Zealand – and the rest of the world – has been steady at between 1.5 and 2 mm per year for the last hundred years and shows no sign of the claimed recent rapid increase. They would also discover that there is no reason – other than the failed climate models – to assume that it will rise more rapidly in the future.

If they studied storms, floods and droughts in New Zealand and the rest of the world they would find that recent weather is rather better than it was in the past. The IPCC agrees.

If they looked at the history of atoll formation they would realise that coral atolls were able to keep up with a sea level rise of 3000 mm per century at the end of the ice age. It follows that they cannot be in danger from the current tiny rate of sea level rise. Pacific islands do have real problems, but they are not caused by sea level rise.

If they looked further they would discover that there are many very credible papers based on observations and experiments that indicate a very high probability that the world will soon enter a cooling cycle. Right now sunspot levels are lower than they have been since the Little Ice Age and the correlation between sunspot levels and temperatures is very strong.

A Danish professor has established a cause and effect relationship between sunspot cycles, cosmic rays, low clouds and global temperatures. When sunspot levels are low, the magnetic shield emitted by the sun is low and this allows more high energy cosmic rays to reach lower levels in the atmosphere. When they do, they cause condensation and this triggers cloud formation. Other scientists have analysed past climate cycles and concluded that there is a high risk of global cooling.

While they regard carbon dioxide as a dangerous pollutant, without it, life on earth could not exist. The reality is that it is essential to life and plant growth and the recent rise in concentration has increased agricultural productivity by about 15%. A big win for New Zealand's economy..

They might also be interested to discover that neither the United Nations Intergovernmental Panel on Climate Change, the Royal Society of New Zealand nor Prof Jim Renwick can provide convincing evidence based on observations of the real world that man-made greenhouse gases cause dangerous global warming. The evidence simply does not exist. Until this evidence is discovered – if it ever is – the only rational conclusion is that man-made global warming is, in all probability, the biggest hoax in the history of the world.

It is tragic that Local Government New Zealand have bought into the global warming hoax.

We should not be squandering our money and damaging our economy in a futile attempt to solve a problem that, according to the evidence, does not exist.